David Charles Robartes Davidge

Development of a Two Phase Xenon Detector for Use in Direct Dark Matter Searches

A thesis presented for the degree of
Doctor of Philosophy of the University of London
and the
Diploma of Imperial College
June 2003

Abstract

This thesis presents research into the development of a two phase xenon detector for direct dark matter searches. The research was undertaken at Imperial College London, as part of the United Kingdom Dark Matter Collaboration during the years 1997 to 2003. Dark matter particles should interact with ordinary matter, depositing energy in a detector resulting in scintillation photons and ionisation. Xenon is a favourable target as it has a high light yield (78600 photons/MeV), has naturally occuring isotopes sensitive to spin dependent interactions, is dense when liquefied and can be obtained with low levels of intrinsic radioactivity. In this study, experiments with a scintillation test cell indicated the possibility for discrimination between nuclear recoil and electron recoil events using the pulse shape of the scintillation light. Measurements gave a decay time constant of 23±3ns for α-particle recoils and 43±8ns for electron recoils. Neutron recoil measurements at the Neutron Beam Facility at Sheffield University measured the quenching factor of liquid xenon to be 0.17±0.01. To reduce light losses the possibility of operating photomultipliers at liquid xenon temperatures was investigated. Results from these experiments indicated that photomultipliers remain linear at temperatures of -104.5°C, however, there is a decrease in response to pulsed light at frequencies of 2kHz. A two phase prototype detector was used to measure the scintillation photons and ionisation from interactions of α-particles and gamma-rays with xenon. These tests gave a discrimination factor of 90% between the two distributions of secondary to primary signal ratios. Monte Carlo analysis of the performance of ZEPLIN III addressed the light collection, charge drift and extraction, electroluminescence output and position sensitivity of the detector. A gamma-ray transportation code was also used to assess the background radioactivity due to the immersion of photomultipliers in the liquid xenon volume. Results from these programs indicate that ZEPLIN III will have a discrimination factor of 99.81% and be sensitive to spin independent cross sections of $7 \times 10^{-44}\text{cm}^2$.

Acknowledgements

A PhD is no easy task. Without the support of family, friends and colleagues it would be impossible. I would therefore like to extend my warmest thanks to the following.

Professor T. J. Sumner has been invaluable over the past five years as a font of knowledge and as a Supervisor.

Dr Alex S. Howard, whom I consider more a friend than a colleague, has been a mentor for me in all things instrumental, experimental and computational.

Arthur Bewick and Vadim Lebedenko have helped me overcome my misunderstandings in all things technical and mechanical. To this I, and the laboratory, owe them a great deal.

Jaime Dawson, another friend made at Imperial and a fine colleague.

Professor J. J. Quenby, Professor Gareth W. Jones and Dr G. J. Davies, I thank them for the discussions we have had over the past five years.

I offer my thanks to the other members of the United Kingdom Dark Matter Collaboration, their knowledge base provided a great forum for learning.

I would like to thank PPARC for their financial support.

To my friends in the Astrophysics Group who unbeknownst to themselves have made this thesis possible: L. Clewley, S. Mattila, L. Hartley, D. Farrah, K. Kolokoutsas, J. Vink, A. Meli.

To the other members of the Astrophysics Group who have provided such an incredible atmosphere of learning, my thanks.

I express thanks to the influential physics teachers that enthused me at a young age; Mr Blunkett and David Hepburn-Scott.

And now I digress, to thank those friendships that have given me such support and inspiration. Henry Morton - a really great bloke, as someone once said. Geoffroy Marie David Scholtes - I couldn't resist - another fine man and DBA extraordinaire. Hannah Chambers who makes me laugh incessantly, a wonderful girl taking the comedy world by storm. Sarah Lack, who shared the joyous experience of living with me in the ice-box that was 61b. Marika Lemos, mysterious and elusive but nonetheless a close friend. Charlotte Worsley and Elizabeth Eade (the order is chronological) - your beauty and intellects are unsurpassed. Can Essenbel, Bob Goodfellow, Karim Karmali, Ben Cutner, Cedric Scholtes, Aled Rees, Richard Docherty, Doniert MacFarlane, Luke Mugliston, Paul Crossfield; old friends with whom I will never lose touch. Spencer Dutton, Bas & Kirstin Van Dorp, Dominic Brightman, Daniel Pracny-Strass, Pauline Brocard (good luck with your thesis), Sue Brown (good luck with your thesis), Karine Oglivie, Andy Bellis & Becky Reeve, Ben Fox; all met an Imperial. Jon Walters and James Fern - thanks for the company during the first year and other enduring memories. Lisa Squires - my thanks for some delicious dinners, bbq's and looking after Jon. Paul Mackinlay and Joshua Hewitt, we had some good times together over the last four years with more to come I'm sure, I am indebted to you both for helping me with those computing glitches, good luck with your businesses.

Maintaining my fencing career has been of great difficulty during the past months and was made possible only by the help of some close friends and competitors. I must pay tribute to Tomek Walicki who has kept his faith in me, despite my inability to train often and more importantly contribute to club fees. With Chris Howarth and Liz Beckingham I have shared some fantastic times, most in their Peugeot on a motorway, and others which will live on in club folklore for many years. Those journeys would be meaningless of course without Kola Abidogun and Anna Bentley wedged in tightly beside me. I wish Nick and Sam Payne the best of luck as they embark on the journey of parenthood. Simon Smith has been a great friend for many years

(I believe since I was "this high") and brief colleague, the website will pick up soon I'm sure. Jon Weekes and Thalia, thanks for some thought provoking conversations. I extend my warmest regards to Marion, Jackie, Debbie, Linda, Kevin, Matt, David Taylor, Becky, Melissa, James Beevers (honorary) and all the other members of Salle Boston Fencing Club. To my other friends in fencing Russell Dudley-Smith (good luck on your thesis too!), Ellie Smith, 'The Scots', 'The Welsh', 'The Irish'; I wish you luck your future fights unless, of course, I happen to be at the other end. I reserve special thanks and praise to Pierre Harper, Britain's finest foilist of recent times and my mentor/coach during my developing years.

To the friends whose names currently escape me, I hope I am forgiven for your omition. Be assured however that this reflects not my feelings or your worth but rather the inadequacies of my address book.

Most importantly I thank Mum, Dad, Katie, Clare, Sarah, Emily, Jonathan and Barty - my family. Without your love I would never have come this far. I will never forget the support and encouragement that you have given when times were hard, I love you all very much. And finally to Jules without whom this thesis may never have been completed, thanks for your love and proof reading skills, I love you too very much.

Contents

List of Figures 11

List of Tables 17

Chapter 1 : The Dark Matter Scenario 19

1.1 A Dark History 20

1.2 Cosmology and Dark Matter 21

1.2.1 Modern Cosmology 22

1.2.2 Inflation and Ω 28

1.3 Astrophysical Observations of Dark Matter 34

1.3.1 Spiral Galaxy Rotation Curves 34

1.3.2 Galaxy Cluster Dynamics 35

1.3.3 Gravitational Lensing 36

1.4 Dark Matter in the Milky Way; The Candidates 37

1.4.1 Dark Baryonic Matter in the Milky Way 38

1.4.2 Non-Baryonic Dark Matter Candidates 41

1.5 Summary 43

Chapter 2 : Neutralino Dark Matter Detection 44

2.1 Introduction 44

2.2 Fundamentals of Detection 45

2.2.1 Elastic Scattering 45

2.2.2 Neutralino Number Density and Scattering Cross Section 47

2.2.3 Expected Event Rates and Energy Spectra 50

2.2.4 Dark Matter Detecting Philosophies 51

2.3 Summary of Terrestrial Dark Matter Searches 59

2.3.1 Exclusion Plots 60

2.4 Summary 63

Chapter 3 : Liquid Xenon Detectors **65**

3.1 Introduction 65

3.2 Xenon as a Target 65

3.2.1 Physical Properties 65

3.2.2 Scintillation and Ionisation in Liquid Xenon 68

3.2.3 Two Phase Discrimination Technique 71

3.2.4 Quenching Factor, q_r 72

3.3 Detecting Scintillation from Xenon 73

3.3.1 Fundamentals of Photomultipliers 73

3.3.2 The 9829QA ETL Photomultiplier 75

3.3.3 Low Temperature Photomultiplier Operation 75

3.3.4 Photomultiplier Radioactivity 80

3.4 Summary 81

Chapter 4 : Single Phase Liquid Xenon Detectors **82**

4.1 Introduction 82

4.2 Purification of Xenon 82

4.2.1 Purification Apparatus 82

4.2.2 Purification Strategy 87

4.3 Test Chamber Measurements 93

4.3.1 Test Chamber Desciption 94

4.3.2 Reflectivity Measurements 96

4.3.3 Scintillation Measurements 98

4.3.4 Measurement of Xenon Quenching Factor 99

4.3.5 Conclusions from Test Chamber Experiments 104

4.4 ZEPLIN I - Single Phase Xenon Detector 105

4.5 Summary 107

Chapter 5 : Two Phase Liquid Xenon Detectors **109**

5.1 Electron Drift in Liquid Xenon 110

5.1.1 Low Field Electron Drift, $V_d \propto E$ 111

5.1.2 High Field Electron Drift 111

5.1.3 Saturation Velocity 112

5.1.4 Summary of Electron Drift in Xenon 113

5.2 Recombination Scintillation and Charge Drift 113

5.3 Charge Extraction and Electroluminescence in Xenon Gas . . . 114

5.3.1 Charge Extraction 114

5.3.2 Electroluminescence 116

5.4 Two Phase Prototype Detector 117

5.4.1 Prototype Design 117

5.4.2 Prototype Operation 119

5.4.3 Results from Two Phase Prototype 120

5.4.4 Conclusions from Prototype Experiments 123

5.5 The ZEPLIN III Dark Matter Detector 125

5.5.1 Target Maximisation and Contamination Minimisation . 126

5.5.2 Brief Overview of ZEPLIN III Design 127

5.6 Summary 130

Chapter 6 : Monte Carlo Simulations of ZEPLIN III **131**

6.1 Introduction 131

6.2 Light Collection in ZEPLIN III 132

6.2.1 Geometry and Materials Definition 132

6.2.2 Physics Processes In Light Collection Simulation 135

6.2.3 Procedure for Light Collection Simulation 137

6.2.4 Results of Light Collection Simulations 137

6.2.5 Results of Light Collection Simulations in the Xenon Gas Gap 142

6.2.6 Black Surfaces and Lambertian Reflection 145
6.2.7 Summary of Light Collection Simulations 146
6.3 Electron Drift in ZEPLIN III 146
6.3.1 Electric Field Simulation 147
6.3.2 Electron Drift Simulation 151
6.3.3 Drift Velocity Simulation 154
6.3.4 Electron Yields for Gamma Rays in Liquid Xenon 155
6.3.5 Electron Extraction from Liquid Xenon 156
6.4 Electroluminesence and Event Reconstruction 157
6.4.1 Electroluminescence Calculations 158
6.4.2 Event Reconstruction 160
6.4.3 Summary 170

Chapter 7 : Background and Data Analysis Simulations 171

7.1 Introduction 171
7.2 Gamma Ray Transport 172
7.2.1 Interaction Cross Sections 172
7.2.2 Gamma Simulation Code Structure 173
7.2.3 Geometry and Material Parameters 178
7.2.4 Diagnostic Testing and Limitations 180
7.3 ^{238}U and ^{40}K Background 187
7.3.1 Deposited Energy Spectra 188
7.3.2 Light Code Application to ^{238}U and ^{40}K Background . . 196
7.3.3 Results from Background Analysis and the Discrimination Power of ZEPLIN III 199
7.4 Summary 204

Chapter 8 : Sensitivity of ZEPLIN III **205**

8.1 Introduction 205

8.2 Sensitivity Plot Formulas 206

8.3 Values for Sensitivity Calculations 207

8.4 Results From Sensitivity Calculations 207

8.5 Summary 208

Chapter 9 : Conclusion **210**

List of Figures

1.1 Schematic of a Stars Motion in the Galactic Plane 21

1.2 Blackbody Spectrum of the CMBR 23

1.3 Full Sky Differential Temperature Map of the CMBR 24

1.4 Nucleosynthesis Predictions of the Abundances of the Light Elements 26

1.5 Hubble Diagram for Type Ia Supernovae 31

1.6 Large Scale Structure Power Spectra from PSCz Galaxy Survey 33

1.7 Schematic of the Geometry for Gravitational Lensing 36

1.8 Rotation Curve for the Milky Way 38

1.9 Microlensing Event Towards the LMC 39

1.10 Limits on the Possible Contribution of MACHOs to Galactic Dark Matter 40

2.1 Nuclear Recoil Scattering in the Laboratory Frame 45

2.2 Nuclear Recoil Scattering in the Centre of Mass Frame 46

2.3 SUSY WIMP Spin-Independent and Spin Dependent Cross Section Parameter Space 50

2.4 Vertical Muon Intensity as a Function of Depth 53

2.5 Schematic of Earth's Motion about the Sun 58

2.6 Exclusion Plot of Current Limits from DAMA and CDMS Groups 61

2.7 DAMA Annual Modulation Signal 62

3.1 Maximum Nucleus Recoil Energy for Variable WIMP and Target Masses 66

3.2 Schematic of Xenon Scintillation and Ionisation Mechanism . . . 69

3.3 The Basic Design of a Photomultiplier 74

3.4 Low Temperature Photomultiplier Experimental Setup 77

3.5 Room Temperature Linearity Test of 9829QA Photomultiplier . 78

3.6 Low Temperature Linearity Test of 9829QA Photomultiplier . . 79

3.7 Room Temperature Rate Test of 9829QA Photomultiplier 80

3.8 Low Temperature Rate Test of 9829QA Photomultiplier 81

4.1 Schematic of Xenon Purification Scheme 83

4.2 Photograph of the Xenon Purification System 85

4.3 Sketch of Distillation Tube Setup 90

4.4 Mass Spectrum Time Profile of Pumping on Solid Xenon 91

4.5 Sketch of Adsorption Process onto Metal Surface 92

4.6 Mass Spectrum Time Profile During Baking of Distillation Tube 93

4.7 Schematic of Distillation Process 94

4.8 Schematic of Test Chamber and Outer Vacuum Jacket 95

4.9 Schematic of Test Cell Arrangement 96

4.10 Energy Spectrum for 5.49 MeV α-particles in Liquid Xenon . . . 97

4.11 Comparative Reflectivity Measurements for PTFE, Al(Mylar) and Stainless Steel 97

4.12 Energy Spectrum for Low Energy Gamma-rays in Liquid Xenon 98

4.13 Average Pulse Shapes of Gamma-rays and α-particles in Liquid Xenon 99

List of Figures

4.14 Time Constant Histograms for α-particles and Gamma-rays in Liquid Xenon 100

4.15 Schematic of Neutron Beam Test Facility 101

4.16 ^{57}Co Energy Spectrum for Liquid Xenon Test Cell 102

4.17 Neutron Recoil Energy Spectrum for Test Cell 103

4.18 Quenching factor of Xenon as a Function of Nuclear Recoil Energy 104

4.19 Photograph of the ZEPLIN I Inner Target Vessel 106

4.20 Schematic of the Veto/Target Arrangement for ZEPLIN I 107

5.1 Typical Drift Velocity Curve for Electrons in a Noble Gas 110

5.2 Schematic of the Liquid/Gas Interface in Two Phase Detector . 115

5.3 Design Drawings of a Two Phase Prototype Detector 118

5.4 Sketch of Internal Electrode Structure in Two Phase Prototype Detector 119

5.5 Signal from Two Phase Prototype Detector due to α-particle Interaction 120

5.6 Histogram of Secondary/Primary Signal Ratio in Two Phase Prototype Detector 122

5.7 Integrated Charge Ouput from Electron Drift in Two Phase Prototype Detector 124

5.8 Sketch of Am-241 Source and Lead Boat in Two Phase Prototype 125

5.9 Design Drawing of ZEPLIN III Detector 126

5.10 Sketch of ZEPLIN III Design Drawing 128

5.11 Sketch of Dynode Disc Arrangement In ZEPLIN III 129

6.1 Schematic of the Light Simulation Geometry 132

6.2 Sketch of Photomultiplier Array in ZEPLIN III 135

6.3 Positions of Simulated Events in Light Simulation 138

6.4 Histogram of Light Collection Efficiency in Liquid Xenon Volume of ZEPLIN III 139

6.5 Distribution of Sources According to Light Collection Efficiency 140

6.6 Light Collection Efficiency at Different Levels in Liquid Volume of ZEPLIN III 141

6.7 Light Collection Efficiency in Gas Volume of ZEPLIN III 143

6.8 Light Collection Efficiency Distribution in Gas Volume of ZEPLIN III 144

6.9 Light Collection Efficiency in Gas Volume of ZEPLIN III, Black Surfaces 145

6.10 Finite Element Mesh for Electric Field Simulations 148

6.11 Field Distribution in ZEPLIN III 149

6.12 Equipotential Distribution in ZEPLIN III 150

6.13 Field Distribution Near Electrodes in ZEPLIN III 151

6.14 Projected Stopping Power of Xenon for Electrons 152

6.15 Electron Trajectories in ZEPLIN III Electric Field 153

6.16 Electron Drift Velocities in Liquid Xenon as a Function of Applied Field 155

6.17 Electron Yield for Gamma-rays in Liquid Xenon 156

6.18 Fits to Electron Yield Data 157

6.19 Electron Extraction Probability as a Function of Applied Electric Field in Liquid Xenon 158

6.20 Vapour Pressure of Xenon as a Function of Temperature 160

6.21 Simulated Normalised Response of Photomultiplier Array to Event on Central Axis of ZEPLIN III 161

6.22 Simulated Normalised Response of Photomultiplier Array to Event Off the Central Axis of ZEPLIN III 162

6.23 Histogram of Events Giving Zero Electroluminescence for Single Electron Extraction 164

6.24 Reconstructed Event Positions for Single Electron Extraction . . 164

6.25 Reconstructed Event Positions for Single Electron Extraction and Minimum of 10 Detected Photons 165

6.26 Histograms of Reconstructed Position Accuracy 167

6.27 Histograms of Reconstructed Position Accuracy for Four Electrons Removed from Liquid Volume 168

6.28 Scatter Plot of Reconstructed Position Accuracy for Four Electrons Removed From The Liquid Volume 169

7.1 Cross Sections for Gamma-ray Interactions with a Xenon Atom 173

7.2 Box Diagram for Gamma-ray Transportation Code 174

7.3 ^{238}U Line Spectrum 175

7.4 Sketch of the Compton Veto and ZEPLIN III Detector Arrangement 179

7.5 Integrated Probability Distribution Functions for Compton Scattering of Xenon Atom 182

7.6 Simulated ^{238}U Line Spectrum 183

7.7 Positions of Emission of Gamma-rays in Radioactive Background Simulations 184

7.8 Variation of the Ratio of the Compton Gamma-ray Energy to Incident Gamma-ray Energy as a Function of the Deflection Angle185

List of Figures

7.9 Simulated Paths in Liquid Xenon For 10keV and 100keV Gamma-rays. 190

7.10 Simulated Paths in Liquid Xenon For 1MeV and 10MeV Gamma-rays 191

7.11 Energy Depositions in Liquid Xenon from Photomultiplier Radoiactivity 192

7.12 Energy Depositions in Liquid Xenon from Photomultiplier Radoiactivity with Multiple Scatterings Integrated 193

7.13 Energy Depositions in Liquid Xenon after Removal of Vetoed Events 194

7.14 Energy Depositions in Liquid Xenon after Removal of Vetoed and Reverse Field Region Events 195

7.15 Simulated Trace from 19 Photomultipliers in ZEPLIN III 198

7.16 Energy Spectra from Background Radioactivity 199

7.17 Primary versus Secondary Signal Scatter Plot for Background Events 200

7.18 Histogram of Secondary/Primary Signal Ratio for Background Events 201

7.19 Plot of Secondary/Primary Signal Ratio for Background Events after Correction 202

7.20 Plot of Secondary/Primary Signal Ratio for Simulated Neutron Distribution 203

8.1 Spin Independent Limits of ZEPLIN III Detector 208

List of Tables

1.1 The COBE Satellite Detectors 22

1.2 Observational Values for Ω 31

2.1 Dark Matter Discrimination Techniques 55

2.2 Time Constant Differences for Neutrons and Gamma-Rays in NaI(Tl) 56

2.3 Current Proposed or Running Dark Matter Detectors 60

3.1 Physical Properties of Xenon 67

3.2 Singlet to Triplet Intensity Ratios for 1MeV Electrons and α-particles 70

3.3 Characteristics of 9829QA Photomultiplier 75

4.1 Gamma-ray Calibration Data for Neutron Test 102

6.1 Positions of Electrodes in Light Simulation 133

6.2 Positions of Mirror and Photomultiplier Housing in Light Simulation 134

6.3 Photomultiplier Positions in Light Simulation 134

6.4 Light Collection Efficiencies in the Liquid Volume of ZEPLIN III 142

6.5 Monte Carlo Input Variables 163

7.1 Volumes and Materials Used in ZEPLIN III Monte Carlo Simulation 180

7.2 Properties of the Elements Used in ZEPLIN III Simulation Code 180

7.3 Physical Properties of the Mixtures Used in ZEPLIN III Monte Carlo Simulation 181

7.4 Absorption Lengths of Gamma-rays in Liquid Xenon 186

7.5 Radioactivity Sources in Photomultipliers 188

8.1 Values for Sensitivity Calculations 207

CHAPTER 1

The Dark Matter Scenario

The dark matter problem has now become one of the most important scientific quandaries of our time. It has profound influence in cosmology, astrophysics, high energy physics and theoretical physics. Each of these disciplines, in one way or another, predicts the existence of dark matter. It is no surprise then that there is a huge global effort to uncover definite signatures from the dark matter. The discovery of dark matter by direct terrestrial searches would be an experimental scientific breakthrough, which, it could be argued, would have no parallel. The arguments for the existence of a non-luminous massive component to the Universe, that dominates ordinary visible matter on all scales, are overwhelming. However the dark matters form is still controversial. SuperSymmetric (SuSy) particles, massive neutrinos, MAssive Compact Halo Objects (MACHOS), axions and other forms of exotic matter are all potential candidates for dark matter.

This chapter examines the motivation behind the frenzy of scientific experimentation into the search for dark matter. In particular both the theoretical predictions and current experimental evidence are scrutinised. An overview of popular cosmological models, particle physics scenarios and theoretical physics motivations is given. Finally astrophysical evidence for the existence of dark matter is considered.

1.1 A Dark History

Previously described as the "*astronomy of the invisible*", the history of dark matter began with the detection of small fluctuations in the positions of Uranus and Sirius A. In 1844 F.W.Bessel deduced that the cause of the deviations in the position of Sirius A could be the presence of an as yet undetected gravitating companion. The French mathematician U. J. J. Le Verrier came to the same conclusion about the movements of Uranus. These predictions inspired astronomers to search for these dark massive objects and in 1846 J. G. Galle first observed the planet Neptune. In 1862 after significant advances in astronomical devices Sirius B was discovered and the binary system of Sirius A and Sirius B was recognised. These two seperate instances enabled astronomers with a new diagnostic tool, gravity. The astronomical community was now aware of the possibility that luminosity might not be the sole tracer of mass, gravitation it seemed had become an indispensable tool for the search for matter.

The first hint of a possible Galactic presence of dark matter seems to have been in 1922, when J. C. Kapteyn used the observed motions of nearby stars to calculate the total density of matter near the Sun. Kapteyn wrote in his abstract "it may be possible to determine *the amount of dark matter* from its gravitational effect" [1]. However, he remarks, "As matters stand at present it appears at once that this mass cannot be excessive" [1] in reference to the possible contribution of dark matter to the total mass density of the Universe. Utilising a similar method ten years later, J. Oort was led to conclude that as much as two thirds of the local mass density could be in the form of some unknown mass. Oort used a calculation based on the spatial density and perpendicular velocities of nearby stars, as a function of their height from the Galactic plane (Fig 1.1). By relating these observational quantities to the gravitational force acting on the stars, and using the formula in Equ 1.1, it is

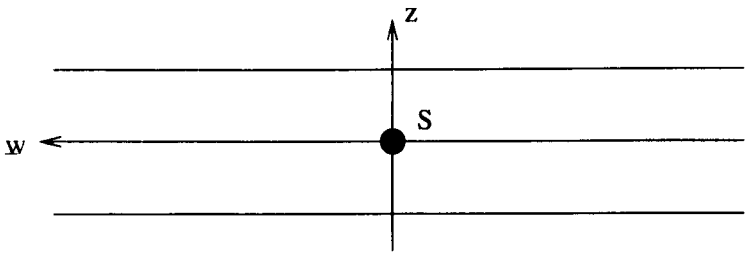


Fig. 1.1: A small section of the Galaxy near the Sun which is near the Galactic plane. w, z and space density are related to give total density of gravitating matter.

possible to measure ρ the total density of gravitating matter,

$$\rho = \frac{g_o}{4\pi G z_o} \tag{1.1}$$

where G is Newton's Gravitational Constant, g_o and z_o are constants of acceleration and height. Equ 1.1 is often referred to as Oort's Limit. Oort himself measured the local mass density to be $0.092 M_\odot pc^{-3}$†‡ , where the known mass in the form of visible stars at that time was only $0.038 M_\odot pc^{-3}$[2]. However, more recent calculations and observations of the solar neighbourhood, do not require a dark matter disk-like distribution to account for these vertical proper motions of stars[3].

Since Oort's suggestion of the presence of a dark matter component to the Galactic mass in 1932, the explanation of its form, of its origin and its role as a fundamental constituent of the Universe, have all become intense areas of research. The seed of the dark matter problem had been sown.

1.2 Cosmology and Dark Matter

In this section we will explore the current cosmological motivations for the existence of dark matter. In particular we examine the densities of types of dark

†1 $M_\odot$= 1 solar mass $\sim 2 \times 10^{30}$kg
‡1 pc = 3.10×10^{16}m

matter which one expects from current cosmological models. The problem of structure formation is also mentioned with reference to the Cosmic Microwave Background Radiation (CMBR) isotropy and Large Scale Structure (LSS) in the Universe. Lambda Cold Dark Matter (ΛCDM) and Cold Hot Dark Matter (CHDM) scenarios are introduced as modern popular cosmological models.

1.2.1 Modern Cosmology

The Cosmological Principle, on which modern cosmology takes as its starting hypothesis, states that the Universe is homogenous and isotropic. In 1989, the COsmic Background Explorer (COBE) satellite was launched, with a mission to measure the CMBR. This radiation is believed to be the primaeval remnants of Hot Big Bang (HBB) photons which decoupled from matter after atoms formed in the early Universe. The photons were then free to stream through the Universe and cool. The expected signature of the photons would be a pure blackbody relationship at a temperature of around 3K. COBE was tuned to search for these photons in the wavelength range between 1μm to 1cm utilising three detectors [4].

Detector	Wavelength	Accuracy
Far Infrared Absolute Spectrophotometer	100μm$\Rightarrow$1 cm	7 degrees
Diffuse InfraRed Background Experiment	1$\Rightarrow$300μm	0.7 degrees
Differential Microwave Radiometer	3mm$\Rightarrow$9.5mm	7 degrees

Table 1.1: Table of the three detectors aboard the COBE satellite, their wavelength ranges and accuracies.

Fig 1.2 is the background spectrum measured by the FIRAS instrument on board the COBE satellite. The accuracy to which the results fit the expected blackbody curve is one of the most striking features of the experiment, and, in fact, one of the most important triumphs in modern experimental cosmology. The absolute temperature measured was 2.728 $\pm$0.004 K (95% CL) [5], which

agreed with the first measurement of this phenomenon by Penzias and Wilson in 1965 [6]. One expects this blackbody form of the energy spectrum as a

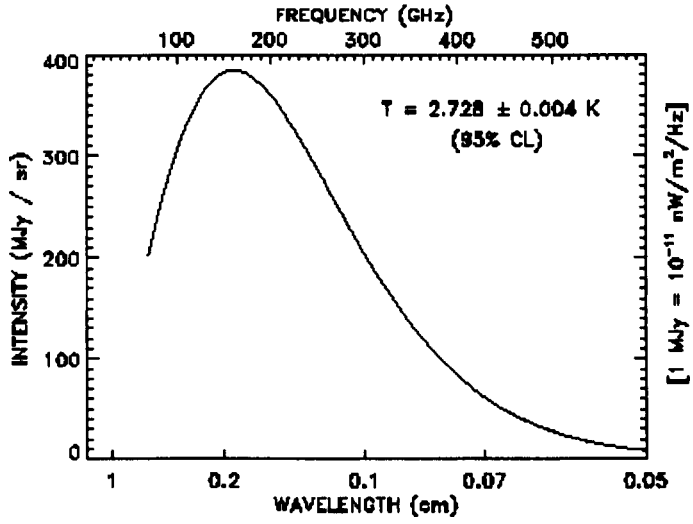


Fig. 1.2: The FIRAS measurement of the energy spectrum of the CMBR. Errors are at a level that they are indistinguishable from the theoretically fitted curve, the rms deviations are less than 50 parts per million of the peak of the CMBR [5].

result of the scattering of the photons before decoupling. The temperature can be derived from the expected 'cooling' rate of the photons as a function of the age of the Universe, or, more specifically, the scale factor of the Universe.

As well as producing the form of the spectrum of the CMBR, COBE was also able to construct full sky maps of the temperature distribution of the CMBR. Fig 1.3 is one such map constructed from data taken with the DMR instrument at 31, 53, and 90 GHz[7]. Whilst the data is consistent with isotropy in the background to 1 part in 10^5, maps of this type indicate anisotropies at the level of $\Delta T/T \approx 6 \times 10^{-6}$. The fluctuations in the spectrum cannot be explained away by systematic errors, Galactic emission or the dipole anisotropy, and hence are determined to be a primordial fingerprint of the energy density of the early Universe. Accurate measurements of the CMBR anisotropies can

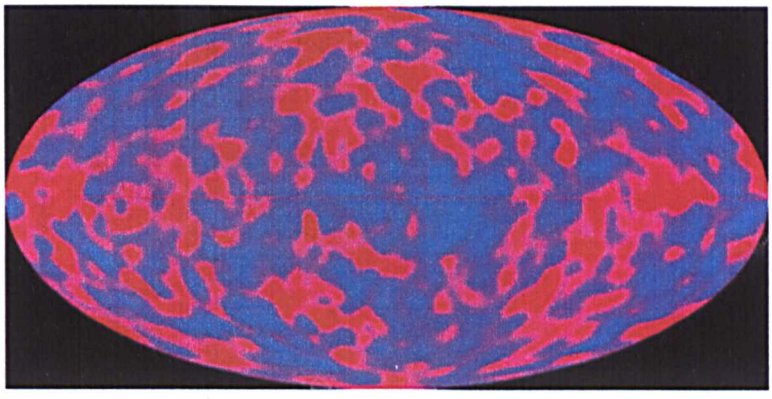


Fig. 1.3: A full sky differential map of the CMBR. This plot is from data taken by the Differential Microwave Radiometer (DMR) instrument. Galactic emission and dipole anisotropies have been subtracted. The data is taken from 2 years running of the instrument.[5]

therefore be used as a stringent constraint on cosmological models, as they must be capable of reproducing this distribution.

The COBE measurements of the CMBR, in conclusion, give the following insights:

- the CMBR has a blackbody form and is isotropic to 1 part in 10^5
- anisotropies exist on large scales which indicate energy fluctuations in the early Universe.

These conclusions fortified the HBB Universe scenario, but simultaneously encouraged the formulation of new, more complex, theories that would predict the fundamental anisotropies.

The Mathematical Formulation of Modern Cosmology

As mentioned previously, modern cosmology is based upon the Cosmological Principle. When combined with Einstein's General Relativity one can derive the Robertson-Walker metric:

$$ds^2 = dt^2 - a^2(t)\left[\frac{dr^2}{1-kr^2} + r^2(d\theta^2 + sin^2\theta d\phi^2)\right] \tag{1.2}$$

The metric defines an expanding, homogeneous and isotropic spacetime, where $a(t)$ is the scale factor, k represents the curvature, and r, θ, ϕ are spherical coordinates on the surface of a world sphere. The curvature term k can take values +1, 0, or -1 for a closed, flat or open universe. In more detail, $a(t)$ follows the Friedmann Equations:

$$\frac{d^2a}{dt^2} = -\frac{4\pi}{3}G(\rho + 3p)a \tag{1.3}$$

$$H^2 + \frac{k}{a^2} \equiv \left[\frac{\frac{da}{dt}}{a}\right]^2 + \frac{k}{a^2} = \frac{8\pi}{3}G\rho + \frac{\Lambda}{3} \tag{1.4}$$

Here ρ is the energy density of matter in the universe, H is Hubble's constant, more often written as $100h^{-1}$ where $0.5 \leq h \leq 1$, p is pressure density, and Λ is the Cosmological Constant.

If we consider a flat universe, k=0, with no Cosmological Constant, then Equ 1.4 relates H and ρ uniquely. In this case ρ is known as the critical density, ρ_c, and is given by:

$$\rho_c = \frac{3H^2}{8\pi G}. \tag{1.5}$$

The critical density gives us our definition for Ω_0:

$$\Omega_0 = \frac{\rho}{\rho_c} \tag{1.6}$$

Ω_0 is then our measure of the total mass density of the Universe.

The cosmology presented so far is very basic, and is only applicable to a universe that satisfies the conditions inferred by the Cosmological Principle. There is no physics used to set up these initial conditions in HBB theory; for this we need to invoke early universe physics where theories endeavour to provide physical bases on which experimental evidence, such as the CMB anisotropies, can be understood. That said, HBB Nucleosynthesis (HBBN) theory has yielded understanding of the early Universe, in particular the calculations of present

day light element abundances. HBB theory suggests that at epochs when $k_b T \approx 10$MeV conditions were such that synthesis of light elements could occur. Predictions of the elemental ratios for species such as D,^{4}He,^{3}He and ^{7}Li to hydrogen, at early times, can be related to pre-galactic abundances of elements which can be inferred from observational data. Figure 1.4 shows a recent

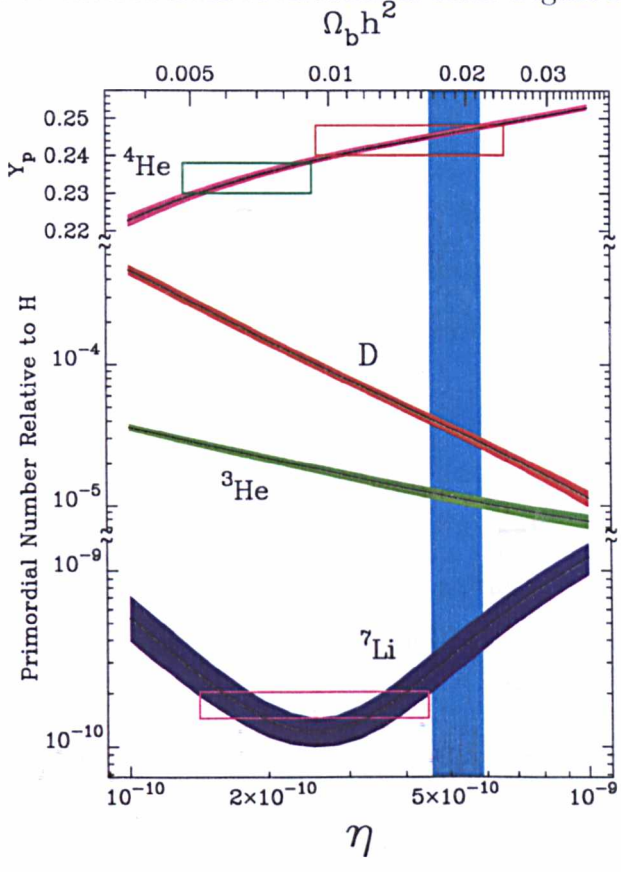


Fig. 1.4: Plot of the 95% confidence intervals for HBBN predictions for D, ^{4}He,^{3}He and ^{7}Li. Solid boxes indicate 95% confidence level abundances from observation.[8]

plot of the 95% confidence intervals for HBBN predictions of D, ^{4}He, ^{3}He and ^{7}Li relic abundances, taken from [8]. These bands are predicted from Monte Carlo simulations of nuclear interactions in the early Universe. Abundances for D, ^{4}He and ^{7}Li have all been measured in gas where there has been little or no stellar processing (this can alter the true ratios of the relic abundances). For the three elements, the values are near to those predicted by HBBN theory.

There are problems with the formulation of standard cosmology which require

new understanding:

- *The Horizon Problem:* from the earlier discussion of the CMBR we noted the isotropy of the radiation, with little further comment. The logical conclusion of this observation is that microwave photons across the full angular scale of the sky are in thermal equilibrium at the same temperature. This implies that at some epoch the photons were interacting in such a way as to produce the characteristic CMBR. Now photons travel with speed c. Therefore, given a time interval Δt, their maximum possible interaction distance is cΔt. This distance is known as a horizon and, if we apply this principle to the Universe, we have:

$$d_H(t) = a(t) \int_{t_*}^{t} \frac{dt}{a(t)}. \tag{1.7}$$

For the CMBR to have been created from photon interactions in the standard HBB model, the photon horizon at the time of matter-radiation decoupling would have to be equal to, or larger than, the current horizon distance. In fact:

$$\int_{t_*}^{t_{dec}} \frac{dt}{a(t)} \ll \int_{t_{dec}}^{t_0} \frac{dt}{a(t)}. \tag{1.8}$$

It is true to say that any two areas of the night sky separated by at least 2 degrees would be causally separated in HBB theory. The homogeneity of the Universe cannot therefore be explained by standard cosmology. Indeed this argument can be explored further, as it also disallows intrinsic irregularities in the last scattering surface to be larger than the horizon. However, these perturbations are seen by COBE on scales of a few degrees or so. If these large angle perturbations are indeed intrinsic to the last scattering surface, and these perturbations are the seeds of large scale structure formation, then it follows that the simple standard HBB theory does not provide an adequate explanation for either as it is constrained by this Horizon Problem.

The Dark Matter Scenario

- *The Flatness Problem:* using Equ 1.5 and Equ 1.4 we can write;

$$|\Omega - 1| = \frac{|k|}{a^2 H^2}. \tag{1.9}$$

Equ 1.9 suggests that as the Universe evolves, Ω is a rapidly varying function of time constantly being driven away from unity. Today we are sure that Ω is at least within an order of magnitude of unity, which means that in the past it must have been even closer. It can be shown that if Ω varied from unity by one part in 10^{55} when the age of the Universe was 10^{-35}sec, then the Universe would either have already collapsed or the current measured density would be an order of magnitude less [12]. This is known as the flatness problem. Why is the Universe so close to the critical density, Ω=1?

- *Other Problems With Standard Cosmology:* particle physics theories such as Grand Unified Theories (GUTs) which go beyond the Standard Model to unite the strong, weak and electromagnetic forces, predict the creation of magnetic monopoles as topological defects in the Higgs field after spontaneous symmetry breaking [13]. These monopoles are created in cosmologically significant quantities in the early Universe, but experimentally have never been observed.

1.2.2 Inflation and Ω

In the previous subsection we introduced simple modern cosmology and some examples of its success and failure. Here we look at an extension to that scenario - inflationary theory. First developed by Alan Guth in the early eighties [14] inflation was conceived to solve the problems associated with simple standard cosmology. The idea, with hindsight, is disarmingly obvious but extremely powerful. The classic example of inflation, which we will use to demonstrate the principle, is observed when we take the equation of state

(relating the pressure and density of the early Universe):

$$p = -\rho \tag{1.10}$$

where p is the pressure and ρ is the energy density. In this case the solution of Equ 1.3 for $a(t)$, the scale factor, is given by Equ 1.11.

$$a(t) \propto exp(Ht) \tag{1.11}$$

This implies an exponential growth in the scale factor of the Universe. Another consequence of inflation is that the Hubble length decreases during inflation. Coupling these two factors and applying them to Equ 1.9 demonstrates that inflation literally drives Ω to unity. Furthermore, realising that the Hubble length can be regarded as the inverse of the causality boundary, we can see that, in the inflation model, this boundary is increased. Hence regions of space that appear out of causal contact now, were in fact, during inflation, 'squeezed' together and hence able to interact, and, the choice of the right parameters in the model can reproduce the characteristic COBE power spectra.

Inflation has given us a model in which we can solve the problems associated with the simple Robertson-Walker universe. We have yet to come across the theoretical motivations for dark matter. To address this we must examine Ω and its constituents more closely. Ω is the total energy density, and can be written as a sum of the following:

$$\Omega = \Omega_b + \Omega_\Lambda + \Omega_{CDM} + \Omega_{HDM} \tag{1.12}$$

- Ω_b: the baryonic matter energy density
- Ω_Λ: the Cosmological Constant energy density
- Ω_{CDM}: the cold dark matter energy density
- Ω_{HDM}: the hot dark matter energy density.

The Dark Matter Scenario

Let us examine these individually, and mention some current estimates on the values of each. Ω_b is baryonic matter energy density. HBBN theory and experimental measurements of the abundances of D,^{4}He,^{3}He and ^{7}Li can yield values for Ω_b. Studies of distant Quasar Absorption line Systems (QAS) are thought to be a reliable way to estimate the primordial deuterium abundance. Data from these studies can be used in Monte Carlo simulations of HBBN theory to predict the baryon to photon ratio, η, and the effective number of neutrinos, N_ν, the only two free parameters in the models. From these, the baryonic contribution to the average energy density of the Universe can be estimated. Below are results taken from recent work [8, 16]:

$$D\text{-}abundance\ Y_D = (3.4\pm0.3)10^{-5}$$
$$\Omega_b h^2 = 0.019 \pm 0.0024$$
$$1.7\leq N_\nu \leq 3.3,\ 4.0\leq \eta_{10} \leq 5.7,\ 0.015\leq \Omega_b h^2 \leq 0.021$$

where $0.5\leq h\leq 1$ represents the uncertainty in the Hubble constant, H. CMBR constraints on Ω_b have been fortified by the most recent measurements of the MAXIMA and BOOMERANG balloon borne experiments [9, 10]. Best fit models to the angular power spectrum of the CMBR incorporating these results suggest $\Omega_b h^2=0.022^{+0.004}_{-0.003}$ [11].

The second term in Equ 1.12 is the contribution of the vacuum energy, or Cosmological Constant, to the total energy density. This has become of increasing interest as astronomical observations have indicated that Ω_Λ may be non-zero, and perhaps even dominate Equ 1.12. Results from two groups studying high redshift Type Ia supernovae suggest that the Hubble diagram for these objects is best fitted by models where Ω_Λ=0.7, Ω_m=0.3 ($\Omega_m = \Omega_b + \Omega_{CDM} + \Omega_{HDM}$) see Fig 1.5 [18] [19]. However, at the time of writing, it would be incorrect to insist that the value $0\leq \Omega_\Lambda \leq 0.7$. Other work on determining the velocity of recession of high redshift objects, in particular gravitational lensing systems [20], are more consistent with Ω_m=1, Ω_Λ=0.

Before commenting on the final two contributions to Ω let us first consider some astronomical observations which are used to estimate the value of Ω. We have

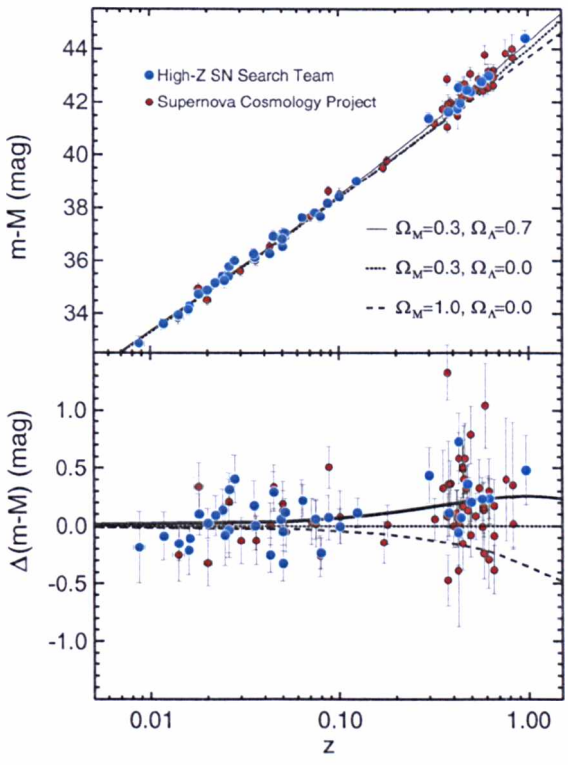


Fig. 1.5: Hubble diagram for Type Ia supernovae. Results from High-Z SN Search Team and Supernova Cosmology Project. [19]

so far theoretically argued that Ω should be close to unity. From Equ 1.12 and previous discussions, we conclude that non-baryonic matter must constitute a significant fraction of the Universe. Even taking the worst case scenario $\Omega_{nbm} \geq 0.27$. Observational efforts to measure Ω include the measurement of the mass to luminosity (M/L) ratios of galaxies, the use of a cosmic virial theorem and large scale flows. In Table 1.2 some current results are given. The values tabulated in Table 1.2 are taken from selected references, and are

Method	Value	Refs
M/L	$0.20h^{-1} \leq \Omega \leq 0.30h^{-1}$	[21]
Cosmic Virial Theorem	$0.27h^{-1} \leq \Omega \leq 0.72h^{-1}$	[22]
Large Scale Flow	$0.6h^{-1} \leq \Omega \leq 1.0h^{-1}$	[23]

Table 1.2: Observational values for Ω for M/L ratio, cosmic virial theorem and large scale flow techniques.

not conclusive. There are problems associated with each of these methods, for example, the assumption in the M/L measurements - that the galaxies and X-ray gas emissions trace in totality the mass of the cluster - is unlikely. This does not allow for possibly extended dark haloes which would lead to an underestimation of the cluster mass and hence reduce the observed value for Ω. It is difficult to find consistency in the values for Ω given by these differing observational techniques. However they all indicate that Ω is certainly of order unity.

Finally in this brief analysis, we come to the contributions of Ω_{CDM} and Ω_{HDM} to Equ 1.12. These two forms of dark matter are inferred from the shortfall of baryonic mass in the Universe. They provide invaluable channels for structure formation in the early Universe. CDM refers to dark matter made up of particles that were travelling at non-relativistic velocities at the time of matter-radiation decoupling. Conversely, dark matter particle candidates that were travelling relativistically at $t=t_{dec}$, are referred to as HDM. In structure formation they play contrasting roles. CDM particles, due to their higher mass, freeze out of the primordial fields at earlier epochs than their HDM counterparts. They then begin to self- gravitate, become Jeans unstable and form areas of over-densities in the early Universe. These are thought to be the seeds for galaxy formation, such that when the Universe has cooled sufficiently, and normal baryonic matter is formed, it falls into the gravitational template constructed by the earlier evolution of the CDM. If this were the only mechanism for structure formation then it has been shown that, whilst galactic formation would take place, pure CDM models would produce too much fine structure. This can be avoided by introducing a relativistic component to the dark matter energy density, HDM. Due to the free streaming of HDM particles, small density perturbations are 'washed out', and the onset of initial gravitational collapse can be delayed, resulting in a reduction in the amount of small scale structure created by CDM. A powerful method for the determination of the mixing ratio of CDM to HDM is the analysis of galaxy clustering on

large scales. In this analysis a Fourier transform of the two point correlation function of galaxy distributions gives a power spectrum. The obtained spectrum can then be fitted by cosmological models and, by varying the mixing ratio (and a host of other parameters), the best fit models can be found. One such analysis, reported in [15], uses the PSCz galaxy survey and the CMB as data for cosmological model fits. Selected results from this analysis are shown in Fig 1.6.

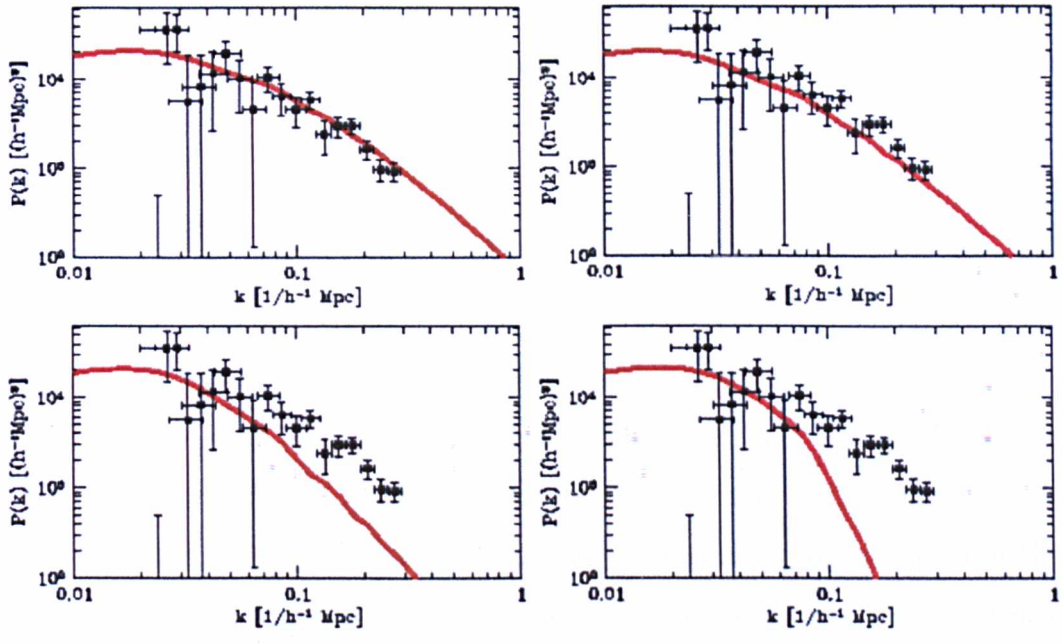


Fig. 1.6: LSS power spectra derived from the PSCz galaxy survey and selected fits from the 11 dimensional 'concordance' model of Tegmark et al [15]. The progression is clockwise from top left with the only varying parameter being f_ν the fraction of dark matter that is HDM : f_ν=0.0000, 0.0770, 0.3100, 0.9000.

The 'washing out' of small scale perturbations, by the addition of HDM to the overall cosmic energy density, can be clearly observed in these four diagrams. The feature to recognise is the steady decline of the tail at k values ≥ 0.03 $hMpc^{-1}$, where k is the wavenumber, for increasing fractions of the HDM contribution. The important point to take from these plots is that the HDM

fraction is constrained well below $f_\nu = 0.077$.

In conclusion, inflation provides a mechanism to drive Ω to 1 and solves the flatness and horizon problems. The contributions to Ω from a baryonic energy density, Ω_b, and a Cosmological Constant energy density, Ω_Λ, are too low to close the Universe. This implies another form of energy density in the Universe. Large Scale Structure observations suggest the HDM component of this other form of matter to be low. Therefore, theoretically, we must insist that there exists a nonbaryonic massive component to the energy density of the Universe.

1.3 Astrophysical Observations of Dark Matter

In this section the direct astrophysical evidence for dark matter is presented. Astronomical observations can be used to probe the form of gravitational potentials in astrophysical systems. The total mass of the system can be calculated and compared to the mass of visible matter. In many examples, these two masses are not equal and it is from this that we infer a dark matter component. Observations of this kind do not give information on the form of the dark matter. In the introduction to this chapter the local dark matter density was discussed in the context of the Oort limit. In what follows, extragalactic observations are focused upon.

1.3.1 Spiral Galaxy Rotation Curves

High resolution spectrometry allows the measurement of velocities of objects in spiral galaxies. Assuming Newtonian mechanics applies on galactic scales, and that the mass of the galaxy is concentrated at the centre, the velocity of objects as a function of radius r would be expected to fall as $1/\sqrt{r}$. In fact when measured, the velocity curves of spiral galaxies remain constant for $r >$10kpc. High resolution observations of the 21cm HI line indicate that flat

rotation curves continue outside the luminous boundary of the galaxy. UGC 2885 has the largest known HI disk of radius 120kpc for H_o=50kms^{-1}. The rotation curve out to this radius is flat [24]. Given that the measured rotation curves are flat, and the expected fall is $1/\sqrt{r}$, this implies a mass component to the galaxy that increases linearly with r. The evidence from galactic rotation curves suggest that galaxies reside within a halo of dark matter. The morphology of this halo is currently unknown. Typically when referring to direct searches for dark matter it is assumed that the halo is spherically symmetric and isothermal. The density profile is then:

$$\rho_d(r) = \rho_0 \frac{a^2}{a^2 + r^2} \tag{1.13}$$

where $\rho_d(r)$ is the density of dark matter at radius r, ρ_0 and a are the halo core density and radius respectively.

Galactic rotation curves give M/L of $\sim$ 10 - 20 [25]. If galaxies were comprised mainly of stars one would expect M/L $\sim$ 2.

1.3.2 Galaxy Cluster Dynamics

The earliest evidence for the existence of extragalactic dark matter comes from the measurements of galactic velocity dispersions in the Coma cluster [26]. The observed dispersion velocity of galaxies exceeds the cluster escape velocity if the only contribution to the gravitational field comes from the luminous matter. Recent measurements from [27] estimate the M/L value for the Coma cluster to be $\sim$ 160.

Applying similar virial techniques to larger systems, for example the Virgo supercluster, M/L values tend to increase. For the Virgo cluster M/L $\sim$ 450 [28].

1.3.3 Gravitational Lensing

Einstein's General Theory of Relativity states that spacetime is curved by massive objects. Light rays passing a massive body are therefore bent accordingly as they follow the geometry of spacetime. The angular deflection $\hat{\alpha}$, of a photon passing a body of mass M, is given by:

$$\hat{\alpha} = \frac{4GM}{c^2\xi} \tag{1.14}$$

where ξ is the impact parameter. Equ 1.14 was derived by Einstein in 1915. That light is bent by objects suggests that a massive object can act as a lens for light from a distant object. Fig 1.7 shows the lensing system to consider. Following the discussion in [29] it can be shown that in the case of a point

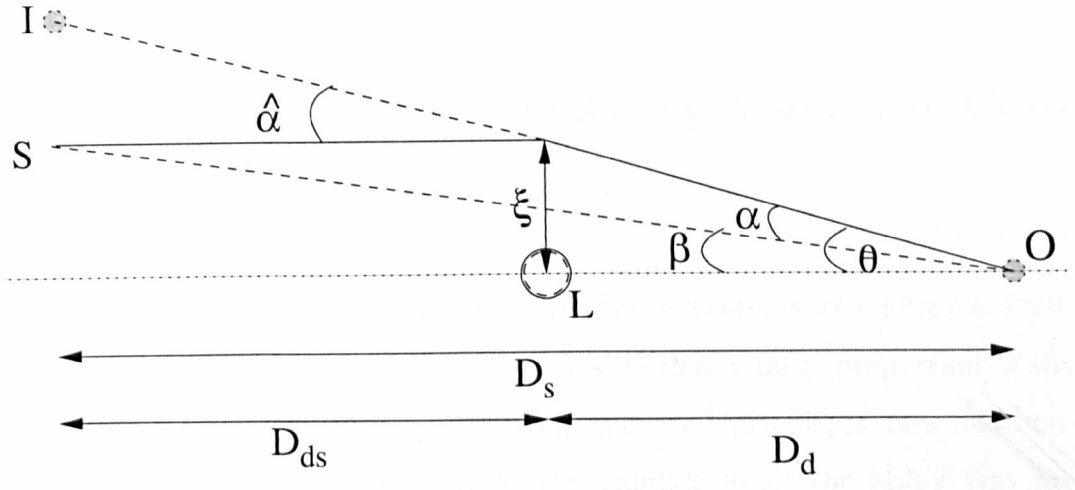


Fig. 1.7: Schematic of the geometry for gravitational lensing. The source object S is lensed by the massive object at O. The deflection angle is $\hat{\alpha}$ and the image is rendered at I. ξ is the impact parameter. The optical normal is the line that passes through the positions O and L

source and lens, the lensing equation is:

$$\theta^2 - \beta\theta - \frac{4GMD_{ds}}{c^2 D_d D_s} = 0 \tag{1.15}$$

where θ is the angle subtended to the optical normal by the image I, β is the angle subtended by the point source to the optical normal in the case of no lensing, D_{ds} is the distance between the point source and the lens, D_d is the distance between the lens to the observer and $D_s = D_{ds} + D_d$. The solution to the quadratic in Equ 1.15, setting $\theta_E^2 = 4GMD_{ds}/c^2D_dD_s$ is:

$$\theta = \frac{\beta \pm \sqrt{\beta^2 + 4\theta_E^2}}{2}. \tag{1.16}$$

where θ_E is known as the Einstein angle. The angular separation of images therefore is dependent on the mass of the lensing object. Where the separate images are unresolvable, the effect of lensing can be seen in the light amplification of an image. Recent results from weak lensing surveys give M/L values of between 160±60 (cluster MS0419.0-3848) and 420±110 (cluster MS2307.9-4328) [30]. Again the suggestion of a large dark matter component to the mass distribution is inferred by these observations.

1.4 Dark Matter in the Milky Way; The Candidates

The implication so far from the astrophysical observations, cosmological arguments and HBBN simulations/observations, is that a large proportion of the matter in galaxies, clusters, superclusters and the Universe, is dark and non-baryonic. In this section the dark matter candidates for the Milky Way are considered. The evidence so far presented indicates that galactic dark matter is present in galaxies similar to our own. In fact there is direct evidence for the existence of dark matter in the Milky Way. Consider the rotation curve for the Milky Way in Fig 1.8, taken from [31]. As expected from the earlier discussion, the curve flattens, indicating the presence of a dark matter component in the mass distribution of our Galaxy. However, the possibility of dark baryonic matter comprising the entire missing mass of galaxies has not been ruled out. In the next section this possible baryonic contribution is discussed.

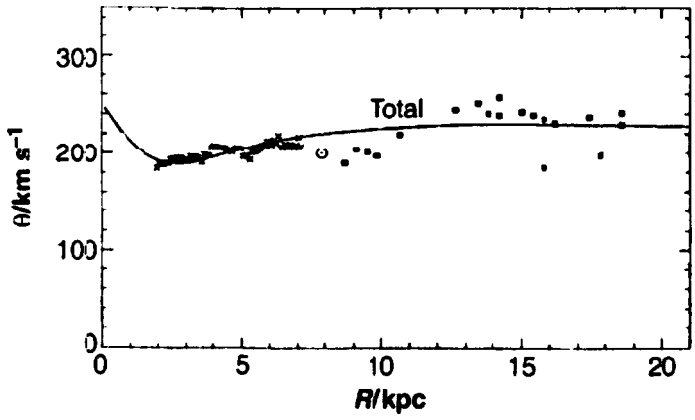


Fig. 1.8: Rotation curve for the Milky Way derived from the 21cm HI line measurements.

1.4.1 Dark Baryonic Matter in the Milky Way

In the previous section on gravitational lensing it was mentioned that object images can be amplified due to lensing by a massive object. Dark baryonic objects such as brown dwarfs - the relics of stars too small to initiate hydrogen burning - in the halo of our galaxy can be detected using this phenomenon. By constantly monitoring the brightness of distant stars this effect can be detected. Should a dark massive object pass between the earth and the star, a time symmetric brightening of the luminosity of that star occurs. This lensing effect is decribed by Equ 1.17,

$$A(t) = \frac{u(t)^2 + 2}{u(t)\sqrt{u(t)^2 + 4}} \tag{1.17}$$

$$u(t) = \left[u_{min}^2 + \left[\frac{2(t - t_0)}{\hat{t}}\right]^2\right]^{1/2}$$

where $A(t)$ is the amplitude of light at time t, $u = \beta/r_E$, $r_E^2 = \frac{4GMD_dD_{ds}}{c^2D_s}$ is the Einstein radius, t_0 is the time of peak amplification, $\hat{t} = 2r_E/v_\perp$ is the duration of the microlensing event, $v_\perp$ is the transverse speed of the dark object and u_{min} is the value of u when $A = A_{max}$.

Stars have been monitored in the Large Magellenic Cloud(LMC) by the MACHO and EROS groups, in the Small Magellenic Cloud by MACHO, PLANET and OGLE and in Andromeda M31 by AGAPE. Events are identified by the time symmetric brightening of the monitored star. The light is monitored in the blue and red ends of the spectrum since microlensing amplification occurs equally over all of the spectrum, unlike other intrinsic variations in the starlight.

The most reliable and extensive data to date comes from the MACHO and EROS groups. A candidate event from the MACHO group data is shown in Fig 1.9. This plot shows the characteristics of a microlensing event, the symmetric time brightening and achromaticity of the lightcurves.

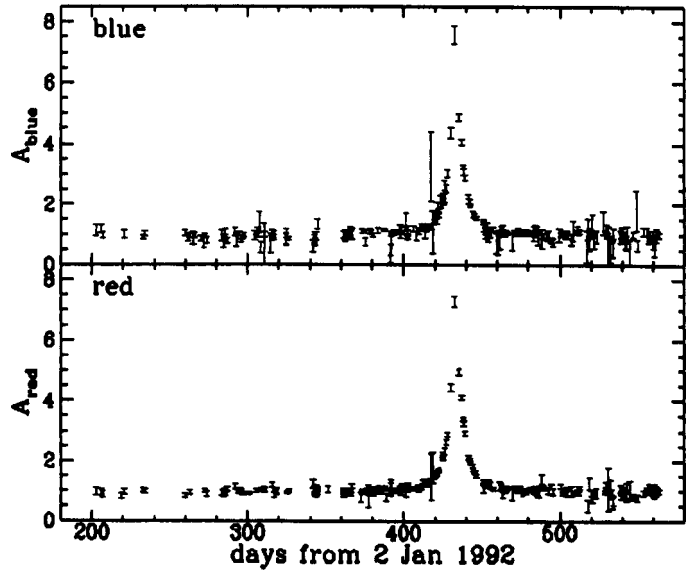


Fig. 1.9: Microlensing candidate data (LMC-1b) from an event towards the LMC, taken from [32].

In all, the MACHO project has detected over 20 microlensing events towards the LMC and SMC. The EROS group detected no events. However, no events

were detected by either group with a duration of between a few hours to 20 days. Analysis of this null data (see [33]) shows that dark compact objects with masses in the range $10^{-7}M_{\odot} - 2 \times 10^{-2}M_{\odot}$ do not contribute more than 10% of the Milky Way mass.

Analysis of the data containing actual event detections indicates that baryonic dark objects could be a substantial constituent of the halo. Fig 1.10 shows the likelihood contour plot for dark objects of mass, m, and halo fraction, f, taken from [34]. The favoured model of the object is seen to be a dark object with

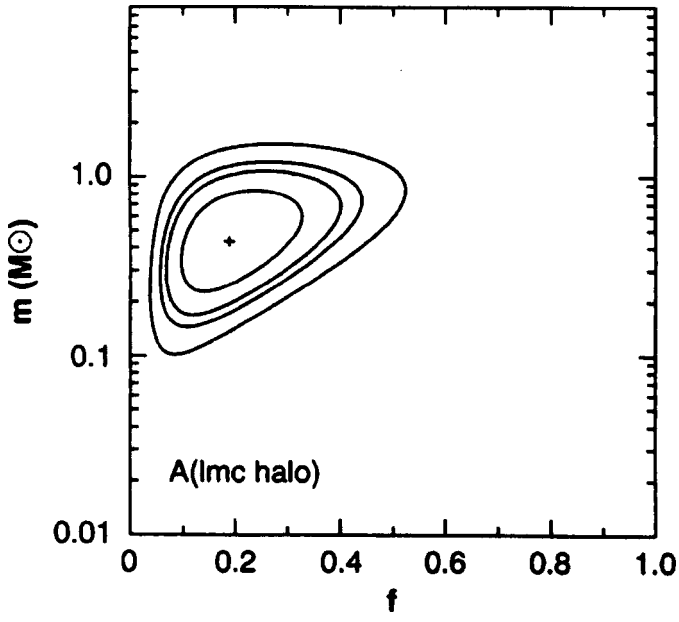


Fig. 1.10: Likelihood contours enclosing regions of 68%, 90%, 95%, 99% probability for dark objects having mass, m and constituting mass fraction, f of the Milky Way halo.

mass $\sim 0.5M_{\odot}$ contributing f$\sim$0.2 of the halo.

Whilst these events have been detected, the properties of the lensing objects, other than limits on their masses, are still unknown. Several hypotheses have

been put forward: cool (low luminosity) white dwarfs; brown dwarfs; primordial black holes; neutron stars and neutralino stars. Indeed there is still debate over whether these events actually occur due to dark objects in the Milky Way halo. The possibility exists that these events occur due to lenses in the host LMC or SMC [35]. Positional information is needed on the events, which requires further observation.

In summary, baryonic dark matter could contribute as much as 20% of the dark matter halo of the Milky Way. The form of these dark objects is unknown, their masses are predicted to be $\sim 0.5M_{\odot}$. Null data for events with short duration indicates that lower mass objects cannot contribute more than 10% of the halo.

1.4.2 Non-Baryonic Dark Matter Candidates

As discussed previously, there are two types of non-baryonic dark matter, CDM and HDM. First the candidates for CDM are explored.

Particle physics provides some strong candidates for the non-baryonic dark matter of the Universe. The 'Standard Model' has been the basis of particle physics for the last 33 years, and has been successful in describing the interactions between fundamental particles. However the Standard Model is unable to explain the origin of the Higgs field. The Higgs field, H_W, was introduced to give mass to the weak gauge bosons after the breaking of electroweak symmetry. To unify the electroweak fields with the fields associated with the strong force, a further symmetry is proposed at higher energies, $\sim 10^{14}$GeV - the GUT scale. This higher energy symmetry has associated with it another Higgs field, Φ. It is possible for the two Higgs fields to couple/mix via exchange of gauge bosons. The effect of this mixing is to increase the expected mass of the H_W field towards that of the higher Φ field. This is known in high energy physics as the hierarchy problem. To solve this problem it is necessary to extend the Standard Model. Supersymmetric (SUSY) theory when applied to the Standard Model avoids this hierarchy problem. SUSY, as a consequence of the

symmetry it invokes between fermions and bosons, requires that each fermion should have a partner bosonic sparticle†, and conversely each Standard Model boson should have an associated fermionic sparticle. With this extension to the Standard Model, the mixing terms between the H_W and Φ Higgs fields through boson exchange are now cancelled by the same mixing term but with fermionic sparticle exchange.

One of the features of supersymmetry is the concept of R-parity conservation. As the angular momentum of a particle and its superpartner differ by $\pm 1/2$ it is not possible to replace a sparticle by its Standard Model partner. Therefore, on the assumption that complete annihilation of sparticles is suppressed in the early Universe by the Hubble expansion, it follows that there could be a massive supersymmetric stable relic particle. This supersymmetric relic will be the Lightest Supersymmetric Particle (LSP), as high mass sparticles will have decay channels to this final state. The favoured candidate for the LSP is the neutralino, the composition of which is discussed further in Chapter 2.

The axion and its fermionic sparticle, the axino, are two other candidates for non-baryonic cold dark matter. The axion is a hypothetical low mass boson whose existence is invoked to solve the strong CP violation problem. The axino, its superpartner, is born from the combination of the Peccei-Quinn mechanism and SUSY. Like the axion, the axino has a low mass and hence a neutralino could decay to this final state. For further discussions on these candidates the reader is referred to [36].

The prime candidate for the HDM is a massive neutrino. Results from the Super-Kamiokande experiment suggest that the neutrino has non-zero mass due to observed neutrino oscillations [37].

†Nomenclature, sparticle: a superpartner particle arising from supersymmetry theory

1.5 Summary

This chapter has presented the current cosmological, astrophysical and particle physics motivations for the existence of dark matter. Modern cosmology favours a flat Universe, with $\Omega \sim 1$. HBBN predictions limit the contribution of baryonic matter to about 2% of the critical density. A non-zero Cosmological Constant suggested by results on observations of high redshift Type Ia supernovae, could account for 70% of the critical density. Coupling these phenomenon indicates a non-baryonic contribution to the Universal energy density. Further astrophysical observations indicate that our own galaxy resides within a dark matter halo, which cannot be wholly comprised of dark baryonic objects due to the recent microlensing results. Non-baryonic dark matter is therefore a constituent of the Universe and of the Milky Way. Supersymmetric extensions to the Standard Model of particle physics yield a possible candidate for non-baryonic dark matter, the neutralino. In the next chapter the detection of the neutralino is examined.

CHAPTER 2

Neutralino Dark Matter Detection

2.1 Introduction

In Chapter 1 the lightest supersymmetric particle, the neutralino, was suggested as a candidate for the missing matter in the Universe. In what follows, we restrict the main thread of the discussion to the detection of this particle. There are many terrestrial searches underway to detect neutralino dark matter. This chapter aims to explain the fundamentals of the direct searches techniques, contextualise the searches in the supersymmetric model and compare current experiments.

2.2 Fundamentals of Detection

The detection of the neutralino is based on its interaction with ordinary matter. The rate of interaction and expected energy depositions in target materials are examined here. The Galactic dark matter distribution is assumed to be spherical and virialised in the following analysis.

2.2.1 Elastic Scattering

Neutralino elastic scattering from a target nucleus releases energy in the form of scintillation, ionisation and heat (phonons). The number of interactions of this kind for a kilogram of target material per second, N_0, is

$$N_0 = n_{lsp}\sigma_s \mathrm{v}\frac{1000.L}{A} \tag{2.1}$$

where n_{lsp} is the number density (m^{-3}) of incident neutralino particles, σ_s (m^2) is the total scattering cross section of a single nucleus, v is the dark matter particle velocity (ms^{-1}), L is Avagadro's number and A is the atomic number of the target atom. The energy imparted to the target atom of the detector material can be calculated from kinematic arguments [38]. Fig 2.1 shows the kinematic system in the laboratory frame. The figure shows a particle (1 in the figure) incident on a target (2 in the figure). This particle collides with the target and is deflected at an angle θ from the straight ahead direction. The target is scattered at an angle ϕ. In Fig 2.1 p_1 and q_1 are the initial and final

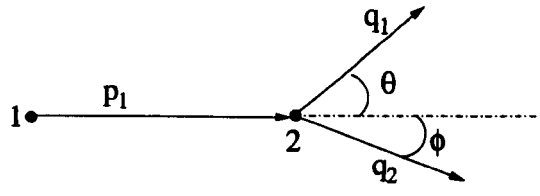


Fig. 2.1: Nuclear recoil scattering in the lab frame.

momenta of the incident particle, p_2 and q_2 are the initial and final momenta of the target nucleus. To relate the initial energy, E_i, and the recoil energy of the target nucleus, E_r, the centre of mass frame (COM) is used. Fig 2.2 shows the elastic scattering process in the COM frame. By definition, in the centre

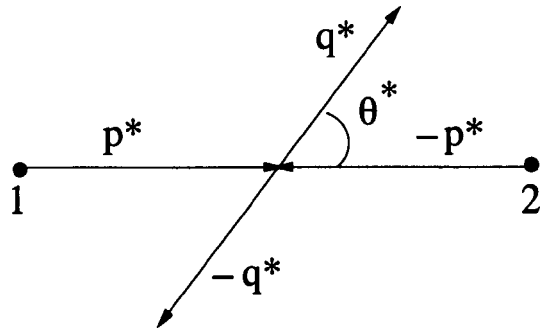


Fig. 2.2: Nuclear recoil scattering in the centre of mass frame.

of mass frame, the target nucleus and incident particle approach each other with equal but opposite momenta. Due to conservation of momentum, they depart after the collision with equal and opposite momenta. These quantities are represented by p^*, $-p^*$ and q^*, $-q^*$ for the initial and final momenta for the incident particle and target nucleus respectively. Following the kinematic argument it is possible to find the following relations:

$$\begin{aligned} p_1 &= \frac{M_{dm}}{M_T} p^* + p^* \\ q_2 &= 2p^* \sin 0.5\theta^* \end{aligned} \tag{2.2}$$

where M_{dm} and M_T are the incident particle mass and target nucleus mass respectively. It follows from Equ 2.2 the target nucleus recoil energy is given by:

$$E_r = E_i \frac{4M_T M_{dm}}{(M_T + M_{dm})^2} \frac{1 - \cos\theta^*}{2} \tag{2.3}$$

where θ^* is the scattering angle in the centre of mass frame and E_i, the initial incident particle energy, is $E_i = 0.5 M_{dm} v^2$, where v is the incident particle

velocity. For a target atom mass of M_T and a dark matter particle of mass M_{dm}, the maximum value for the recoil energy of the target atom, E_{max}, is given by:

$$E_{max} = E_i r \tag{2.4}$$

$r = \frac{4M_T M_{dm}}{(M_T+M_{dm})}$. Ideally, to maximise energy transfer in the collision, the mass of the target should be equal to that of the dark matter particle. Recent SUSY theories favour an LSP mass of between 20 - 200 GeV/c^2. From LEP a lower limit is quoted as 46 GeV/c^2 [39]. Therefore, for detection, a target should be chosen which is suitable for this range.

The equations presented so far are valid for any nuclear elastic recoil interaction. The dark matter specifics are introduced by considering the variables more closely. The number density and velocity of the incident dark matter particle need to be considered in the context of galactic and solar motions. Cross sections must be derived from the SUSY theories.

2.2.2 Neutralino Number Density and Scattering Cross Section

In the simplest model, the dark matter halo is assumed to be at rest with respect to the Galaxy. As our solar system orbits the galactic centre (220 kms^{-1}), this induces a particle flux in the direction opposite to this motion. Assuming that the Galactic system is virialised, then the velocity of the neutralino particles can be described by the Maxwell-Boltzmann distribution. Ignoring the velocity of the Earth about the sun, we have for the velocity distribution

$$\frac{dn}{dv} = \frac{4n_0 v^2}{\mathrm{v}_0^3\sqrt{\pi}} e^{-\frac{v^2}{\mathrm{v}_0^2}} \tag{2.5}$$

where v_0 is the halo velocity dispersion (213kmsec^{-1}) [40]. Equation 2.1 now becomes:

$$dN_0 = \frac{dn}{dv}\sigma_s \mathrm{v}\frac{1000L}{A}dv. \tag{2.6}$$

It can be shown that the scattering is isotropic in the centre of mass frame [38]. This enables definition of the differential number of recoil scatters per unit recoil energy, $\frac{dN}{dE_r}$ as:

$$\frac{dN}{dE_r} = \frac{N_0}{E_i r} \tag{2.7}$$

substituting 2.6 into 2.7 and integrating gives:

$$\frac{dN}{dE_r} = \frac{N_0}{E_i r} e^{-\frac{E_r}{E_0 r}} \tag{2.8}$$

E_0 is the characteristic energy for a virialised WIMP population, $E_0{=}1/2 M_{dm} v_0^2$.

The expression in Equ 2.1 also requires the inclusion of the local number density of neutralino particles, n_{lsp}. Whereas the simple Newtonian analysis of galactic rotation curves suggest a density profile $\rho_{dm} \sim R^{-2}$, where R is radial distance from the galactic centre, this must be modified at low R to account for the significant contribution of ordinary matter to the galactic orbital velocities. The dark matter profile is usually modified to:

$$\rho_{dm} = \rho_0 \frac{a^2}{a^2 + R^2} \tag{2.9}$$

ρ_0 and a are the halo core density and radius. Calculations using this isothermal spherical model give a dark matter volume density of between 0.2 - 0.4 $\mathrm{GeVc^{-2}cm^{-3}}$, a value of $0.3\mathrm{GeVc^{-2}cm^{-3}}$ is often taken [41]. The number density is then ρ_{dm}/M_{dm}, which for a neutralino mass of $100\mathrm{GeVc^{-2}}$ gives 0.003 $\mathrm{cm^{-3}}$.

The final unknown in Equ 2.1 is now the cross section for the dark matter particle with the target nucleus, σ_s. Behind this term lies the physics of supersymmetry. Supersymmetry (SUSY) is a particle physics theory, as yet undetected in nature. SUSY provides a mathematical framework in which fermionic and bosonic eigenstates can be related through a set of commutating and anti-commutating relations. This relation of the different fields results in a deluge of fundamental particles. These are the 'carriers' in the SUSY theory,

in the same way that photons are the carriers of the electromagnetic force. The cross sections for neutralino scattering are usually taken from the Minimal Supersymmetric Standard Model (MSSM). MSSM is the supersymmetric extension to the Standard Model that requires the smallest increase in particle content. The favoured dark matter candidate is the lightest neutralino, which is a superposition of the SUSY partners of the electroweak gauge bosons and Higgs particles, the gauginos and higgsinos. The neutralino states can be written as:

$$\chi^0 = N_{i1}\tilde{B} + N_{i1}\tilde{W}_3 + N_{i3}\tilde{H}_1^0 + N_{i4}\tilde{H}_2^0 \tag{2.10}$$

where the N's are the mixing coefficients set such that the neutralino mass is non-zero. $\tilde{B}$, $\tilde{W}_3$, $\tilde{H}_1^0$, $\tilde{H}_2^0$ are the superpartners bino, wino, and the two neutral higgsinos [42]. The neutralino, because of this mixing, can have different interactions with matter, dependent upon the relative values of the mixing coefficients. The three processes that can lead to neutralino-nucleon scattering are Higgs exchange (spin-independent), Z boson exchange (spin dependent) and squark exchange (spin-independent and spin-dependent). The coupling between a neutralino and ordinary matter is complex. In dark matter research it is usual to refer to two types of cross section, the spin dependent and spin independent. The former is the case where the neutralino couples to the nuclear spin of the target nucleus. Net nuclear spin only arises for nuclei that contain an unpaired nucleon, i.e. for atoms with odd atomic number (A). For the spin independent case, the neutralino scatters off the nucleus in a coherent manner. The cross section for this process is then dependent on the size of the nucleus and it can be shown that the cross section $\propto A^2$. The duality in the neutralino-nucleon coupling, between χ^0 coupling with nuclei with spin (axial coupling) or all nucleons (scalar coupling), leads to a similar duality in the cross sections. Theoretical predictions of the spin-independent cross section of neutralino-nucleon scattering can be seen in Fig 2.3. This plot was produced using the software freely available at [43]. In the given figure, we see the extent of the cross section parameter space.

Neutralino Dark Matter Detection

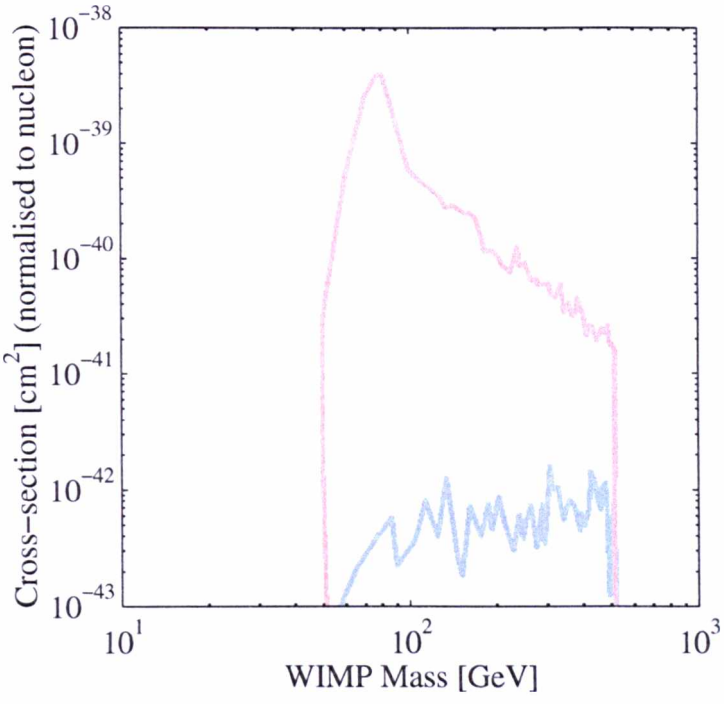


Fig. 2.3: Total spin-independent and spin dependent cross section plots for neutralino-nucleon scattering for WIMP masses between 10 - 1000 GeVc^{-2}. The upper pink curve is the upper bound on the spin dependent cross section. The lower blue curve is the upper limit on the spin independent cross section.

For a more comprehensive coverage of the calculations and theory the reader is directed to the works, [42, 44, 45] *(and references therein).*

2.2.3 Expected Event Rates and Energy Spectra

From the previous section, values were obtained for $n_{lsp} \sim 0.003\text{cm}^{-3}$ and the SUSY cross sections, Fig 2.3. To calculate an expected event rate let us take a SUSY WIMP mass of 100GeVc^{-2}, particle velocity of 220kms^{-1}, a cross section of interaction of 10^{-42}cm^2 per nucleon, and use xenon as an example target, A=131. To calculate the total cross section we use Eqn 2.11 taken from [38],

$$\sigma_{SI} = \sigma M_{dm} M_T A^2 \tag{2.11}$$

where σ_{SI} is the total spin independent cross section and σ =10^{-42}cm^2 is the cross section per nucleon (taken from Fig 2.3). Now we use this cross section in Eqn 2.1. The resultant expected rate is calculated to be 0.5 counts kg^{-1} day^{-1}.

In this calculation we have ignored the form factor effects on the neutralino-nucleon cross section. This form factor, $F(E_r)$, is due to the structure of the nucleus. The nucleus in this scattering process acts as a matrix of scattering centres, analogous to the scattering centres in classic X-ray diffraction. The form factor therefore represents the wavelike nature of the scattering process and accounts for the loss in coherence in the scattering. The event rate is reduced by the addition of the form factor term. This event rate dictates the fundamental characteristics of a dark matter detector, as we shall explore in the next section.

The expected observational recoil spectrum from neutralino interactions is a modification of Equ 2.8, that accounts for the relative efficiency of detection of nuclear recoil energy relative to that of a gamma ray with equal energy. The term introduced is the quenching factor, q_r. The spectrum is predicted to have the form given in Equ 2.12, taken from [41].

$$\left[\frac{dN}{dE_r}\right]_{obs} = \frac{N_0}{q_r E_0 r} e^{\frac{-E_r}{q_r E_0 r}} F^2(E_r) \tag{2.12}$$

From the form of Equ 2.12 we can see that the predicted spectrum will be a falling exponential. Theoretical predictions suggest the recoil energy to lie predominantly in the 0 - 10 keV region.

2.2.4 Dark Matter Detecting Philosophies

The theoretical predictions mentioned so far highlight the difficulty in detecting neutralino dark matter. The signal event rate (possibly less than 1 event per year) means a detector must be optimised to detect low levels of interaction. The general approach of worldwide experiments (independent of the detector physics) is to adopt the following strategies:

- to reduce the background event rate in the detector:
  - place the experiment deep underground
  - use radio-pure materials for construction
- actively discriminate between elastic recoil scattering and other events
- search for seasonal variations in the event rate due to the rotation of the Earth about the Sun
- deploy the largest possible mass of detecting material.

Let us examine each of the first three points in more detail.

Underground Operation and Material Purity

The need to reduce the flux of photons, neutrons and electrons incident on a dark matter detector, results in experiments being operated at sites with substantial terrestrial shielding. At first it was thought that sufficient shielding could enable experiments to be run at, or near, the Earth's surface. However cosmic ray muons interacting in a typical shielding material produce gamma rays and neutrons. The resulting neutron interaction rate in the detector at the surface has been shown to be $\sim 10^3$ collisions per day [38]. This background would swamp any dark matter signal. As neutrons scatter from the nucleus of atoms, signals arising from neutron interactions in a dark matter detector are virtually indistinguishable from those of a dark matter particle. The only possibility for discrimination in this case would be to observe multiple scattering events of the neutron in the detector. The muon induced background rate can be suppressed by placing the experiment underground, where rock acts as a passive shield. Significant reductions in the muon flux, of orders 10^5 - 10^7 lower than the surface flux, can be obtained by operating at depths around 1200m. A quantative representation of this can be seen in Fig 2.4, from [46]. This plot levels at $\approx$ 20km water equivalent, due to the muon flux becoming dominated by the component due to charged current interactions (virtual W-boson exchange with nucleon) of the muon neutrino, ν_μ. This reduction leads

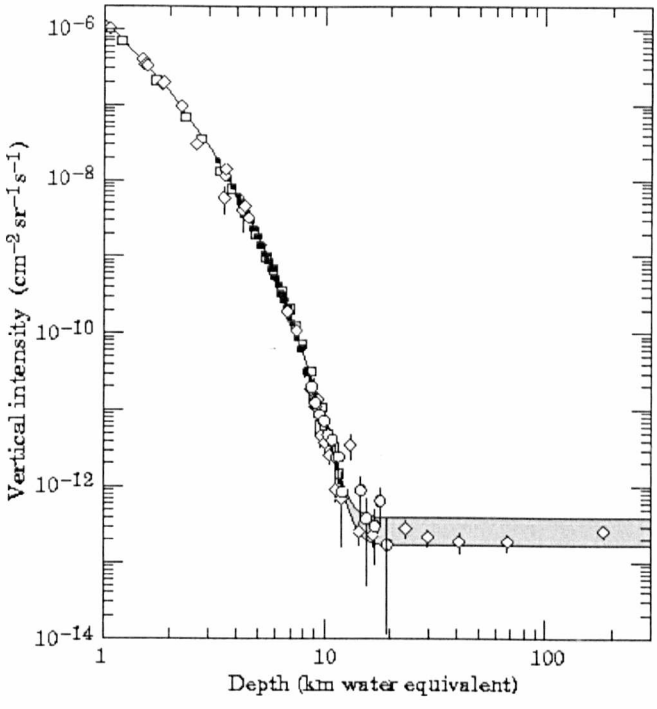


Fig. 2.4: Vertical muon intensity as a function of depth (1km water equivalent $= 10^5 \text{gcm}^{-2}$ of standard rock). The shaded area at large depths represents neutrino induced muons of energy 2 GeV. Experimental data are from [47, 48, 49, 50, 51].

to a muon related event rate of less than 0.1 $\text{day}^{-1}\text{kg}^{-1}$ [38]. The remaining sources of background are then within the site of the experiment, e.g the walls of the experimental hall. The experimental apparatus itself is the final source of unwanted radiation. To remove the latent environmental contribution to the background, experiments are encased in high purity shielding materials. High purity copper and aged lead are two commonly used materials. The ^{210}Pb natural isotope of lead decays over a lifetime of 21 years, releasing an α-particle (3.72MeV) and β-particle (61keV). To avoid these contaminants, sources of old lead (40 years or more) are used to produce a more radio-pure background shield. The United Kingdom Dark Matter Collaboration (UKDMC) has also incorporated the use of a large purified water tank as a system for background reduction. The thickness of absorber required is much greater in the case of

ultra pure water, due to its low density in comparison to copper. However water's neutron thermalisation efficiency makes it a favourable choice as a shield (neutrons are thermalised within $\sim$ 1 metre). Materials that comprise the detector itself must adhere to similar, if not more stringent, conditions than the passive shield. Let us concentrate, momentarily, on the structural components rather than the active detecting material. Copper's high thermal conductivity and mechanical properties make it a perfect choice for detector construction. Electroformation of copper reduces the ^{60}Co contamination, which is usually present in cast copper (from cosmogenic activation), and so is the preferred material option. Stainless steel is also an often used construction material. Precaution should be taken in the selection of stainless steel. It is apparent that American manufacturers used ^{60}Co behind the lining in the furnace. This is used to indicate when the lining is worn through (by a rise in activity of the steel). Such a scheme introduces high levels of ^{60}Co to the steel produced. There is also concern over the recycling of steel from radioactive environments. These factors can lead to different steels having significantly diverse radioactive contamination. The final elements of concern for the background are the electronics and, for the case of scintillation detection, the photo-detecting devices. In these cases, the ceramics in electronic insulation and the glass of the photodetector (specifically photomultiplier bodies) are the sources of contamination. The UKDMC uses a combination of mass spectrometry and counting rates from a Ge detector, located underground, to assess the radioactive purity of many materials used in dark matter experiments. Principally the abundance of uranium, thorium and potassium are a specific measure of a sample's radiopurity as they constitute the main 'natural' sources of radioactivity in a material. Assuming the U and Th decay chains are in equilibrium, the expected count rates per kg of naturally occuring material are: U $\sim 1.7 \times 10^8$ Bq, Th $\sim 4.0 \times 10^7$ Bq, K $\sim 2.8 \times 10^4$ Bq, [38]. Therefore, bearing in mind the neutralino interaction rate, to reduce the background count rate to acceptable

levels would require materials with purities of U, Th < 0.1ppb * and K < 1 ppm †. In reality the achievement of such low levels of contamination for all detector components is very difficult. The limits of a dark matter detector are in essence dictated by the background levels of radiation. The GENIUS collaboration uses this principle as its driving philosophy, proposing to immerse a highly radio-pure detector setup into a large volume of highly pure cryogenic liquid (argon, xenon or nitrogen). However other collaborations place equal emphasis on the ability to identify and discriminate electron recoil and nuclear recoil events. We shall now turn our attention to this philosophy of detection.

Electron Recoil and Nuclear Recoil Discrimination

Discrimination between events in a dark matter detector is possible in several ways, dependent upon the target material. The ability to discriminate is derived from the alternate channels of interaction of the incident particle with the target. Several techniques have been researched in separate dark matter detectors, as shown in Table 2.1. A summary of the techniques follows:

Experimental Group	Target Material	Dicrimination Technique
UKDMC	Sodium Iodide	Pulse Shape Analysis
UKDMC	Xenon	Drift Length
UKDMC/UCLA	Xenon	Ionisation/Scintillation Yield
CDMS	Ge/Si	Phonon/Ionisation Yield

Table 2.1: Table showing the discrimination techniques used in dark matter detectors.

- Electron recoils and nuclear recoils in sodium iodide result in scintillation with differing time profiles. This effect was used widely for several years for discrimination between neutrons and electrons at high energies. The scintillation mechanism is such that nuclear recoils give a shorter decay time constant than electron recoils. At lower energies the difference in time constant is reduced and the variation in the time constant for

*ppb = 1 part per billion by weight, ie a conc. of 1×10^{-9}
*ppm = 1 part per million by weight, ie a conc. of 1×10^{-6}

a similar interaction is increased due to poorer statistics. However it has been shown by the UKDMC that if large data sets are collected then statistical analysis of the pulse shapes can be used to discriminate between nuclear recoil and electron recoil events [52]. In the analysis, pulse shapes are fitted using a single exponential with characteristic time constant, τ. Table 2.2 shows the average difference in time constant between gamma-ray and neutron events, $\Delta\tau_{\gamma n}$, from calibration runs. Using this knowledge of the characteristics of pulse shapes it is possible

Energy/keV	$\Delta\tau_{\gamma n}$
4-5	13
5-7	18
7-10	25
10-13	33
13-16	38
16-19	42
19-22	47
22-25	51

Table 2.2: Mean time constant differences between gamma-rays and neutrons for thallium doped sodium iodide (NaI(Tl)) crystal, as measured by the UKDMC [52].

to reduce the background contamination in the data set. This technique has also been applied to liquid xenon scintillation, see Chapter 3.

- Negative ion drift time projection chambers (NITPC) have been proposed as potential dark matter detectors [55, 56]. These detectors use the drift of negative ion carriers in a host target gas to discriminate between nuclear recoil ionisation and electron recoil ionisation. The ionisation tracks for 40keV recoils, 5keV alpha particles and 13keV electrons have been modelled in argon gas (as an illustration of the technique) to be 2.7mm, 17mm and 85mm respectively by [55]. Discrimination between particles for a given interaction is therefore achieved by the measurement of the track length and charge deposition. Work is underway by the DRIFT collaboration to adapt this technique to the constraints of a

dark matter detector. Argon has a naturally occuring radioactive isotope (^{42}Ar), has a low atomic mass number, and the main isotopes have zero spin making Argon an unsuitable dark matter target. DRIFT therefore is examining the use of carbon sulphide (CS_2) doped xenon. CS_2 is used for its electronegative properties. It acts as the electron carrier from the ionistation site to the avalanche grid and reduces (because of its large molecular mass) diffusion of the track, enhancing the spatial resolution of the detector. As well as discrimination by track length and charge, the DRIFT collaboration also suggest that it might be possible to identify the direction of the track. As we alluded to earlier, the Earth's motion through a virialised WIMP distribution would result in seasonal and daily variations in the count rate in detectors. In a functioning NITPC detector, variations in the direction of tracks would be expected due to these motions. It is the variation in the direction of these tracks that gives the DRIFT experiment a unique channel of data in terms of measuring a dark matter flux.

- The third discrimination technique is to measure the relative scintillation to ionisation yield from an event. Let us restrict our discussion to xenon detectors. The ionisation from a recoiling nucleus after a WIMP/neutron scatter is expected to be lower than that of an electron recoil. Therefore simultaneous measurement of light and charge from an event will give an extremely powerful tool for event discrimination. A two phase xenon system can be designed to collect both primary scintillation from an event in the liquid, then, after charge from the event is drifted from the liquid to the gas, electroluminescence (light originating from electron induced excitation in the gas). The amount of the electroluminescence in the gas is dependent upon the charge produced by the event, and hence discrimination between progenitor particles is possible. An in-depth discussion of xenon as a two phase detector can be seen in Chapter 4.

- Interactions in semiconductor devices also show a variation in ionisation yield per unit energy deposited for nuclear recoils and electron recoils. A semiconducting crystal coupled to a thermistor capable of μK accuracy to detect phonons, and surface mounted electrodes to detect drifted charge, enables measurement of the thermal energy/ionisation ratio. Results from small scale detectors of this type have been reported by several groups supporting this technique, [57, 58].

Annual Modulation

From Equ 2.12 we note that the differential event rate recoil spectrum is proportional to the expected WIMP velocity in the lab frame. However the velocity distribution in Equ 2.5 should be modified to account for the Earth's velocity about the sun ($\sim$ 30 km sec^{-1}), see Fig 2.5. The modified velocity distribution, where v_e is the Earth's velocity about the sun in the galactic frame, is given by Equ 2.13.

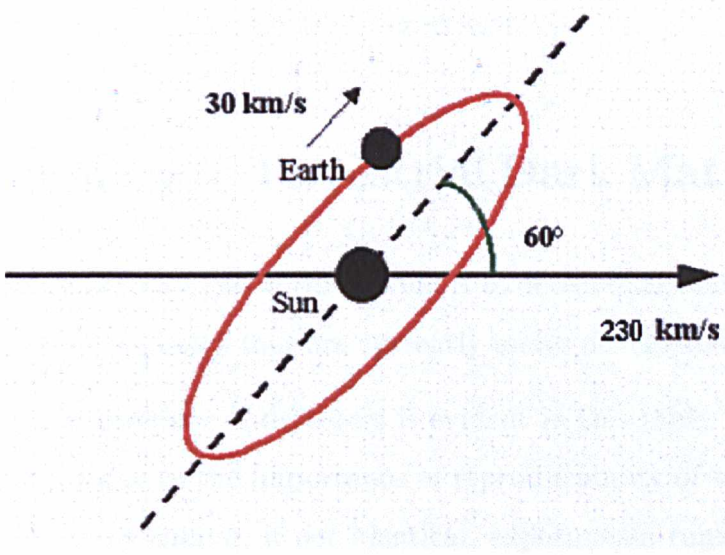


Fig. 2.5: A depiction of the Earth's motion about the sun, relative to the galactic plane.

$$\frac{dn}{dv} = \frac{4n_0 \mathrm{v}^2}{\mathrm{v}_0^3\sqrt{\pi}} e^{-\frac{\mathrm{v}^2+\mathrm{v}_e^2}{\mathrm{V}_0^2}} \tag{2.13}$$

The expression for the expected observational recoil spectrum is now:

$$\left[\frac{dN}{dE_r}\right]_{obs} = \frac{N_0}{q_r E_0 r}\frac{\sqrt{\pi}}{4y}\left[erf(x+y) - erf(x-y)\right]F^2(E_r) \qquad (2.14)$$

where $x = (E_r/E_0 r)^{0.5}$, y=$\mathrm{v}_e/\mathrm{v}_0$ and $erf(s)$ is the error function:

$$erf(s) = \frac{2}{\sqrt{\pi}}\int_0^s e^{-t^2}dt. \qquad (2.15)$$

The rate dependence on $\mathbf{v}_e$, characterised by the ratio between the expected rate inclusive of the Earth's velocity to the expected rate for a stationary Earth (with respect to the sun) has been predicted to vary by 6 % from minimum to maximum [52]. The form of the modulation, as expected due to the Earth's elliptical orbit, is a cosine fluctuation with maxima occuring on the 152.5-th day of the year (equating to June 1st/2nd). This modulation should be detectable at low energies, and would provide a positive identification of dark matter. However this modulation is not incontrovertible. Sources of variable background would have to be ruled out before the detected signal could be claimed as arising from dark matter interactions.

2.3 Summary of Terrestrial Dark Matter Searches

In this section we examine the worldwide effort to detect dark matter. Table 2.3 is a compilation of detectors that are currently under development or running.

The plethora and diversity of detectors is evident in this table. The use of so many detectors is due to the importance of reproducability of results. Ideally one would like to see similar, if not identical, experiments running in several different underground laboratories to reduce unknown systematics due to the environment. This is somewhat true of the sodium iodide detectors, though different groups employ different strategies for data collection and detector construction. The variability of detectors makes direct comparison between them a difficult problem in itself. The most commonly used mechanism for comparisons is the exclusion plot.

Experiment	Site	Target Material
USC-PNL-Zaragoza	Homestake	Ge
Neuchatel-Caltech-PSI	St.Gotthard	Ge
UCSB-UCB-LBL	-	Si,Ge
HDMS (Heidelberg-Moscow)	Gran Sasso	Ge
GENIUS (Heidelberg)	-	Ge
TANDAR-USC-PNL-Zaragoza	Sierre Grande	Ge
GEDEON (MOZA collabortation)	Canfranc	Ge
UKDMC(IC-Sheffield-RAL)	Boulby	Na, I
NAIAD (UKDMC)	Boulby	Na, I
DAMA (Rome)	Gran Sasso	Na, I
ELEGANTS	Kamioka	Na, I
SACLAY	Frejus	Na, I
USC-PNL-Zaragoza	Canfranc	Na, I
ANAIS (Zaragoza)	Canfranc	Na, I
DAMA (Rome)	Gran Sasso	Ca, F
ELEGANTS VI (Osaka, Otho)	Oto-Cosmo	Ca, F
CASPAR (Sheffield)	Boulby	Ca, F (C,H)
DAMA (Rome)	Gran Sasso	Xe
ZEPLIN I (UKDMC)	Boulby	Xe
ZEPLIN II (UK-UCLA-ITEP-Torino-Padova)	Boulby	Xe
ZEPLIN III (UK-ITEP-Columbia-UCLA-Torino-Padova)	Boulby	Xe
DRIFT (UK-UCSD-Oxy-Temple)	Boulby	Xe, Ar
SIMPLE (Paris VII -Lisbon)	Paris	freon
PICASSO (Montreal)	Montreal	freon
CRESST-I(MPI-TUM-Oxford)	Gran Sasso	sapphire
CUORCINO (Italy-US collab)	Gran Sasso	TeO_2
CUORE (Italy- US collab)	Gran Sasso	TeO_2
ROSEBUD (IAS-IAP-Zaragoza)	Canfranc	sapphire
PASS (UBC-Bayreuth)	UBC	In/Sn
ORPHEUS (Bern)	Bern	Sn
SALOPARD (Lisbon-Paris-Zaragoza)	Canfranc	Sn
CDMS-I (US colaboration)	Stanford	Ge, Si
CDMS-II(US collaboration)	Soudan	Ge, Si
EDELWIESS-I (French collab)	Frejus	Ge
EDELWEISS-II (French collab)	Frejus	Ge
CRESST-II (MPI-TUM-Oxford)	Gran Sasso	$CaWO_2$

Table 2.3: Table of current dark matter detectors proposed or currently taking data.

2.3.1 Exclusion Plots

Previously we have shown the extended SUSY cross section parameter space in Fig 2.3. To measure the efficacy of a detector, or indeed the results, it is usual to plot contours of sensitivity in the (σ_s, M_{dm}) plane. Following the discussion in [38], if we define the limit of observability $E_{obs} = E_{det}$ where E_{det} is the detector energy threshold, then we can rewrite Equ 2.12:

$$\frac{N_0}{r} = \left[\frac{dN}{dE_r}\right]_{obs} q_r E_0 e^{\frac{E_r}{q_r E_0 r}} F^{-2}(E_r). \tag{2.16}$$

Equ 2.16 allows one to compare the predicted event rates (kg^{-1} day^{-1}) with experimentally determined background limits (events kg^{-1} day^{-1} keV^{-1}). The

rate exclusion plot can be converted to a cross section exclusion plot by multiplying N_0/r by $A/[n_0(2/\pi 0.5)v_0(L.1000)]$. To allow comparison of differing target nuclei, N_0/r can be scaled by the inverse of the square of the target atomic mass $1/A^2$(for the spin independent case). For the spin dependent case, the rate scales as the inverse of $\lambda^2 J(J+1)$, where λ is a constant to be determined and J is the magnitude of the nuclear spin.

Fig 2.6 shows spin independent limits for the DAMA and CDMS experiments.

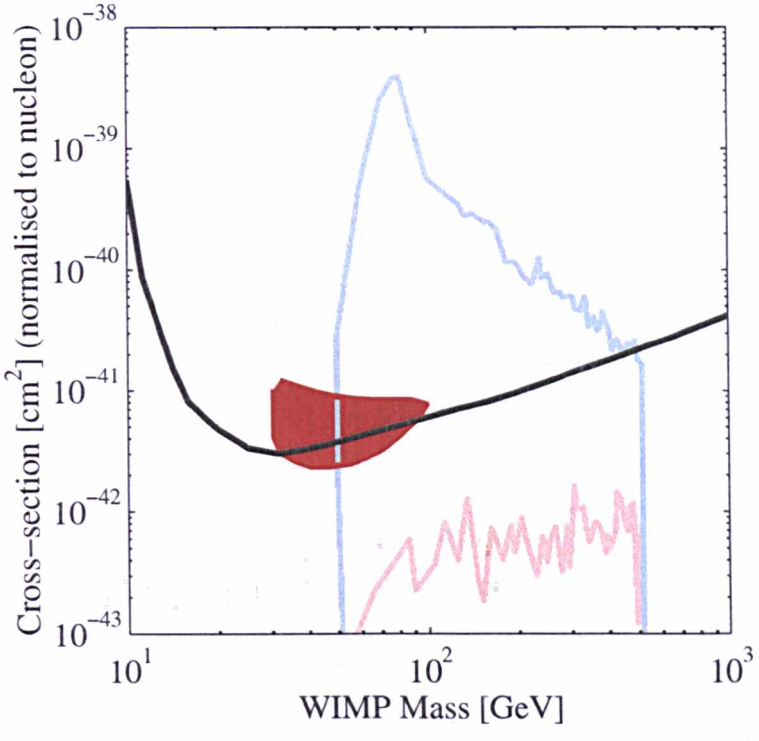


Fig. 2.6: Spin independent cross section limits from the DAMA (Red Area) and CDMS (Black Line) groups. Plot created using software from [43]. References for groups: CDMS [65] and DAMA [66].

The most striking feature in this plot is the red area that corresponds to the result from the DAMA collaboration. The DAMA collaboration has claimed an annual modulation in the signal from a $\sim$ 100kg NaI(Tl) detector array (exposure=$\sim$ 58000 kg days) situated in the Gran Sasso Laboratory, (see Fig 2.7) [60] (*and references therein*). A χ^2 test of its data disfavours the hypothesis of unmodulated behaviour with a probability of 4×10^{-4}. The

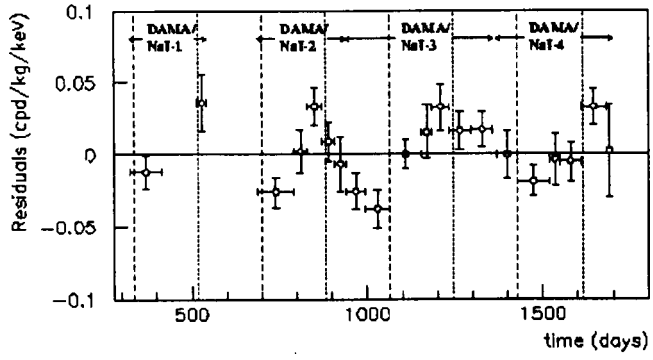


Fig. 2.7: The residual rate in the 2-6keV cumulative energy interval as a function of time (t=0 $\equiv$ 1^{st} January 1998).

phase and time period of the oscillation are reported to be consistent with those expected due to the Earth's rotation about the Sun. The modulation signal is a strong signature for dark matter, therefore the results produce a bound region within the $(M_d m, \sigma_s)$ space. Results from the the CDMS Ge detector set exclusion limits that intercept part of the DAMA region. The CDMS collaboration claims that its results exclude the entire 3σ allowed region from the DAMA experiment with $> 75\%$ confidence [57].

On the Comparison of Dark Matter Detectors

There are intrinsic difficulties in comparing different experimental results from dark matter experiments. As an illustration, let us take the DAMA vs CDMS results. DAMA has seen a variation in the residual rate in the 2-6 keV region, see Fig 2.7 taken from [60]. The CDMS collaboration uses results of actual count rate seen in the Ge and Si detectors. Besides the argument of annual modulation vs count rate as techniques for WIMP detection, one also has to consider the validity of comparing different targets. First of all on the technique, it is clear that the annual modulation is more powerful, but seasonal variations in other systematics must be ruled out for full confidence. Also the CDMS analysis relies on the accuracy of Monte Carlo simulations used to predict the expected neutron background signals in the detectors. Comparing

different targets is a more general issue. In the equations presented so far, we note that there are several target dependent quantities. For example, the form factor and quenching factor are dependent on the target nucleus therefore differing nuclei couple to the WIMP with variable strength.

2.4 Summary

The lightest supersymmetric particle, the neutralino, is detectable by its interaction with ordinary matter. For the best targets the neutralino interaction rate is low < 1 counts kg^{-1} day^{-1}, and the energy deposition is also low $\sim$ a few keV. Therefore all materials used in a dark matter experiment should be chosen with low radioactive contamination. All materials should be sampled and their radiative background measured. Experiments should be conducted in low radioactive backgrounds. Subterranean experimental halls provide low muon flux conditions to prevent neutron/gamma-ray production by muon interactions with matter. A dark matter signal is recognisable by its annual modulation (6 % amplitude fluctuation) due to the Earth's rotation about the Sun. Discrimination between electron recoil and nuclear recoil interactions can be used to lower the background rate in a detector, and increase confidence on any unidentified nuclear recoil signals. There are currently thirty six or more dark matter detectors planned/taking data. The acceptance of a dark matter signal will rely on the systematics and nuclear physics being fully understood for an experiment. Duplication is also a favourable strategy for dark matter detection. Reproduction of similar targets allows more powerful correlation of results, and an exciting prospect is the correlation of the UKDMC NAIAD array that, from Fig 2.6, should register the same annual modulation as the DAMA collaboration report if it is a real dark matter signal. Finally it should be noted that a large proportion of the supersymmetric parameter space remains untouched by current experimental limits. More sensitive detectors are required to explore this parameter space. Chapters 3 and 4 of

this thesis investigate the prospects of dark matter detectors employing liquid xenon technology which are expected to probe more of the unexplored SUSY parameter space.

CHAPTER 3

Liquid Xenon Detectors

3.1 Introduction

This chapter will focus on the application of xenon to direct dark matter searches. The suitability of xenon is examined with reference to the physical properties of the element, scintillation/ionisation yields and radioactivity characteristics. The concept of discrimination using a two phase operation technique will be discussed. Photomultipliers are introduced as light detecting devices and they are discussed with reference to their application to xenon dark matter detectors.

3.2 Xenon as a Target

3.2.1 Physical Properties

In Chapter 2 it was briefly mentioned that mass matching of the target nucleus to expected neutralino mass increased the energy deposition for nuclear recoils, therefore increasing detector sensitivity. To illustrate this, Fig 3.1 shows the variation of the maximum recoil nucleus recoil energy as a function of the target mass, for several WIMP masses (WIMP velocity was taken as 300kms^{-1}).

Xenon Mass

Xenon has a nuclear mass of $\sim$ 130GeV/c^2. Kinematically it is suited to more massive WIMPs. However, as we have seen in Chapter 2, the coherent cross section scales as A^2. Therefore xenon with its high atomic mass has

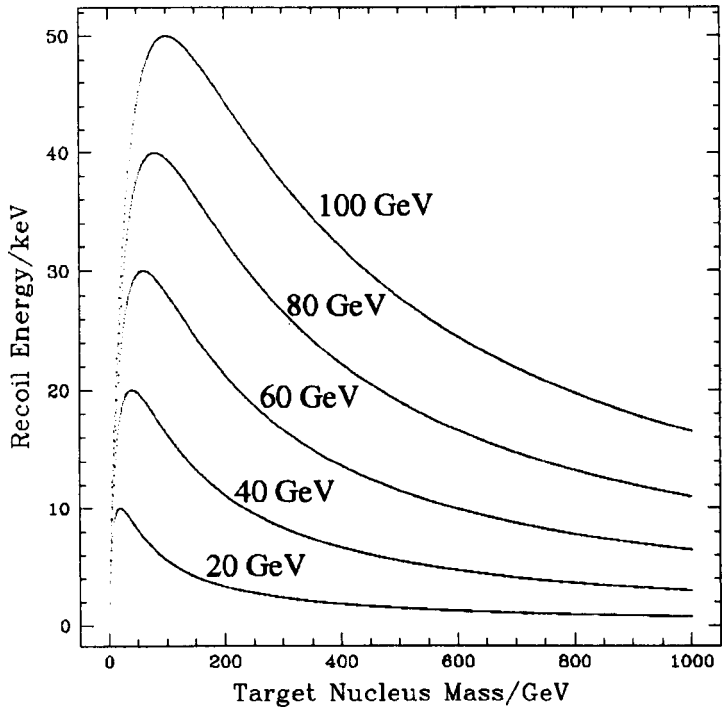


Fig. 3.1: Plot of target nuclear mass vs maximum recoil energy for differing WIMP masses.

an increased cross section compared to lower mass targets. Thus, whilst interactions with low mass WIMPS are not kinematically favoured, the rate of interaction is increased due to the higher target mass.

Xenon obtained from fractional distillation of air is naturally composed of several isotopes. Table 3.1 shows the isotopic abundances of xenon and some other selected physical properties.

From the table we note that xenon occurs naturally with 47.6% odd A isotope. Xenon is therefore sensitive to spin dependent WIMP interactions. Enrichment of the target (by centrifugation) with this odd A isotope would be ideal, but this is expensive.

Liquid xenon targets are also favourable because of the high liquid density. Large mass targets can be achieved within a small volume. For example 1 litre

Physical Properties of Xenon	
Atomic Number	54
Atomic Mass	131.29
Isotopes (% Abundance)	^{129}Xe(26.44);^{131}Xe(21.18);^{132}Xe(26.89)
	^{134}Xe(10.44);^{136}Xe(8.87)
Density of liquid	3.052 gcm^{-3}
Colour of Liquid	clear
Boiling Point (at 1bar)	165.7K
Refractive Index (at 170K)	1.55
Peak Scintillation Line	175 ± 5nm [70]
W-value (eV/ion pair)	15.6±0.3, 14.7 [71, 72]
Attenuation Length	30cm [73]
Fano Factor	0.033±0.045 [70]
Volume Ratio ρ_{gas}/ρ_{liq}	518.9 [70]

Table 3.1: Selected physical properties of xenon, references in square brackets.

of liquid has a mass of 3kg.

Liquid Xenon Purity and Handling

An important consideration for the use of xenon as a target is its purity and handling. Xenon obtained by air distillation is usually free from contaminants at the 5ppm level. Below this, the main contaminants are oxygen, nitrogen, carbon dioxide, water and hydrogen. For a pure scintillation detector, impurity considerations are not as vital as those of the scintillation and charge detector, in which long free electron lifetimes are required. Highly electronegative impurities such as oxygen and water can remove electrons by the following processes:

$$O_2\,(aq) + 2e^-_{(aq)} \longrightarrow 2O^-_{(aq)}$$

$$2H_2O_{(aq)} + 2e^-_{(aq)} \longrightarrow 2OH^-_{(aq)} + H_2\,(aq)$$

where $X_{(aq)}$ indicates species X as an aqueous solution in xenon. To preserve electrons during drift in a two phase chamber, electronegative impurities should be removed below ppb levels. Xenon detectors therefore require purification systems capable of reaching these levels of purity. The detector and gas

handling system should also be free of impurities at these levels. In Chapter 4 we discuss the xenon purification scheme employed at Imperial College and measurements of xenon purity made by the group. Table 3.1 also indicates another practical implication of handling xenon. The high volume ratio implies caution should be taken whilst handling liquid xenon. Large volumes of liquid raised above boiling point represent a serious safety hazard as large pressures can develop in the gas handling system. Therefore it is recommended that, to ensure safety, a dark matter detector should have a clean gas-dump volume in case of uncontrollable temperature fluctuations in the apparatus. Further discussion on gas handling and purification is covered in Chapter 4. Liquid xenon is a cryogenic liquid. Therefore it is necessary to supply sufficient cooling to the detector whilst under operation. Thermal stability is a prerequisite for a two phase experiment. Variation in light output with change in liquid temperature has been seen by this group. We suggest temperature stability to within ± 0.1K.

Xenon and krypton are removed from liquefied air in the same fraction. Further purification of this mixture yields the two pure elements. However there is slight contamination of the xenon by krypton at the 1ppm level. Krypton has a radioactive isotope ^{85}Kr that is a beta-emitter with a half-life of 10.76 years. This isotope is released into the environment by nuclear power stations, and typically has a concentration of 1×10^{-7} ^{85}Kr atoms per Kr atom [74].

3.2.2 Scintillation and Ionisation in Liquid Xenon

The scintillation process in liquid xenon has been widely researched and the reader is directed to [75, 76]. Here we will discuss the main characteristics of scintillation light and the process of electron extraction from xenon.

Fig 3.2 shows a schematic of the scintillation and ionisation mechanism in xenon. Energy imparted to a xenon nucleus can result in ionisation of the atom, leaving a xenon cation and electron, or excitation of the xenon atom.

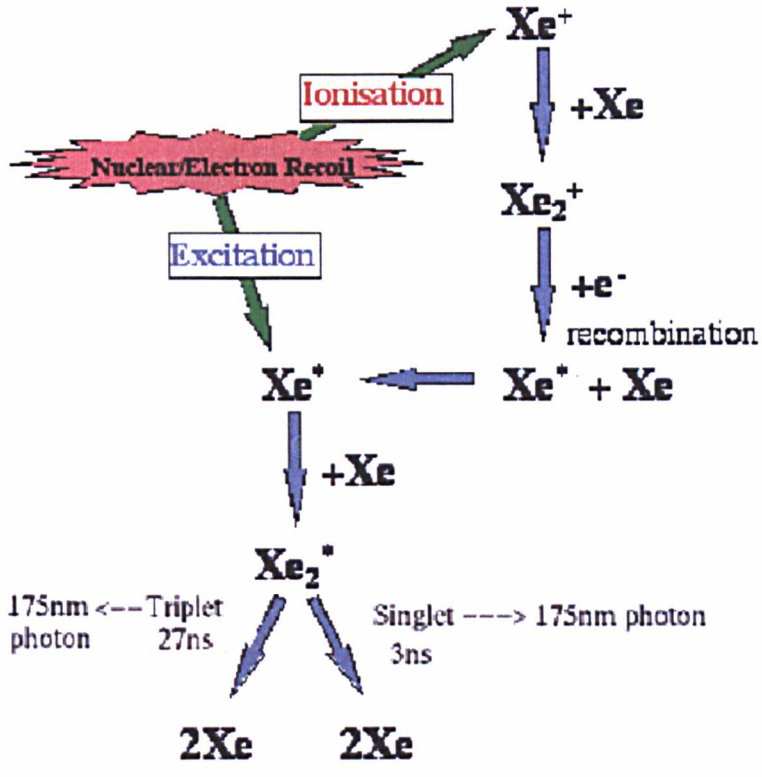


Fig. 3.2: Schematic of xenon scintillation and ionisation mechanism, based on work in [76].

Let us consider these two channels separately. In the ionisation channel, the xenon cations are localised almost immediately - within a picosecond - to form a dimer cation with another xenon atom[77, 78, 79]. A free electron recombines non-radiatively with the dimer cation, forming an excited atom (exciton) Xe* and releasing a neutral ground state atom. This exciton then interacts with a nearby atom to produce the excited molecular state Xe_2^*. The excited dimer (excimer) then dissociates, releasing the characteristic 175nm photons. The second path to scintillation indicated in Fig 3.2 is the direct excitation of xenon atoms to the exciton state. This may occur due to atomic collisions where the energy in the process is too small to effect ionisation. The scintillation light emitted from the excimer originates from the relaxation of the two lowest excited bonding molecular states ($^3\Sigma_u^+$ (triplet) and $^1\Sigma_u^+$

(singlet))to the ground state. These two states have associated lifetimes of 27 $\pm$ 1ns, and 2.2 $\pm$ 0.3ns respectively [76].

The ratio of light produced by direct excitation to ionisation recombination has been shown to depend upon the linear energy transfer (LET), dE/dx, of an interaction. Also the population of the triplet and singlet states has been identified as depending on the LET. Table 3.2 shows experimental figures on the ratio I_s/I_t, the intensity of singlet to triplet states, and the recombination time τ_R for 1MeV electrons and α-particles [102]. High energy electrons have

Measurement	1MeV electron	α-particle
I_s/I_t	0.45$\pm$0.07	0.05
τ_R	45ns	1.5ns

Table 3.2: The ratio of singlet to triplet intensities and recombination times for 1MeV electrons and α-particles

a much lower LET in comparison to α-particles. Therefore the recombination time for electrons is much higher than for the densely ionising α-particle. The implication of this early work was that electron recoil and nuclear recoil scintillation light would have different time profiles. The electron recoil decay time is extended due to the finite time of the recombination process, whereas high density ionising events, such as those reported for the α-particle excitation have a negligible recombination time and therefore the time profile is dictated by the lifetime of the $^1\Sigma_u^+$ and $^3\Sigma_u^+$ states. This relation between LET and scintillation lifetime can be used to discriminate between incident particles. Such discrimination, similar to that in the UKDMC NaI project, is an effective tool for removal of background gamma radiation and therefore reduces detector threshold. In Chapter 4 time constant analysis of gamma-ray (60keV) and α-particle (5.64MeV) scintillation pulses is presented.

Other Properties of Scintillation from Liquid Xenon

The scintillation yield for liquid xenon has been measured by this group and others. Typically the light yield is dependent on the purity of the xenon there-

fore absolute values are somewhat misleading. We present our measurements in Chapter 4. The light yield has previously been measured as 78600 photons/MeV [70]. This value indicates that xenon has a high light output in comparison to other scintillators, such as sodium iodide, where the figure is closer to 40000 photons/MeV. The final intrinsic property of the scintillation light in xenon is the attenuation length. Measurements indicate this is 30 - 100cm, though the values on the upper limit are suspect as it was found that dark surfaces coated with Al_2O_3 in the experiments actually reflected 175nm light to some extent [73, 106]. Throughout the rest of this thesis L_{att}=30cm is assumed.

3.2.3 Two Phase Discrimination Technique

In the previous section we discussed the scintillation mechanisms in liquid xenon. We saw how the nature of the scintillation can be dictated by the linear energy transfer of the interacting particle. The relative density of ionisation from electron recoils and nuclear recoils can be used as a more powerful discrimination technique. By the application of an electric field to the liquid xenon, recombination can be suppressed and electrons drifted freely through the liquid. Ionisation from electron recoil events is more easily removed from an interaction site due to the lower space charge density, which reduces Coulombic interactions between electrons and ions. All electrons drifted and extracted into the gas phase will produce 'electroluminescence', because as soon as the field is high enough for extraction it is automatically high enough for electroluminescence. The relative sizes of the scintillation to electroluminescence signals can be used as a discriminant between background electron recoil events and nuclear recoil (WIMP-like) events. In Chaper 4 we present measurements of the primary scintillation and electroluminescence for α-particles and gamma rays.

The ionisation that is expected to be extracted from a nuclear recoil event is small. For a WIMP event we expect the neutralino to scatter and produce a

recoiling nucleus with an energy of a few - 50keV. Ionisation from xenon atom-atom collisions has not been observed before. However ionisation has been observed in the collisions between other inert gas atoms at energies between 2 - 30 keV [83]. The findings of this work can be summarised as follows. Ionisation of inert gases has been observed between 'like' atoms, e. g. neon-neon (^0Ne-^0Ne where the superscript indicates the ionisation state) and 'like' atoms and ions (e.g ^1Ne-^0Ne). Measurements were also obtained for collisions between different atomic species, including krypton with xenon. The total cross section for the ionisation of xenon gas atoms by neutral krypton, ^0Kr, was measured to be $\sim 2 \times 10^{-16}$ cm^2 (^0Kr kinetic energy 2keV). The cross sections between 'like' species was found to be larger than those for differing species. The findings from the published data also show the total cross section for ionisation is larger for ^0Kr-^0Kr ($\sim 3 \times 10^{-16}$ cm^2) collisions, compared to the ^0Ne-^0Ne ($\sim 2 \times 10^{-16}$ cm^2) interaction. Therefore, based on this data, we can conclude that for the collision ^0Xe-^0Xe, where the incident energy of the xenon atom is 2 - 30 keV, we would expect a total cross section of ionisation to be $\sim 3 \times 10^{-16}$ cm^2. This data is for atomic collisions in inert gases. No data exists for liquid noble gases. The effect of the change of state on this atomic collision ionisation is unknown.

3.2.4 Quenching Factor, q_r

The energy threshold and discrimination factor (for a two phase system) both depend on the efficiency of conversion of the deposited energy from a nuclear recoil into visible energy. The quenching factor, q_r, is defined as the visible deposited energy divided by the true recoil energy. This ratio can be measured by comparing the scintillation yield for known energy depositions by neutrons and gamma-rays. The quenching factor for xenon has been measured to be $0.2 \leq q(_r) \leq 0.6$ [103, 84, 128]. In Chapter 4 the measurements made by the UKDMC are reported. It is worth noting that these measurements will depend on xenon purity which may explain the different results from each group.

3.3 Detecting Scintillation from Xenon

Photons emitted from the relaxation of xenon excited states have a wavelength of 175nm. A photodetector must be used that is suitably optimised for the detection of photons of this wavelength. The device itself must be low in radioactive background and have sufficient sensitive area to ensure good light collection. To enable time constant analysis of pulses, the speed of response of the photodetector must be a few nanoseconds at most. The UKDMC liquid xenon group has decided for the first phase of experiments that the photomultiplier is the best device currently available for this application. At Imperial College, we studied the effects of low temperature operation of photomultipliers with a view to increasing light collection efficiency by immersing the devices in the liquid xenon. In this section we discuss the fundamentals of photomultiplier operation and present the results of the low temperature tests.

3.3.1 Fundamentals of Photomultipliers

The basic structure of a photomultiplier is shown in Fig 3.3 [85]. A photon incident on the photomultiplier window will pass through and hit the photoemissive material deposited on the backside of the quartz. The photoemissive material then releases electrons via photoelectric emission. The emitted electrons are accelerated towards the first dynode, which releases more electrons and so and so forth until the electrons are collected at the anode. The amplification or 'gain' of a photomultiplier is dictated by the potentials placed across the dynodes. This sets the interdynode field strength and hence the electron's kinetic energy. The higher the kinetic energy of an electron incident on a dynode surface, the more secondary electrons are produced. The potential applied across the dynodes is controlled by a network of resistors called a 'dynode chain'. The design of the dynode chain is critical in achieving maximum performance from the photomultiplier.

In general the dynode chain is a set of resistors connected in series, with each

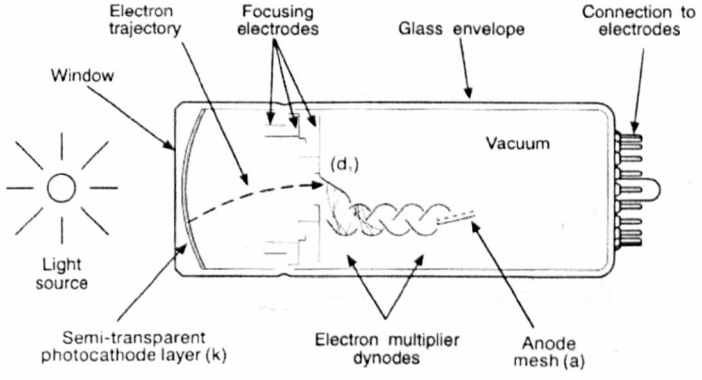


Fig. 3.3: The basic design of a photomultiplier [85].

dynode connected to the nodes between each resistor. High gain tubes utilise 12 dynodes. The resistance placed between the first and second dynodes is approximately double that between the other dynodes. This increases the speed of response of the tube which is paramount if photon timing is going to be used on the scintillation pulses from liquid xenon.

Quantum Efficiency

When discussing photomultipliers one refers to their quantum efficiency, $Q(\lambda)$. $Q(\lambda)$ is defined as the average photoelectric yield per incident photon, and is expressed as a percentage. The quantum efficiency of a photomultiplier tube is one of its fundamental properties and is a direct measure of its efficacy of detection. The quantum efficiency of a photocathode varies as a function of the wavelength of light incident upon it. For xenon scintillation photons of wavelength 175nm, a quartz variant of the bialkali is the best performing photocathode. Photomultipliers for the ZEPLIN III project are being chosen with $Q(\lambda=175\text{nm}) \sim 20\%$. The photoelectric yield, therefore the $Q(\lambda)$, is dependent on wavelength due to two main factors. The first is the transmission of the window of the photomultiplier. To limit the effect of this factor it is necessary to choose a material with high transmission. In general, the transmission of a material is dependent on the wavelength of the travelling light. The highest

transmitting photomultiplier tube windows at 175nm are the spectrosil quartz and magnesium fluoride [85]. These windows have transmissions of $\sim$ 80% at 175nm.

3.3.2 The 9829QA ETL Photomultiplier

The photomultiplier chosen for the ZEPLIN III dark matter experiment is the 9829QA supplied by Electron Tubes Ltd (ETL). This tube was chosen for its fast response, single photon counting, Q(λ) in the VUV, and high gain. Table 3.3 shows some characteristics of this tube.

9829QA Characteristics	
Photocathode Material	Bialkali
Effective Photocathode dia.	46mm
Body Length	126±3mm
Window Radius of Curvature	52mm
Window Material	Quartz
No. of Dynodes	12
Rise Time	2ns
Pulse Width (fwhm)	3ns
Q(λ)	20 ± 2%
Typical Gain	$\sim 10^6$

Table 3.3: Characteristics of 9829QA photomultiplier.

3.3.3 Low Temperature Photomultiplier Operation

The collection and detection of photons limits the energy threshold of detectors. The coupling between the light source and the photodetector in any system is never 100% efficient. For example, it has been usual in the past to have a window as an interface between the photodetector and the liquid xenon. This leads to losses due to absorption in the window material and reflection/refraction at the interfaces between the liquid xenon and window material. By removing the window and immersing the photomultiplier directly into liquid xenon we would:

- remove unwanted light losses due to absorption in the window material
- increase the solid angle onto the face of the photomultiplier
- reduce thermal noise from the photomultiplier.

The thermal noise of the photomultiplier will be reduced because of the low temperature operation of the tube. Thermal noise is created by the unstimulated thermionic emission of electrons from the photocathode or dynodes. Lowering the temperature of the photocathode and other photoemissive surfaces within the tube, lowers the thermal distribution of electrons. Therefore the probability of emission is reduced.

Initially we tested the temperature response of a 9829QA tube in a vacuum cryostat. The photomultiplier was arranged as in Fig 3.4. A copper sheath provided cooling along the length of the photomultiplier whilst the dynode chain remained at $\sim$ 0°C throughout. A yellow pulsed Light Emitting Diode (LED) was included to illuminate the front face of the tube. Several positions were used across the face of the tube with no discernible difference in the results seen. Two thermocouples gave readings of the temperature at the centre (T_1) of the photocathode and at the edge (T_2). Throughout $T_1 \sim T_2$ assuring us that the photocathode was evenly cooled. The entire ensemble was evacuated to a pressure of 3×10^{-6} Torr to avoid condensation on the apparatus and coronal discharge. We performed two measures of the photomultiplier's performance at low temperatures. The first was to check the linearity of response. The light levels emitted by the LED were controlled by applying a pulse from a Hewlett-Packard 8200A Pulse Generator. Assuming a gaussian distribution to the pulse height spectrum recorded for a set voltage on the pulse generator, we calculate the number of photons detected using Equ 3.1.

$$\text{number of photons} = \left[\frac{2.35 \times \text{pulse height centroid}}{\text{FWHM pulse height spectrum}}\right]^2 \qquad (3.1)$$

By plotting the number of photons detected versus the centroid of the gaussian distribution, we can therefore measure the linearity of response for the

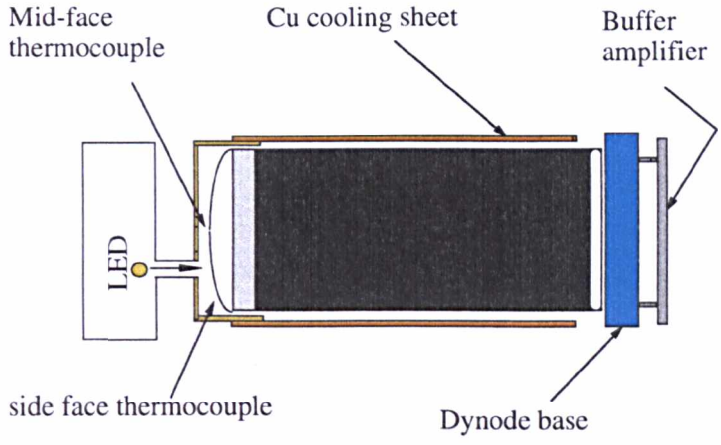


Fig. 3.4: Schematic of experimental set-up used to measure the effects of low temperatures on the performance of the 9829QA photomultiplier.

phototube. Figures 3.5 and 3.6 show the response of the phototube at room temperature (21^{o}C) and -104.5^{o}C. The two plots indicate that the photomultiplier operates linearly at both room temperature and at -104.5^{o}C. The second investigation was into the stability of the photomultiplier response with variable pulse frequency. The voltage applied across the LED remained constant whilst the pulse frequency was increased. Figures 3.7 and 3.8 show the rate dependence of the measured number of photons (again given by Equ 3.1) at room temperature and pressure, and at -104.5^{o}C. Fig 3.8 shows that at low temperatures the response of the tube is very different to that at room temperature. There is a fall in the number of photons detected by the phototube with increasing rate. The *a priori* explanation for this is that the photocathode is becoming positively charged. This would explain the behaviour since positive charging of the photocathode would result in fewer electrons being released per light pulse due to Coulombic attraction. This charging would also alter the electric field distribution between the photocathode and the first dynode which could, in turn, reduce the efficiency of collection of electrons emitted from the photocathode onto the first dynode. The photocathode is

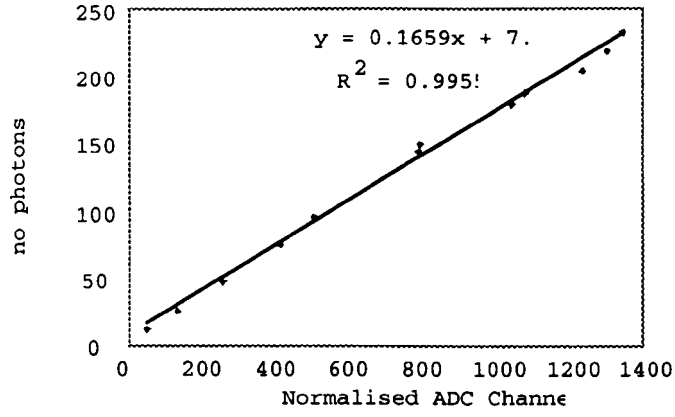


Fig. 3.5: Plot of number of photons detected versus Gaussian distribution centroid for the 9829QA photomultiplier at room temperature and presure.

a semiconductive layer. Therefore with decreasing temperature the resistivity of the photocathode will increase. If the resistivity is such that the number of electrons delivered to the photocathode is less than those emitted due to photoelectric emission then it follows that the photocathode will become charged. Further investigations showed that the fall in response was only significant at pulse frequencies > 2kHz. It is worth noting that this pulse frequency is much greater than that expected in any real dark matter detector. However this measurement has shown that the resistivity of the photocathode is higher at low temperatures. Whilst the rate of a dark matter detector might be sufficiently low to allow safe operation of the photomultiplier at these temperatures, there is a possibility the phototube may become charged due to high light levels. To counter this effect, the photomultiplier tubes for ZEPLIN III are being modified to include aluminium 'fingers' which will aid the removal of charge from the photocathode. Electron Tubes Ltd (ETL) estimate that the addition of the fingers will effectively reduce the Q(λ) of the tube by 5% [86]. This estimate was included in the previous figure for the expected Q(λ=175nm) of the photomultipliers in ZEPLIN III.

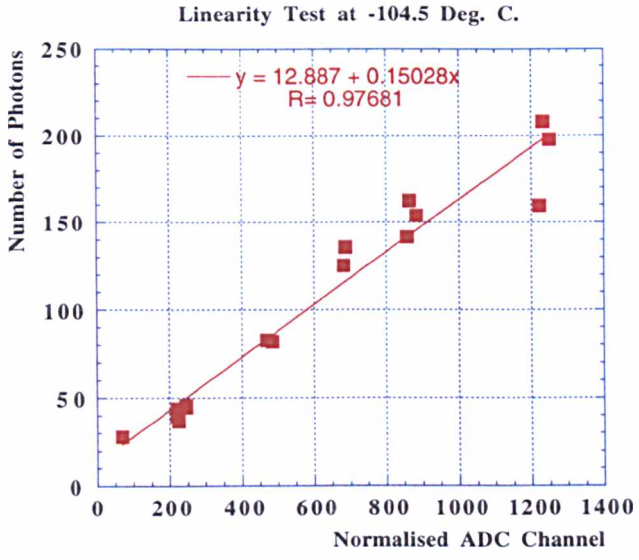


Fig. 3.6: Plot of number of photons detected versus Gaussian distribution centroid for the 9829QA photomultiplier at -104.5°C

Conclusions of Low Temperature Tests

These low temperature tests indicated to us that the operation of the 9829QA ETL photomultiplier device at liquid xenon temperatures ($\sim$ 170K) was feasible. The linearity of the tube was shown to be unaffected at temperatures as low as -104.5°C. A deterioration in the response to high frequency pulsed light was observed. We concluded that the resistivity of the photocathode was increasing. The rate of interaction in an underground experiment will be much lower than the frequencies of pulsed light used in these experiments. However to preserve the response characteristics of the tube, and avoid photocathode saturation, conducting aluminium fingers between the quartz window and photocathode have been implemented, as suggested by ETL [86]. The $Q(\lambda)$ of the tubes is affected by the addition of aluminium fingers, but we expect to achieve $Q(\lambda$=175nm) = 20 $\pm$ 2% for all the photomultipliers in ZEPLIN III.

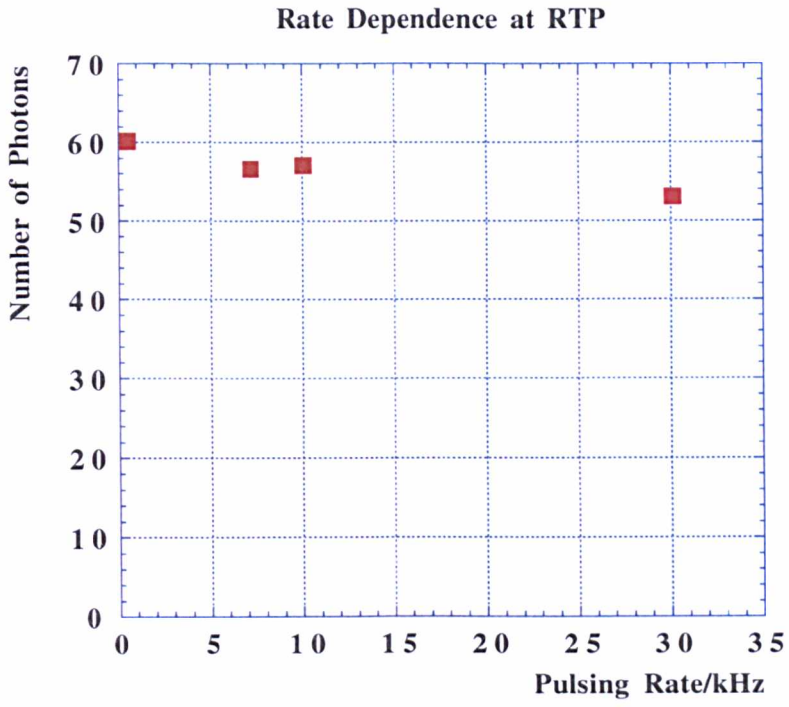


Fig. 3.7: Plot of number of photons detected versus LED pulsing frequency at room temperature and pressure.

3.3.4 Photomultiplier Radioactivity

In the past, dark matter experiments have been wary of the radioactive background produced by photomultiplier tubes. The main contamination arises from ^{40}K, ^{238}U and ^{232}Th in the glass body and from the graded seals used to attach the quartz window to the tube. In the UKDMC-NaI program the photomultipliers were placed apart from the NaI crystal to reduce the incident gamma-ray flux. Light collection was enhanced by the use of light guides. For detectors purely based on the detection of scintillation, this method of background shielding is important. However for two phase systems the philosophy can be altered. It is proposed that in the ZEPLIN III detector the gamma-ray background from the photomultiplier tubes is reduced by: discrimination based on scintillation/ionisation yield, the utilisation of a dead region directly above the phototubes (where ionisation is trapped due to the application of a reverse drift field) and anti-coincidence vetoing. Chapter 6 includes detailed

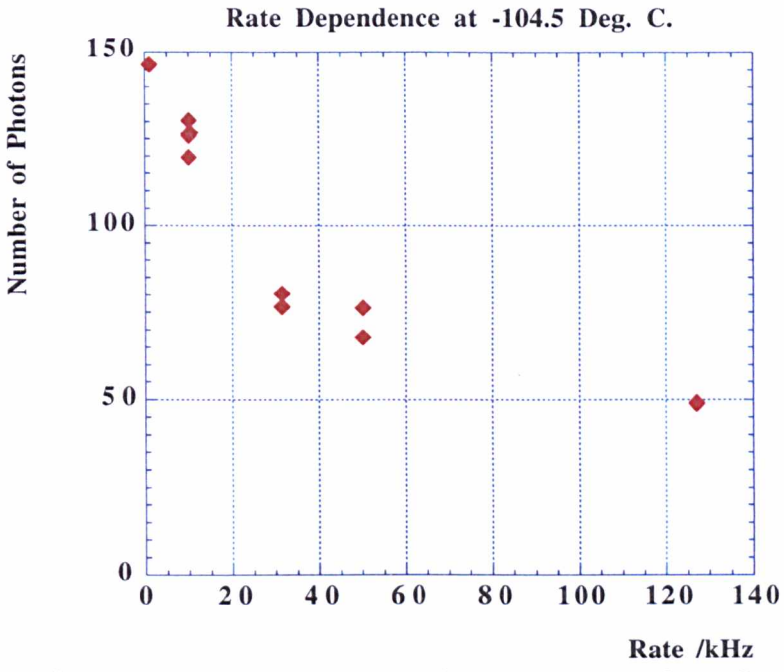


Fig. 3.8: Plot of number of photons detected versus LED pulsing frequency at -104.5°C.

discussion of the gamma-ray background and Monte Carlo results. Chapter 4 discusses the ZEPLIN III detector philosophy in more detail.

3.4 Summary

In this Chapter the main motivations of using xenon as a target were introduced. The two phase discrimination technique and the quenching factor were discussed. Finally results from low temperature photomultiplier tests were presented. These experiments showed that the 9829QA photomultiplier remained linear at low temperatures. Experiments with a pulsed light source indicated that the resistivity of the photocathode was increased at low light levels.

CHAPTER 4

Single Phase Liquid Xenon Detectors

4.1 Introduction

In Chapter 3 two xenon detector philosophies were introduced, the single phase (scintillation) detector and the two phase (scintillation and ionisation) detector. In this chapter we concentrate on the single phase technique. Results from a test chamber operated at Imperial College are reported. We have made measurements of the quenching factor and compared reflectivities of Aluminium (Mylar) and PTFE. The quenching factor was measured at the Neutron Beam Test Facility at Sheffield University. Preliminary results are presented from the ZEPLIN I chamber, constructed at the Rutherford Appleton Laboratory and implemented at the Boulby mine.

4.2 Purification of Xenon

In the operation of the test chamber we devised methods for the purification of xenon that are used later in the operation of our two phase prototype device. The process can be broken into two parts, chemical adsorption of impurities and distillation. To handle the xenon, an ultra high vacuum system was constructed. Let us start by examining this apparatus.

4.2.1 Purification Apparatus

A schematic of the xenon handling system is shown in Fig 4.1.

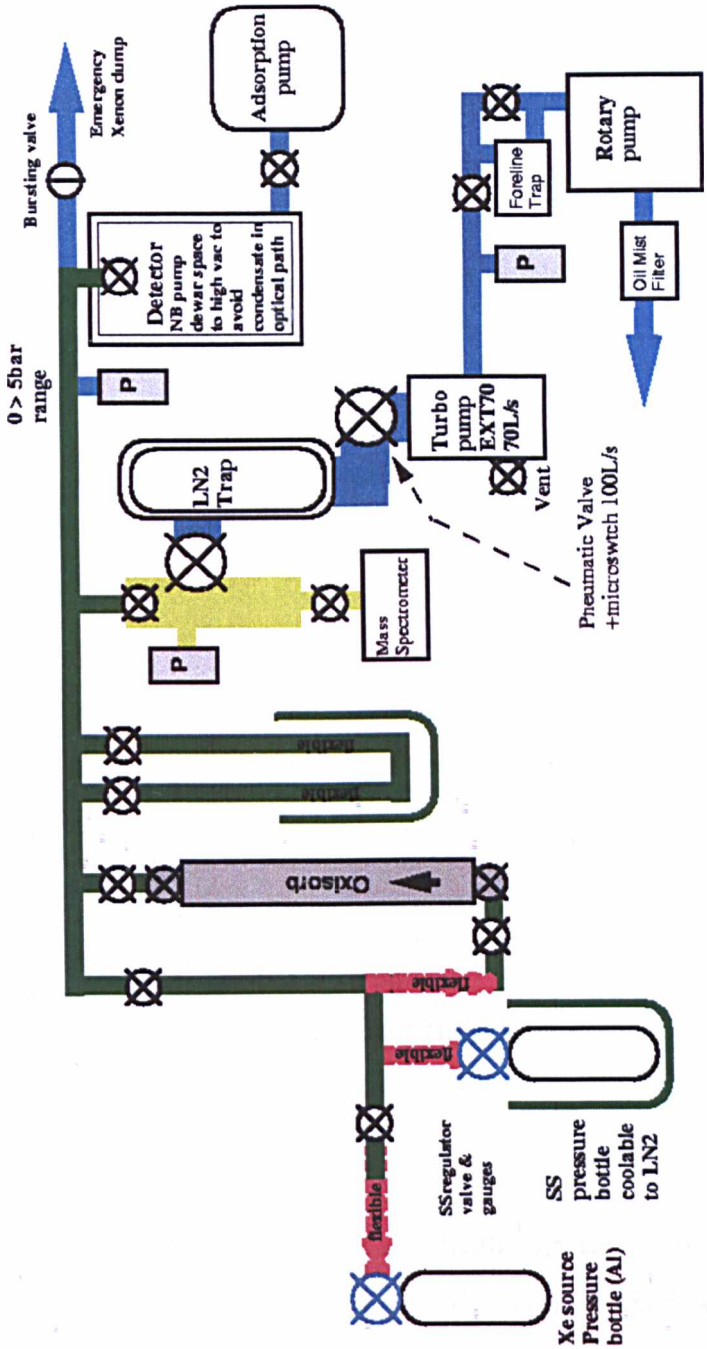


Fig. 4.1: Schematic of the xenon purification scheme [87].

Construction

We refer to the green pipework in the diagram as the gas system (GS) and the light blue pipework as the vacuum system (VS). Before any xenon gas can be admitted from its source bottle into the GS we must first assure the cleanliness of the GS and VS. Each part was cleaned ultrasonically for 15 mins in distilled water, acetone, propan-2-ol and hexane. This series of solvents removes polar and non-polar impurities. Hexane is used as the final stage as it has a low boiling point and therefore evaporates quickly from the surface of the material. The clean parts were then wrapped in aluminium foil in preparation for attachment to the system.

The majority of connections were made utilising Conflat^{TM} stainless steel flanges. These flanges are rated to operate down to pressures of 10^{-11}mb and temperatures of -190°C to +450°C. We used copper annealed gaskets to provide the leak tight connection between flanges. In the instance where National Pipe Thread (NPT) fittings were required we sealed these by coating the thread with pure indium and tightening. The main purification system was mounted on a wheeled aluminium frame. A photograph of the final construction can be seen in Fig 4.2.

Component Description

Let us examine the main components and their uses.

Oxisorb

The Oxisorb cartridge contains a metallic getter, and is used in the purification of the xenon. This cartridge comes filled with argon and before use should be pumped continuously for 3-4 days. Argon remaining after this time can be flushed out using xenon itself, which can then be distilled to remove the argon.

Liquid nitrogen trap

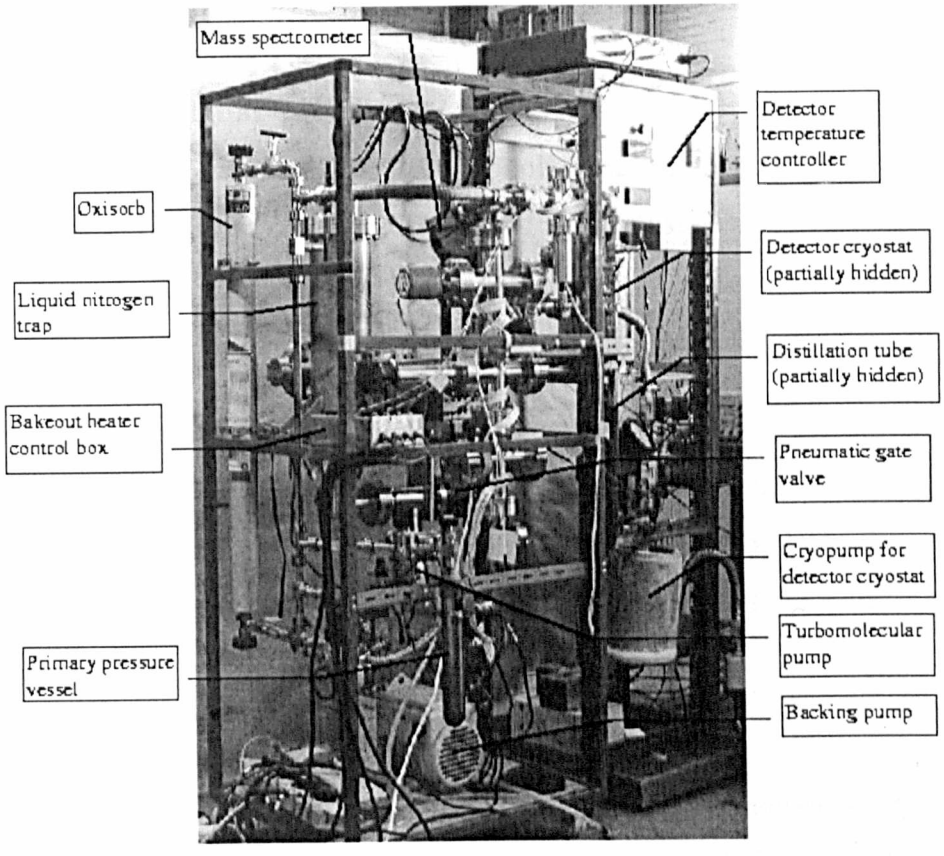


Fig. 4.2: Photograph of the xenon purification system.

The liquid nitrogen trap provides the interface between the GS and the VS. This is a large surface area container that is filled with liquid nitrogen when the system has reached low pressures. The wall between the volume filled with liquid nitrogen and the VS is thin (a few mm). As the internal surface is very cool compared to other surfaces in the system, contaminants are attracted to this surface and condensed/solidified depending upon their boiling/melting points.

Distillation tube

This is a 1m length, 16mm diameter high pressure (100 bar max) tube. During operation with the test chamber, where small volumes of xenon are used, this tube was large enough to be utilised as a volume for dis-

tillation.

Turbomolecular pump

This is an Edwards EXT70 turbomolecular pump capable of pumping down to pressures of $< 1 \times 10^{-8}$mb. The exhaust of this pump is fed into an Edwards rotary pump that expels pumped gas to the atmosphere.

Mass spectrometer

The mass spectrometer can be used to identify atomic and molecular species present in the VS at pressures $< 1 \times 10^{-5}$mb. Partial pressures of atomic species can be measured accurately to levels of $\sim 10^{-12}$Torr.

Detector cryostat

The test chamber and photomultiplier assembly are housed in the detector cryostat. Cooling to the test chamber is supplied via thermal coupling to a liquid nitrogen heat sink. The cryostat is pumped by a cryogenic molecular sieve to reduce both thermal losses from the test chamber, due to convection, and scintillation light attenuation between the window and photomultiplier tube. Several layers of aluminium foil are wrapped Between the outer and inner walls of the cryostat. These insulating layers provide reflective surfaces that reduce the radiation heating from the outer wall.

Valves

The majority of the valves used in the GS are Nupro (product code), with welded Conflat^{TM} flanges. The larger valves used on the VS are Vacuum Generator right angled valves (part no. ZVR40R), rated to operate at pressures $< 1 \times 10^{-9}$mb. One of these connects the VS to the GS directly. Finally there is a pneumatic gate valve connecting the

VS to the turbomolecular pump. This valve is automatically closed in the event of a power failure to maintain system vacuum integrity. The valves provide gateways for the transfer of xenon gas in the GS.

Pressure gauges

The system comprises two forms of gauges. For volumes where high pressure gas is expected, Bourdon gauges with pressure ranges 0-7 bar are used. For low pressure measurements ion gauges are used which are sensitive to pressures from 1×10^{-2}mb down to 1×10^{-8}mb.

4.2.2 Purification Strategy

The purification scheme that will be described here has been used at Imperial College to obtain xenon of sufficient purity to use in both scintillation and scintillation/ionisation detectors. Xenon is supplied with the impurities H_20, O_2, CO_2, N_2, Kr, H_2, at the ppm level. The physical properties of these contaminants dictate the purification procedure. We employ two main concepts of purification - chemical adsorption and distillation. It should be noted that we have purified our xenon supply > 25 times in the past four years. Therefore we suggest that the following strategy should be followed at least 10-15 times before high purity levels are reached.

System Preparation

The GS and VS should be baked for several days (3-4) at temperatures of > 100°C. During this time the liquid nitrogen trap should be filled. The liquid nitrogen trap provides a surface onto which outgassed molecules can preferentially attach. After the bakeout our system pressure reads $< 1 \times 10^{-8}$mb. The remaining contaminants measured by the mass spectrometer are then H_2 and N_2 whose partial pressures are $H_2 \sim 1 \times 10^{-8}$mb and $N_2 \sim 1 \times 10^{-9}$mb. As all other contaminants H_20, O_2, CO_2, and Kr are not measurable by our mass spectrometer, upper limits can be placed on their partial pressures

of $< 1 \times 10^{-12}$mb. Once the system has reached this state, pumping on the GS can be removed and immediately replaced by xenon gas at a pressure of ~ 2 bar*. Filling to this pressure surpresses outgassing of impurities from the walls.

Chemical Adsorption by Oxisorb

The first stage in xenon purification is to utilise the Oxisorb cartridge. The Oxisorb contains chromium embedded on an SiO_2 lattice. The chemical reaction that takes place between the chromium and another species is referred to as a redox reaction. That is to say that reduction and oxidation (hence redox) of differing species is taking place. In general the reduction and oxidation equations are:

$$\begin{aligned} \mathrm{Cr} &\longleftrightarrow \mathrm{Cr}^{6+} + 6e^- \\ X + ne^- &\longleftrightarrow X^{n-} \end{aligned} \tag{4.1}$$

where X is an oxidising species and n is the preferred oxidation state of X. If we take oxygen as an example Equ 4.1 becomes:

$$2\mathrm{Cr} + 3O_2 \longleftrightarrow 2\mathrm{Cr}_2O_3 \tag{4.2}$$

where the charges have been balanced by suitable multiplication. The Oxisorb is therefore capable of removing oxidants from gas passed through it. Strong oxidants, by which we mean species for which the second reaction in Equ 4.1 is thermodynamically favourable, will be removed more efficiently than weak oxidising agents. From our initial list of impurities the most affected by the Oxisorb will be H_20, O_2, CO_2 (in no particular order).

We have used the Oxisorb cartridge in two ways. The first method is to fill the cartridge with the entire xenon supply, and allow the gas to permeate through the SiO_2 lattice. The second method is to create a circulation of the xenon from its initial containment bottle, through the Oxisorb and then finally into

*All figures given in bar are absolute pressures.

a clean receptacle volume. This second approach can be used in conjunction with the distillation process. We have no data to suggest that either of these methods is superior. For the scenario where xenon is retained in the Oxisorb cartridge it was noted that the gas was more difficult to recover. Increased ingression of xenon atoms into the SiO_2 lattice is the most likely explanation for this.

After the Oxisorb has been exposed to impurities, it should be recycled. For the first 30 - 40 uses this can be achieved by simple pumping. After this we suggest baking of the cartridge to drive off impurties. Essentially by baking, the equilibrium of Equ 4.2 is shifted to the left as the reverse reaction is endothermic and, as an equilibrium, LeChatelier's principle '*that a system in equilibrium will react so as to counter any change in its environment*' is obeyed.

Distillation

After xenon has been exposed to the Oxisorb it should be collected in a clean vessel that has been baked and pumped. The xenon is removed from the Oxisorb by placing the receptacle vessel in liquid nitrogen. This vessel now acts as a cryogenic pump, and xenon is solidified in the vessel. We have used two different types of distillation. The first case is not distillation in the conventional sense, i.e. the controlled boiling of a mixture to produce pure distillate. In this first instance we transfer small portions of the xenon to the distillation tube. The distillation tube is immersed in liquid nitrogen, the level of which is slowly increased during the addition of the xenon. This process creates a layer of solid xenon on the walls of the tube, see Fig 4.3. Whilst maintaining the solid xenon at the temperature of liquid nitrogen, the two inlet valves at the top of the distillation tube are opened. This volume is then pumped by the turbomolecular pump. At this temperature, contaminants with boiling points < 77 K can be removed. Fig 4.4 shows a mass spectrum time sequence taken whilst the solid xenon was being pumped. This time profile is quite short as exposure of the mass spectrometer to high pressures increases degradation of the instrument. From this short sequence one can identify the

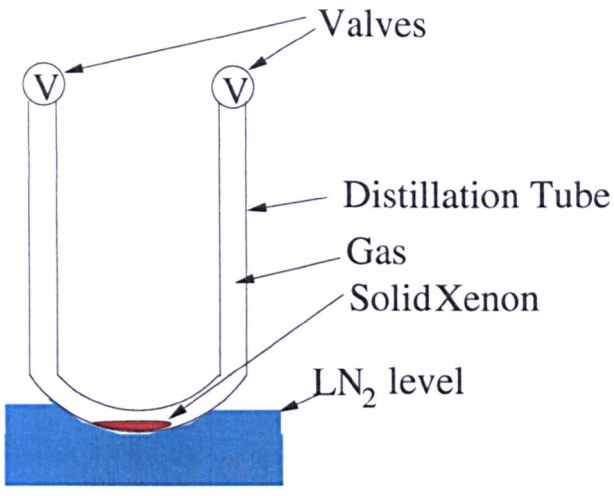


Fig. 4.3: Sketch showing the distillation tube set up. The two inlet valves are opened alternately to balance the build up of solid xenon on either side.

main species being actively removed. They are argon and nitrogen. The argon remains as contamination from the Oxisorb. The nitrogen is present due to system contamination. When examining these spectra it should be noted that the pumping rate of species is convolved into these measurements, therefore relative species pressures are not the true concentration ratios. Note the low levels of carbon dioxide, water and oxygen.

Coincident with the physical removal of contaminants by pumping, there is a more subtle purification taking place. The metal surface itself acts as a trap for atoms and molecules. Fig 4.5 shows a sketch of the process. Two types of molecular/atomic adsorption can occur. They are chemical and physical. The latter of these 'physisorption' is a Van der Waal's interaction between the metal surface and a polarisable atom or molecule, and subsequent accomodation in the metal surface. This type of bond is weak in comparison to 'chemisorption' where chemical bonds are formed between the metal and interacting species (usually covalent). By reducing the temperature of the metal surface we encourage adsorption onto the metal. The rates of these processes vary for different species. In the case of physisorption, rates of accomodation will be higher for more polarisable species where Van der Waal attraction is stronger.

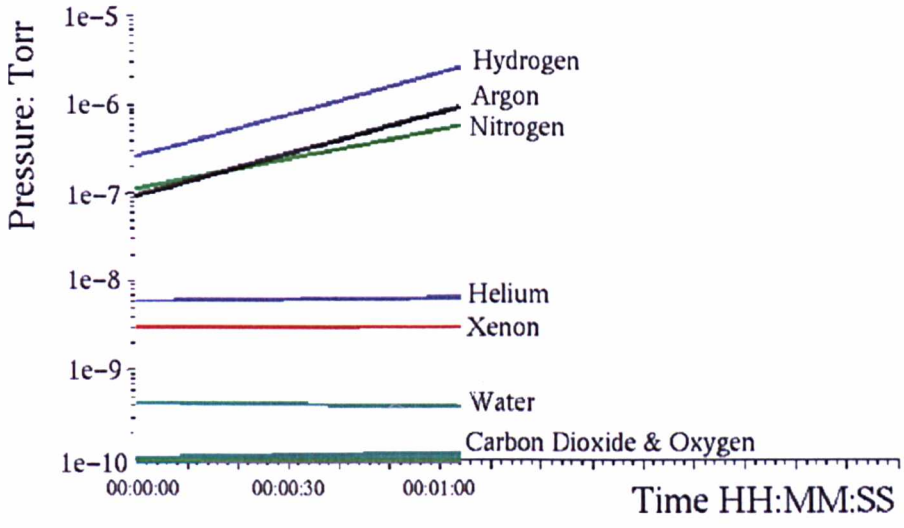


Fig. 4.4: Time profile of mass spectrum of purification system whilst solid xenon is being pumped.

For chemisorption, the higher the bond enthalpy between the metal and the chemiadsorped species, the more readily this process will proceed. Whilst we expect xenon to become physisorped due to its polarisability, chemisorption of xenon should be low. Conversely impurities such as H_20, O_2, CO_2, N_2 and H_2 are readily chemisorped onto the surface of the metal. Therefore, as the overall adsorption rate of xenon is lower compared to the impurities, purification takes place. Evidence for this occurring is shown in the mass spectrum time sequence in Fig 4.6. This chart shows the chemical composition of the system before and during heating of the distillation tube after the solid xenon has been pumped.

This rather extended time sequence shows the effect of heating the distillation tube after solid xenon has been in contact with the walls. The sudden increase in partial pressures of many species indicates the time at which heat was applied to the distillation tube. Comparing the concentrations to those taken whilst pumping on the xenon (Fig 4.4), the increase in oxygen, water, hydrogen and carbon dioxide can clearly be seen. These are all species that we would

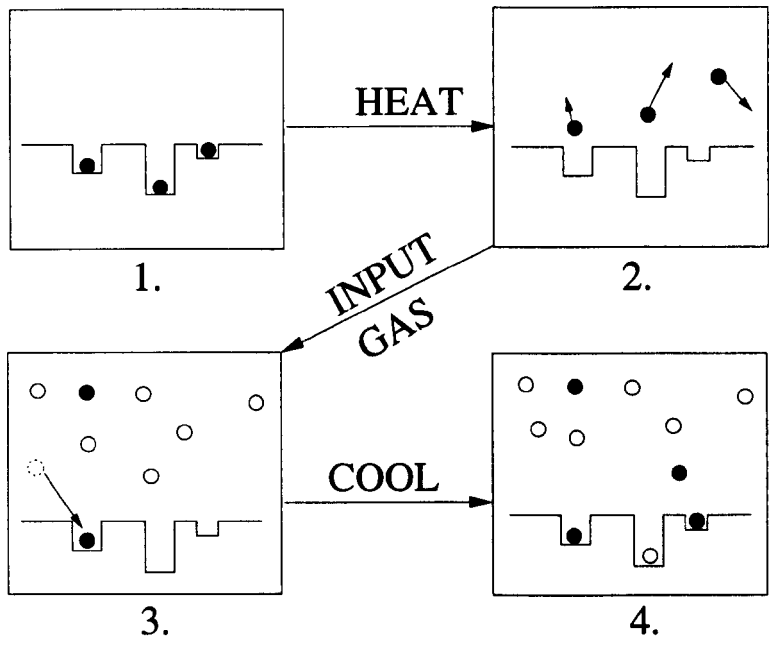


Fig. 4.5: Sketch showing the process of adsorption onto a metal surface. 1) The metal surface at room temperature with adsorption sites filled. 2) Heat releases adsorbed atoms and molecules which can be pumped (this occurs during baking). 3) A gas mixture surrounds the metal surface and adsorption sites become filled. 4) Cooling reduces atomic and molecular kinetic energies increasing adsorption.

expect to be chemisorped onto the surface of the metal. The mass spectra support this.

To achieve further purification of xenon, we use a conventional method of distillation. For this process we require two thermally controlled vessels. The source vessel contains the xenon to be distilled. The destination vessel we choose to be the detector volume itself. A schematic of the process can be seen in Fig 4.7. As can be seen from this representation, we immerse the source cylinder in cool ethanol. With sufficient care the ethanol bath can be maintained at a temperature of 178 $\pm$ 5 K by a combination of cooling with liquid nitrogen and manual stirring. The bath usually takes the form of a mixture of both solid and liquid ethanol[†]. At this temperature the pressure

[†]Some ethanol solidifies when contacted by the liquid nitrogen (T_{mp} = 155.8K for ethanol).

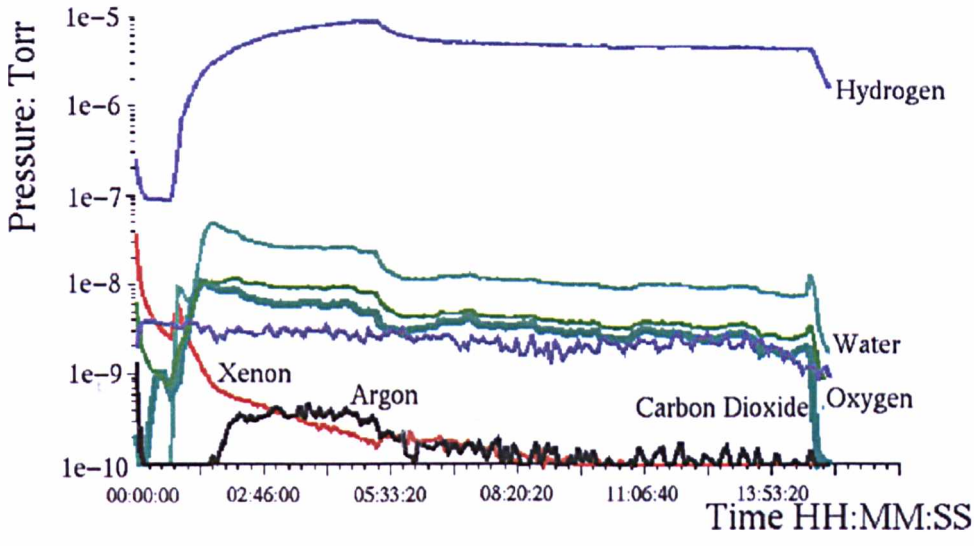


Fig. 4.6: Time profile of mass spectrum for system open to distillation tube at room temperature and high temperature ($\sim$ 473K after time=01:30:00).

on gauge 1 (see Fig 4.7) reads $\sim$ 1.7 bar. We maintain the temperature of the detector volume at approximately 173K, where the pressure reading from gauge 2 is $\sim$ 1.2 bar. With this pressure differential, gas can flow from the source cylinder to the receptacle detector volume. This process is lengthy. To attain $\sim$ 15cm^3 of distillate requires $\sim$ 2 hours.

4.3 Test Chamber Measurements

At Imperial College we developed a liquid xenon test chamber capable of measuring scintillation. The system comprised a 70cm^3 maximum volume capacity cell, viewed through a quartz window by a 9829QA ETL photomultiplier. With this system we measured scintillation from liquid xenon excited by an internal americium-241 (^{241}Am) source which was mounted on an aluminium float. Comparitive reflectivity measurements of Aluminium(Mylar) and PTFE were made. These suggested PTFE was a more efficient reflector of xenon scintillation light. A measurement of the xenon quenching factor was also made at the Neutron Test Facility at Sheffield University. We measured q_r to be 0.17$\pm$0.03

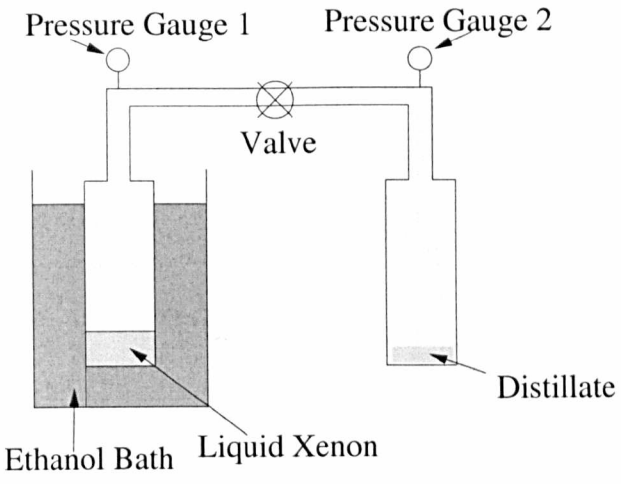


Fig. 4.7: Schematic of the distillation process.

in the recoil range 40 - 70 keV. Measurements of the time constants for α-particle and gamma-ray scintillation signals events were made with τ_α=23ns and τ_γ=43ns.

4.3.1 Test Chamber Desciption

A diagram of the test chamber is shown in Fig 4.8. The system comprises of three main stages, the temperature control system, the test cell and the photomultiplier. Cooling is supplied by a liquid nitrogen heat sink that is thermally connected to the test chamber via a copper plate. This copper plate is attached to the test chamber and a vacuum seal is formed by the compression of indium wire between the two parts. The copper plate also houses a single heater cartridge rated to operate at 120V with a power dissipation of 220W. A Pt100 thermocouple is thermally linked to the copper plate and wired into a temperature control unit (TCU). The TCU controls the state of the heater circuit. A variable resistor is placed in series within this circuit which enables the experimenter to control the power dissipated in the heater cartridge. With this system, temperatures in the test cell could be maintained at a predetermined level with fluctuations of only $\pm$0.1K. The test cell is cylindrical with

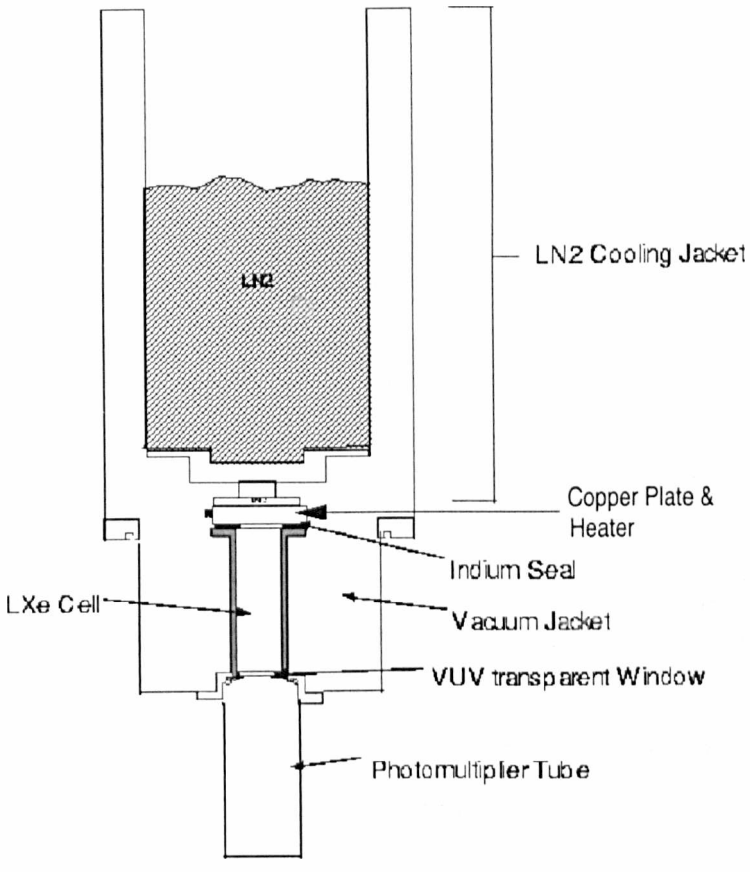


Fig. 4.8: Schematic of test chamber and outer vacuum jacket.

a radius of 15mm and height 100mm. Xenon gas is fed into the cell through a pipe at the top. The cell is viewed by a photomultiplier through a Spectrosil quartz window. Signals from the photomultiplier are read out into a pulse height analyser (PHA) or fast digital oscilloscope (LeCroy 7200) sampling with 1GHz frequency. The temperature of the test cell is monitored by three Pt100 (platinum) thermocouples placed at intervals along its length.

To measure scintillation light from xenon, due to the excitation of α-particles and gamma-rays, we arranged the test cell as in Fig 4.9. An ^{241}Am source is mounted at the centre of a cylindrical block of aluminium (radius 14mm height 15mm). This block is then placed in the test cell with the source facing

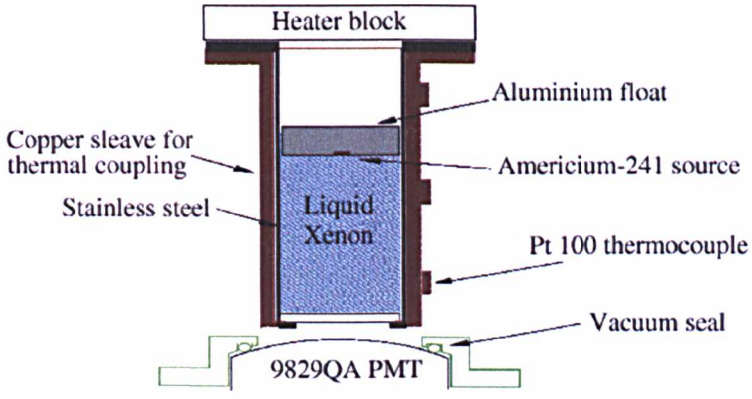


Fig. 4.9: Schematic of the test chamber arrangement.

the photomultiplier. Aluminium has a lower density than that of the liquid xenon[‡]. Therefore as liquid is condensed, the aluminium block floats, and the radiation source is displaced. By comparing the variation of light output as a function of depth, relative measurements of reflective materials can be made (these line the inner surface of the test cylinder).

4.3.2 Reflectivity Measurements

By the addition of known quantities of xenon into the test cell, plots can be made of the photopeak position of the α-particle spectrum versus liquid depth. This response curve can be compared for different materials. An example of the α-particle spectrum is shown in Fig 4.10. The photopeak position is reduced with increasing depth due to the decrease in solid angle of direct light and increased losses to reflections. Therefore comparing these curves yields a qualitative measure of the efficiency of reflection for different materials. From the curves in Fig 4.11 we deduce that PTFE of 4.5mm is the superior reflector of scintillation of xenon light. These results had an impact on the design of the UKDMC ZEPLIN I zero field xenon dark matter detector - a PTFE reflector within the target was incorporated.

[‡] ρ_{Al}=2.70gcm^{-3}

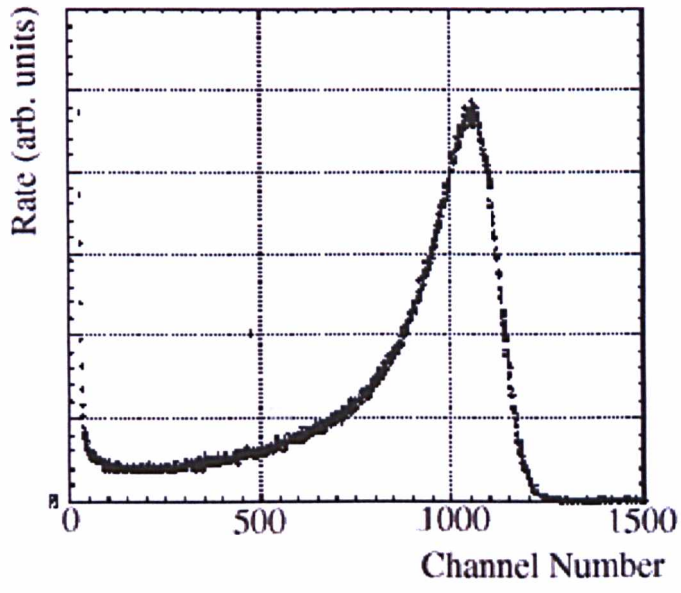


Fig. 4.10: Energy spectrum for 5.49MeV α-particles from internal ^{241}Am source in liquid xenon test chamber.

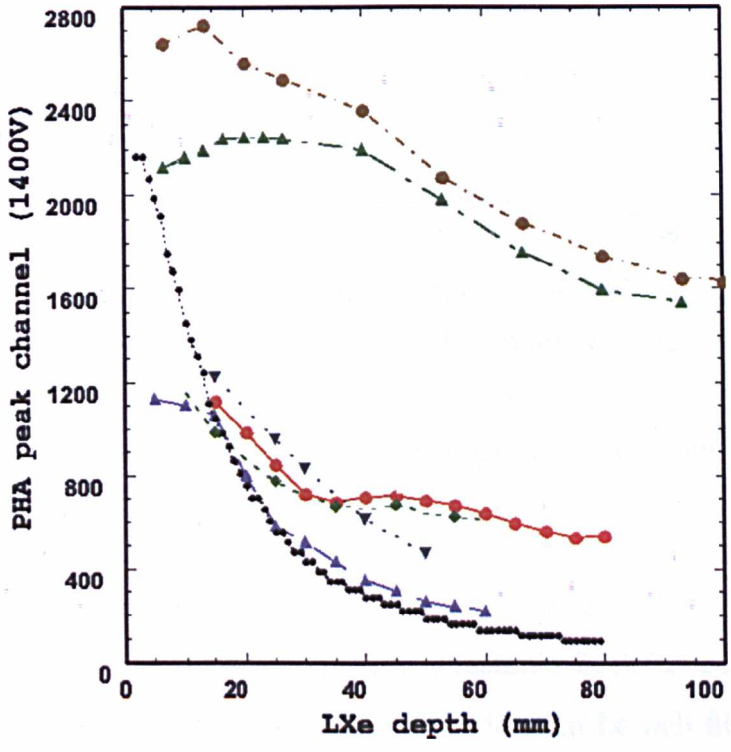


Fig. 4.11: α-particle photopeak position vs depth of liquid xenon. Curves are for: PTFE 4.5mm thick (green - $\triangle$), PTFE 4.5mm thick (khaki - $\circ$), Aluminium/Mylar (red - $\circ$), stainless steel (blue - $\circ$), black wall simulation (black - $\circ$), stainless steel wall (grey - $\triangledown$), PTFE 0.1mm PTFE (green - $\diamond$).

4.3.3 Scintillation Measurements

The spectrum of the low energy gamma-rays from the ^{241}Am was also measured. This is shown in Fig 4.12. The 60 keV gamma-ray photopeak can clearly be resolved as can the single photoelectron peak from the photomultiplier. The feature at around channel 125 is attributed to the Neptunium complex of lines. Pulse shapes were measured for α-particles (5.49MeV) and ^{60}Co gamma-rays (1.17MeV & 1.33MeV). Fig 4.13 shows the average pulse shapes for a thousand events. Events were selected based on the integrated area of the pulses.

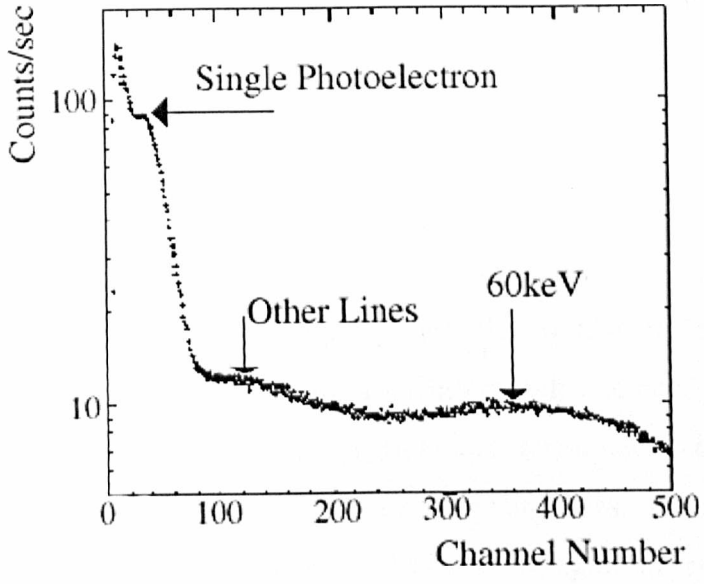


Fig. 4.12: Energy spectrum for low energy gamma-rays from internal ^{241}Am source in liquid xenon test chamber.

Fig 4.13 indicates the difference in time constants between nuclear and electron recoil events. The decay of the scintillation can be well fitted by a single exponential profile. A histogram of the fitted time constants for α-particles and gamma-rays is shown in Fig 4.14. The left (red) distribution is the time constant distribution of the α-particles and has a mean value of 23ns and an

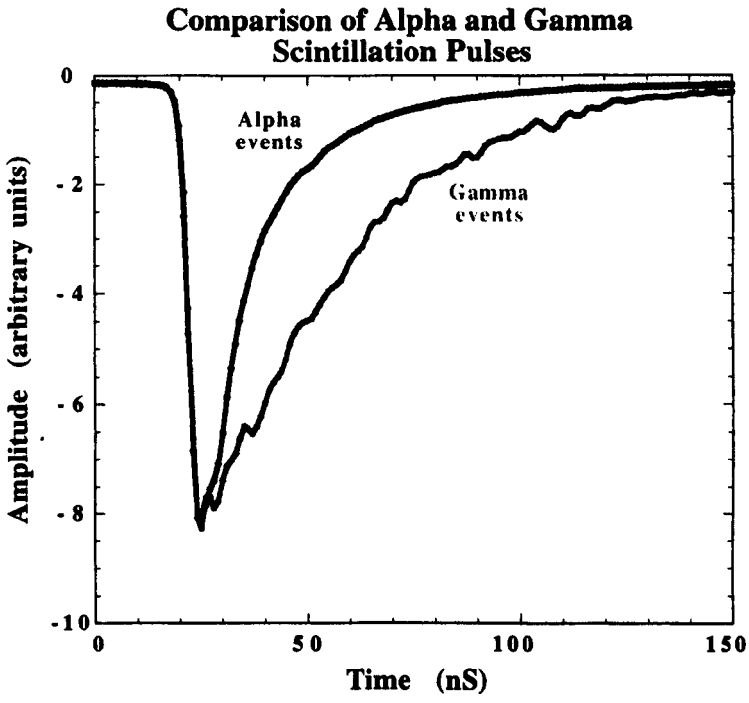


Fig. 4.13: Average pulse shapes of gamma-rays and α-particles in liquid xenon test chamber.

associated width of 3ns. The right (blue) distribution for the gamma-rays shows a mean value of 43ns and an associated width of 8ns. These measurements were taken with high energy particles. At lower energies the gamma-ray distribution is expected to shift to lower time constants. This effect was measured in a seperate detector where, at 13.5keV, the gamma-ray time constant was found to be 29.1 $\pm$0.6ns (the error is the error on the mean value and not the associated width of the distribution) [128].

4.3.4 Measurement of Xenon Quenching Factor

The quenching factor of xenon was measured by irradiation of the test cell with a monoenergetic neutron beam of energy 2.85 MeV. The beam was produced by a ^{2}D - ^{2}D device at the University of Sheffield, producing $\sim 10^9$ neutrons/s isotropically. The isotropic source is collimated by specific shielding of the

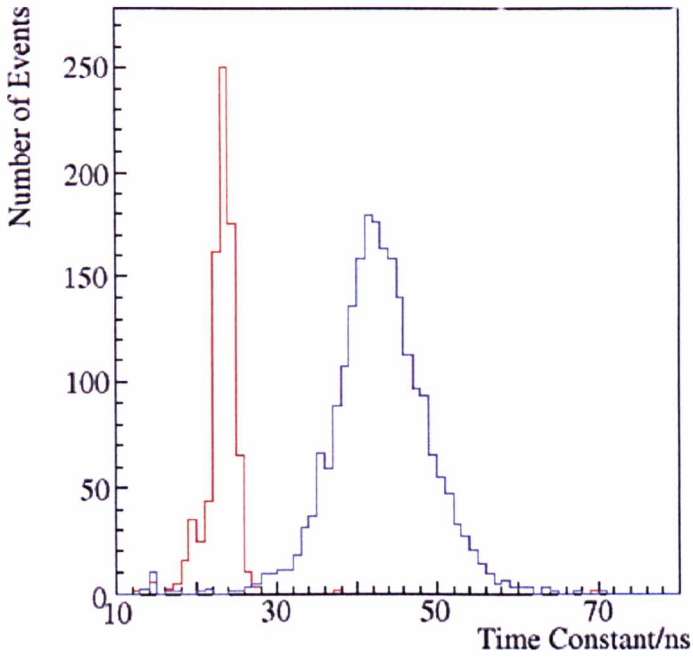


Fig. 4.14: Histogram of the single exponential time constant fits to scintillation pulses from α-particle and gamma-ray excitation in liquid xenon.

source with lead and boron loaded wax. For this test the xenon test chamber was placed 0.2m from the collimator orifice. A pulse shape discriminating Nuclear Enterprises NE213 counter was placed at angles of 120^o, 105^o, and 90^o, see Fig 4.15 for angle definition. The NE213 was placed 1m from the liquid xenon detector. Signals from the xenon target were used to trigger a time-to-amplitude converter (TAC) module. A LINK Systems 5020 pulse-shape discrimination unit identified nuclear recoil events in the NE213 counter. Outputs from this module stopped the TAC module. Signals corresponding to a time of flight of less than 500ns then triggered a fast LeCroy digital oscilloscope. The oscilloscope digitised the signals. The pulse data with the TAC amplitude was then passed to a PC running LabView^{TM} and data was stored for off-line analysis. This technique has been used before to measure relative scintillation efficiencies and pulse shapes in NaI(Tl) and CaF_2(Eu), [89, 90, 91].

For a neutron recoil at angle θ^* (in the center of mass frame) the energy of the recoiling nucleus can be shown to be:

$$E_r = E_i \frac{2m_n m_t}{(m_n + m_t)^2}(1 - \cos(\theta^*)) \tag{4.3}$$

Where E_i is the energy of the incident neutron, m_n is the mass of the neutron and m_t is the mass of the target nucleus. In the case of neutron scattering from a xenon nucleus $m_t >> m_n$, therefore we can assume $\theta^*=\theta$, where θ is the angle measured in the lab frame. Figure 4.15 shows a schematic of the arrangement of the neutron beam test facility, in which the angle θ is shown. From Equ 4.3 the recoil energies expected from the three angles 120^o, 105^o,

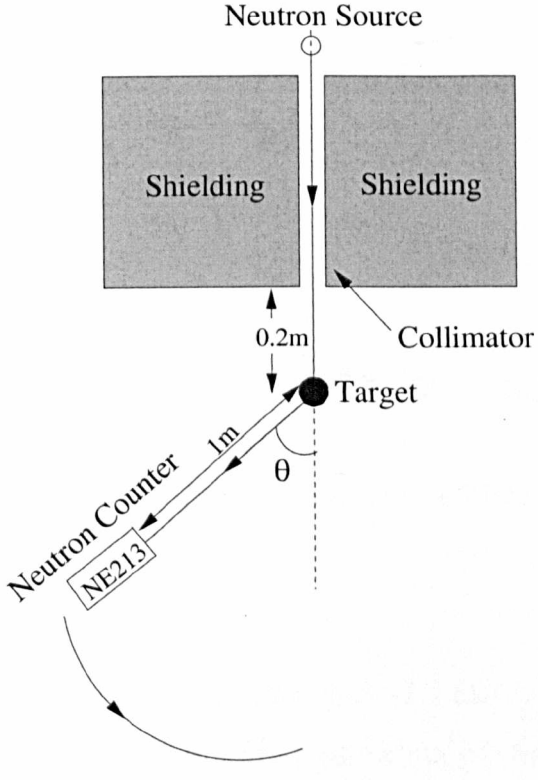


Fig. 4.15: Schematic of the neutron beam apparatus at Sheffield University, indicating the lab frame angle of scatter θ.

and 90^o are 64, 54 and 44keV respectively.

The quenching factor is found by measuring the visible energy recorded from the neutron scatter and dividing this by the recoil energies expected i.e. E_{obs}/E_r.

The test cell is first calibrated with gamma-ray sources of known energy. Fig 4.16 shows the energy spectrum arising from the test cell when irradiated with gamma-rays from a 10μCi ^{57}Co source. Pulse Height (PH) spectra were also obtained in situ during experimentation, utilising PC-based software. Table 4.1 details the calibration results.

Calibration Source	Line Energy/keV	PH Centroid
LED	-	3
^{57}Co	122	254
^{137}Cs	662	1311

Table 4.1: Results from test cell calibration in situ at Sheffield University Neutron Test Facility.

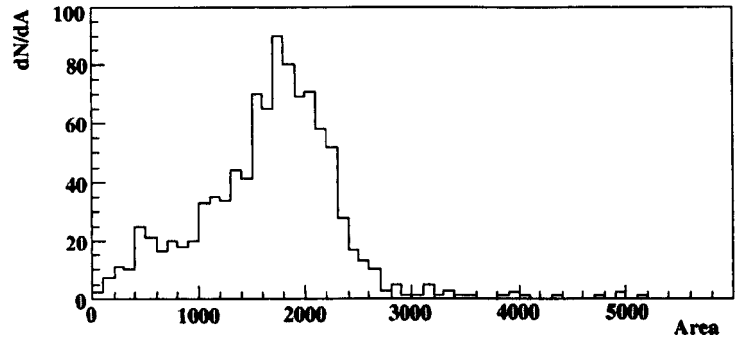


Fig. 4.16: Energy spectrum for liquid xenon test cell irradiated with external ^{57}Co gamma-ray source.

The PH results compute to give a light yield of 1.5keV/photoelectron. Calibration was performed before and after operation of the neutron beam and indicated no deterioration in light yield.

Results from Neutron Beam Scattering

Data analysis was performed by D. R. Tovey of Sheffield University [128]. The mean nuclear recoil energy was determined by fitting a gaussian to the curve of the observed energy spectrum. Events were selected based on two criteria. Firstly the energy deposition was restricted to < 30keV to reduce

contamination of the data with high energy events. Secondly, the pulses were fitted with a single exponential and only events for which the decay time was within the range 12-30ns were considered. This reduces contamination of the data from coincidence gamma-ray electron recoil events. The neutron recoil spectrum with the angle of scatter set at 120° is shown in Fig 4.17. The

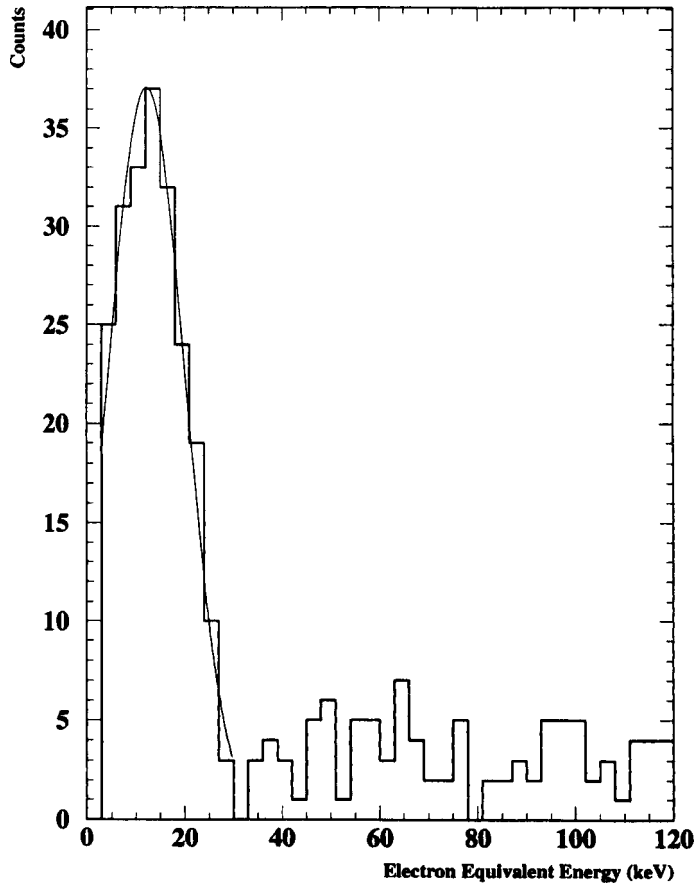


Fig. 4.17: Neutron recoil energy spectrum with gaussian fit.

energy was calibrated according to the results in Table 4.1. This procedure was performed for the two other angles. A plot of the quenching factor as a function of the nuclear recoil energy is shown in Fig 4.18. The results are consistent with a quenching factor for xenon of 0.17±0.03. The errors in the points include both the statistical errors from the fits and systematic effects due

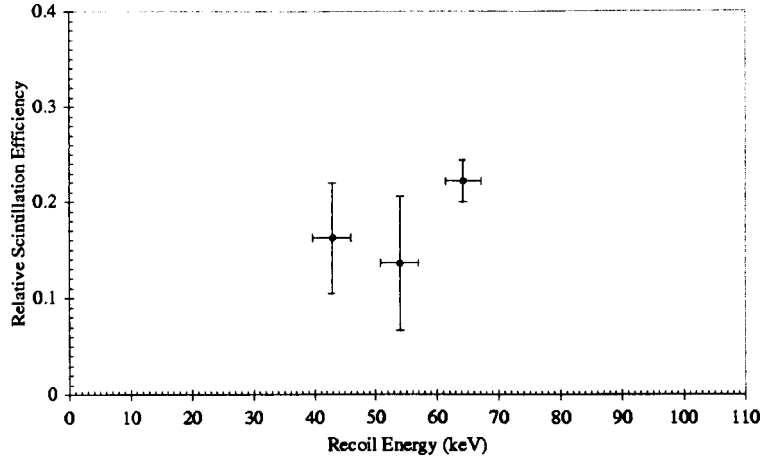


Fig. 4.18: Quenching factor for xenon as a function of nuclear recoil energy.

to the finite solid angle acceptance of the NE213 counters, possible fluctuations in the neutron beam energy and variation in the fitted means. The values for the scattering angles 90^o and 105^o are less certain than the 120^o. At these angles the scintillation distribution of the neutrons is more difficult to identify.

4.3.5 Conclusions from Test Chamber Experiments

A liquid xenon scintillation test chamber has been operated at Imperial College. Light output for the setup shown in Fig 4.9 with an internal PTFE 4.5mm reflector was 1.4 keV/photoelectron. This output was achieved and maintained for a period of 6 weeks without re-purification of the xenon. Comparative reflectivity measurements indicated that a 4.5mm thick PTFE insert produced the highest reflectivity for xenon scintillation light. The pulse shapes of high energy α-particles (5.49MeV) and gamma-rays(1.3MeV) were analysed. The decay times from a single exponential fit indicated $\tau_{\alpha_{5.49MeV}}$=23±3ns and $\tau_{\gamma_{1.3MeV}}$=43±8ns. Further experiments with other gamma-ray sources showed a dependence of τ_γ on deposited energy. Neutron tests at the University of Sheffield confirmed the prospect of pulse shape discrimination between nuclear recoil events and electron recoils. The quenching factor for xenon was also mea-

sured in our detector to be q_r=0.17±0.01. This value is in agreement with that measured by the ICARUS collaboration [84], but well outside the range measured by DAMA [92]. This discrepancy could be caused by differences in the purity of xenon used in each experiment. Electronegative contaminants, such as oxygen, remove electrons from electron recoil events with greater efficiency than from nuclear recoil events, which produce less intrinsic ionisation. Therefore a sample of xenon which contains more electronegative contaminants will be expected to have a measured quenching factor which is larger than for pure xenon.

The purification technique and results achieved influenced the design of the ZEPLIN I single phase dark matter detector.

4.4 ZEPLIN I - Single Phase Xenon Detector

The UKDMC has developed and built a single phase xenon system for dark matter detection. ZEPLIN I is a 4kg fiducial mass liquid xenon target viewed by three 9265QA ETL photomultipliers. To date, the detector has collected 6 weeks of data corresponding to 168 kg days.

Fig 4.19 shows a photograph of the ZEPLIN I inner target vessel. This vessel, when completely constructed, is placed inside a vacuum sealed outer container. In the photograph the main observables are: the target volume, gas inlet pipe, cooling tube and turrets. The target volume takes on a parabolic shape to enhance light collection. Internally, this volume is lined with a custom moulded PFTE shell of thickness 5mm (following the test chamber results). Gas is fed into the volume at the top through a stainless steel flexible pipe. The stainless steel reduces thermal losses from the target. Cooling is accomplished through the conduction of heat through the copper into pipes that carry a constant flow of refrigerant to a Polycold 'PFC Water Cryo Pump' unit that maintains the refrigerant temperature at $\sim$ 156K. The turrets (pictured) act as a passive shield to low energy gamma-rays from the photomultiplier tubes.

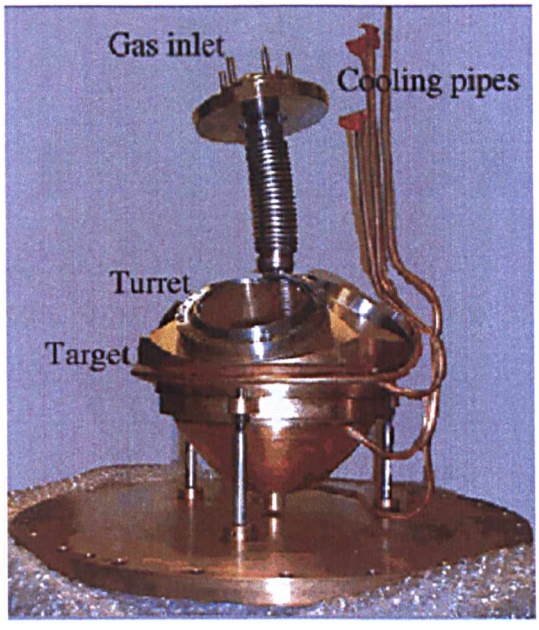


Fig. 4.19: Photograph of the ZEPLIN I inner target vessel.

Higher energy gamma-rays events (Compton scatters) in the target volume are vetoed by means of an external Compton veto system that surrounds the target assembly, shown in Fig 4.20.

As the target volume is viewed by three photomultipliers, rejection cuts are possible based on the relative responses of the tubes. Events that occur preferentially close to an individual tube, due to more efficient light collection, will produce a larger signal in that tube. Therefore cutting events, for which the signal contribution from a single tube is significantly greater than that of the others, removes unwanted background events that are deemed to have occurred from gamma-rays due to radioactivity in that tube.

ZEPLIN I was installed in the Boulby mine towards the end of the year 2000. Six weeks of useful data has been collected so far. This has yet to be fully analysed. Initial analysis suggests that the background rate for energies 1-50keV is about 20 dru*. A complete analysis will include rejection of turret events and time constant analysis. It is projected that this detector will require

*1 dru = 1 count kg^{-1} day^{-1} keV^{-1}

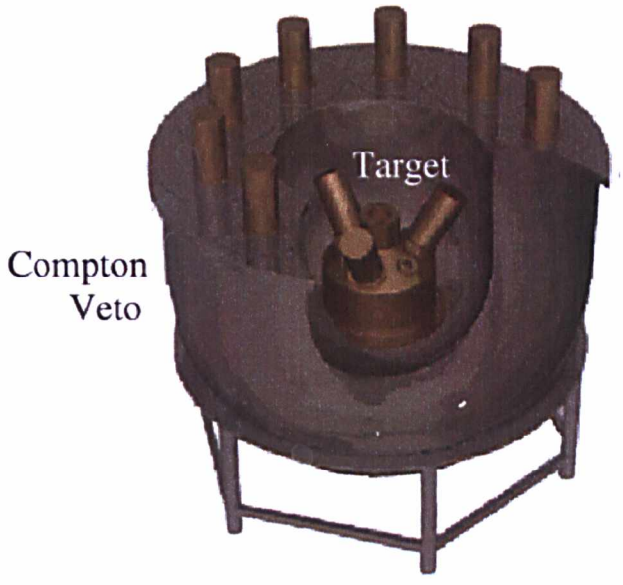


Fig. 4.20: Schematic of the Veto/Target arrangement for ZEPLIN I.

1 year of running (~1500 kg days) to acquire sufficient data to explore the DAMA region of interest in the SUSY parameter space.

4.5 Summary

This chapter has covered the operation of a liquid xenon scintillation chamber. The purification apparatus and strategy used to purify liquid xenon were discussed. Mass spectra of the residual gases in the system indicate that contamination of the electronegative impurities is reduced to below ppb levels. Measurements were presented of the comparative reflectivities of variable thicknesses of PTFE and Aluminium (Mylar). Results suggested that 4.5mm thick PTFE had the highest reflectivity. Time constants of the scintillation light from liquid xenon were reported. The decay time constant for gamma-rays of energy ~1 MeV was measured to be 43 ± 8ns. For α-particles of 5.49MeV the decay time constant was measured to be 23 ± 3ns. The quenching factor for liquid xenon was investigated using the neutron beam at Sheffield University. The data suggest that the quenching factor is 0.17 ± 0.03 in the recoil energy

range 40-65keV. Finally, the ZEPLIN I liquid xenon dark matter detector was discussed. The first data from this detector suggests a background rate of 20 dru in the 1-50keV energy range.

CHAPTER 5

Two Phase Liquid Xenon Detectors

In this chapter we focus on the theoretical and experimental motivations behind the two phase xenon detector method. In this configuration both scintillation and ionisation are detected by drifting electrons into the gas phase and producing secondary scintillation via electroluminescence. First the physics of electron drift in liquid xenon under the influence of an applied electric field is considered.

5.1 Electron Drift in Liquid Xenon

This section considers the physics behind the drift of electrons in liquid xenon. We treat electrons in a classical manner to interpret the form of drift velocity versus applied electric field curves [93]. In doing so, the physics involved will be highlighted and will give an insight into the expected signals from a two phase detector. The development of this discussion is influenced by the measurement of electron drift velocities in the liquid rare gases. Therefore a few comments on a typical drift velocity versus applied electric field curve are appropriate. In Fig 5.1 a typical drift velocity curve is sketched. The three characteristics that shall be discussed are: the low field linear dependence, the power law dependence between E^* and E_l and the saturation of the drift velocity at high fields.

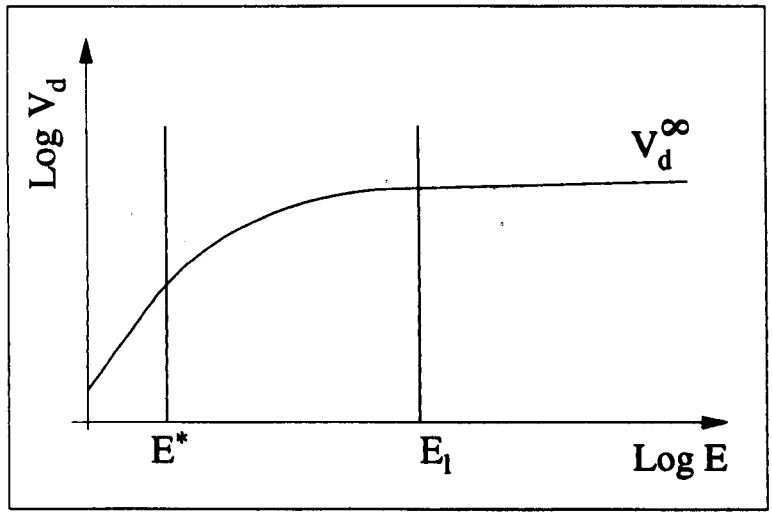


Fig. 5.1: A typical drift velocity curve for electrons in a noble gas. E^* is the field strength after which the drift velocity is no longer linearly dependent on the field strength and E_l is the field strength after which the drift velocity is saturated to its limiting value of V_d^∞.

5.1.1 Low Field Electron Drift, $V_d \propto E$

A condensed rare gas such as liquid xenon provides the simplest case for the understanding of the liquid state, due to the inert nature of the rare gas atom. The large mass, M, of the atom means that electrons colliding elastically with the atom will undergo large deflections but with small energy losses. Therefore at low fields a gas approximation to the motion of the electrons is applicable. In this case we have random motion of electrons driven by the force due to the electric field. The distance over which the electron is drifted is proportional to the acceleration on the electron due to the field. The drift velocity itself is proportional to the drift distance and, as the acceleration is proportional to the electric field strength, we can express the dependence of the drift velocity at low field strengths as in Equ 5.1.

$$V_d = \mu E \tag{5.1}$$

Where μ is the electron mobility and E is the field strength. For xenon the electron mobility is 0.22 $m^2V^{-1}s^{-1}$.

5.1.2 High Field Electron Drift

As the applied field is increased, small energy losses of the electron due to elastic collisions become compensated by the energy imparted to the electron by the field. The energy lost by an electron in an elastic collision is given by:

$$\Delta\epsilon_{el} = \frac{2m}{M}\epsilon \tag{5.2}$$

where m is the mass of an electron and ϵ is the initial energy of the electron, due to displacement in the field, before collision. In the case of xenon for an electron energy of 5eV $\Delta\epsilon_{el}$=3 $\times$ 10^{-5}eV. The characteristic distance between collisions in a medium of number density N, is $1/(N\sigma_e)$ where the cross section for an interaction is given by σ_e. Therefore the energy imparted to an electron

between collisions is $E/(N\sigma_e)$. The field strength E^* at which elastic collision losses are balanced by the energy gained by the field is therefore given by Equ 5.3.

$$E^* = \frac{2m}{M}\sigma_e N\epsilon \tag{5.3}$$

For E>E^* the field now acts to increase the kinetic energy of the electron entirely. As a result $\epsilon \propto$ E and therefore the drift velocity dependence on field strength is dependent on E by the relationship shown in Equ 5.4.

$$V_d \propto E^{0.5} \tag{5.4}$$

5.1.3 Saturation Velocity

At sufficiently high fields $E \gg E^*$ (E_l in Fig 5.1) the drift velocity of electrons saturates. To explain this phenomenon let us consider the case where the electron kinetic energy approaches ϵ_1, the potential of the xenon atom excitation energy. It can be shown that the energy imparted to an electron between collisions that result in excitation of the xenon atom, is too small to result in processes other than the excitation of the lowest lying excitation level. In these collisions all of the kinetic energy of the electron is lost. Therefore at high fields the drift velocity will saturate since the electron can gain no further energy. The value of the saturated drift velocity can be calculated as in Equ 5.5.

$$V_d^{\infty} = \left(\frac{\epsilon_1}{2M}\right)^{0.5} \tag{5.5}$$

Where ϵ_1 is the energy of the lowest lying excitation level in xenon. Using ϵ_1=8.34eV for xenon we calculate V_d^{∞} to be 1.8mmμsec^{-1} [93].

5.1.4 Summary of Electron Drift in Xenon

Electrons have a high mobility in liquid xenon and can be drifted under the application of an electric field. Here, the drift velocity varies depending on the magnitude of the field, being linear at low fields and proportional to $E^{0.5}$ at higher fields. The drift velocity saturates due to the electrons exciting atoms whereupon they lose all their kinetic energy. The time between exciting collisions is too short (for fields where $E < few \times 10^5 \mathrm{Vcm}^{-1}$) to enable the onset of excitation to higher levels than the lowest lying level. Whilst this theory is not completely rigorous it does explain the features in a typical drift velocity curve. However, from real data, we see that the saturation velocity predicted by this simple model can be quite different from the actual observed value. Experimental measurements of this quantity give a value of $2.8\mathrm{mm}\mu\mathrm{sec}^{-1}$ [112]. This could be due to the invalidity of the proposed theory from [93], or possibly due to impurities in the xenon. Nevertheless charge conduction through xenon is measured. The most recent data on drift velocities is shown in Fig 6.16 in Chapter 6. We use this data in the Monte Carlo simulations, as opposed to the theoretical predictions of this model due to the uncertainties involved in the modelling. In Chapter 6 the method used in the Monte Carlo model to track electrons is discussed in more detail.

5.2 Recombination Scintillation and Charge Drift

On production of charge by an ionising event in liquid xenon, electrons can recombine, giving scintillation, or alternatively be free to drift if an external field is applied. In the Monte Carlo simulations presented in Chapter 7 the proportion of electrons free to drift and those that recombine to produce primary scintillation is needed. The theory used in that calculation is discussed here.

The W-value for xenon was given in Chapter 3 as 15.6 eV/ion pair. Therefore the number of electrons produced by a gamma-ray is E_γ/W where E_γ is

the energy of the gamma-ray. In the simulations it is assumed that a single electron recombining produces a single photon. The proportion of electrons recombining is determined by the formalism in Equ 6.5. Photons are also produced from the excitation process in liquid xenon. The number of photons produced at zero field can be written as E_γ/W_s where W_s is the average energy required to produce a photon in liquid xenon. In what follows η is the fraction of scintillation produced by electron recombination and ν is the electron yield i.e. the probability of electron recombination suppression. Defining W_1 as the energy required to produce an excitation photon, $N_{ph}(E)$, the number of primary scintillation photons produced, can be written as,

$$N_{ph}(E) = \frac{E_\gamma}{W_1} + \frac{\eta E_\gamma(1-\nu)}{W} \tag{5.6}$$

where E is the local field strength. Assuming W and W_s are equal, W_1 is found to be

$$W_1 = \frac{W}{1-\eta}. \tag{5.7}$$

Therefore Equ 5.6 becomes

$$N_{ph}(E) = \frac{E_\gamma(1-\eta\nu)}{W}. \tag{5.8}$$

In the simulation η is taken to be 0.67 as suggested in the data from [94]. The formalism of ν is discussed in detail in Chapter 6, where experimental data is parameterised for coding purposes.

5.3 Charge Extraction and Electroluminescence in Xenon Gas

5.3.1 Charge Extraction

To detect optically the electrons created in liquid xenon from an interaction, they must first be extracted into the gas where electroluminescence can take

place. A detailed theoretical model of the extraction of charge from a liquid/vapour interface under the influence of an electric field does not exist in the literature. A simple model would be to consider the interface as a potential barrier to the electron. In this case the electron should be extracted if it has enough energy to overcome this potential. This is analagous to photoemission from a metallic surface. Experimental observations suggest that there is an extraction probability that increases with increasing field strength [115]. For, with an increased field, the potential barrier across the interface will be reduced and therefore more electrons should be extracted. We can postulate that electrons could become trapped at the surface as they are unable to gain sufficient energy from the field to pass through the interface potential as depicted in Fig 5.2. This could occur as random motions of the electron, due to thermal motion, are too small to provide sufficient acceleration of the electron in the direction of the field. If the field is perfectly uniform the electron is therefore permanently trapped. However in a more typical situation the liquid level is unlikely to be perfectly aligned (see Fig 5.2 for schematic). In such a

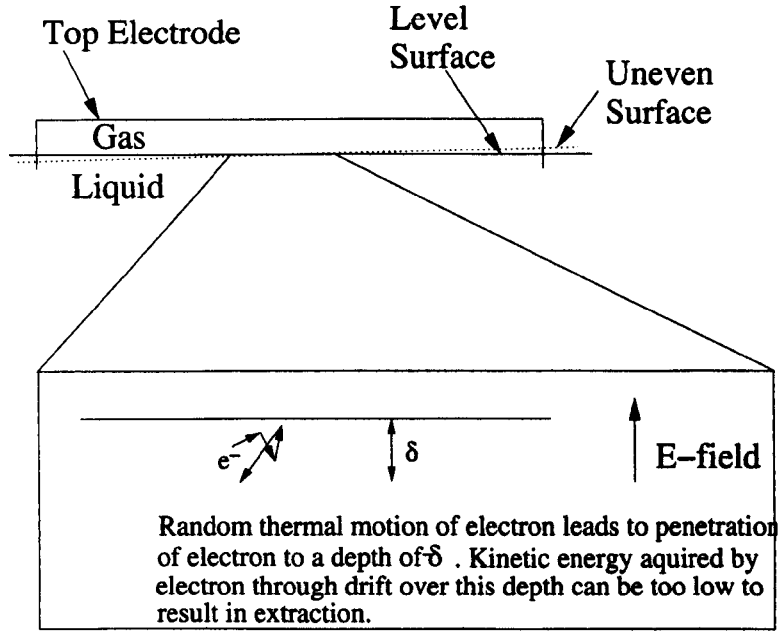


Fig. 5.2: Schematic of the liquid/gas interface with relation to electrode.

case it is possible that the electron migrates to the edge of the electrode, as the field gradient will be in the direction of the point at which the gas gap is minimised. Alternatively electrons could become trapped by electronegative impurities. It is clear that many possible mechanisms are involved in even this simple analysis. Experimental work is planned to investigate these phenomena. Certainly the theoretical scope of the proposed trapping of electrons needs further detailed consideration. The conclusion to this section, is that charge extraction is possible from liquid/gas interfaces in xenon. This has been observed in experiment. Indeed, it has been shown that at sufficiently high fields, of around 6kVcm^{-1} in the liquid, the probability of extraction of an electron reaches 1. Therefore by application of a field of this strength even single electron ionisation should become extractable from the liquid.

5.3.2 Electroluminescence

The second process on which the two phase detectors rely is electroluminescence in xenon gas. In the gas, the path length between collisions of the electron is much longer due to the reduced density of the medium. If the applied electric field is above a certain threshold then the electron is accelerated to energies sufficient to cause excitation of atoms to a state where luminescence can occur. This results in a continuous production of photons along an electron's path.

The yield of photons from this electroluminescence process is proportional to the number of electrons passing through the gas - provided the electric field is lower than 20kVcm^{-1} (with gas pressure 1.5 bar) -, i.e. $N_{ph} \propto N_{el}$, where N_{ph} is the number of photons produced for N_{el} electrons. In the case of a dark matter detector, where we are intent on detecting very low levels of ionisation, this process can be exploited to give a detectable light signal. Experimental investigations into the light output by [96, 97, 98] indicate that

the electroluminescence yield per electron is well approximated by Equ 5.9,

$$N_{ph} = 70(E - 1.3p)x \tag{5.9}$$

where E is the field strength, p is the pressure of the gas and x is the drift distance. For ZEPLIN III we expect $p = 1.5$bar, $x = 5$mm and $E = 8.34\text{kVcm}^{-1}$. Therefore a single electron would yield 224 photons during drift over the gas gap. Coupled with the statement in the previous section, that single electrons should be extractable from the liquid, this figure indicates that single electrons should be visible with appropriate instrumentation.

5.4 Two Phase Prototype Detector

A detector based on the concept of detecting the primary scintillation of light followed by electroluminescence in xenon gas after charge extraction has been constructed and operated at Imperial College. In this section a brief outline of the detector is given and some results are presented that confirm the two phase detection technique. In particular the ratio between primary and secondary electroluminescence for α-particles and gamma-rays is presented.

5.4.1 Prototype Design

A design drawing of the two phase prototype is presented in Fig 5.3. The xenon volume is cooled by a liquid nitrogen heat sink located above the top flange indicated in the diagram. This is thermally linked by a copper sleeve that runs down the outside of the detector and connects to the second large flange (level with the photomultiplier). The photomultiplier itself is positioned below the active volume of the detector, inside the liquid xenon. The active volume is defined as the cylindrical volume bordered by the field shaping rings, the aluminium mirror and the height at which the photomultiplier rests. A schematic of this volume is shown in Fig 5.4. An ^{241}Am source is mounted

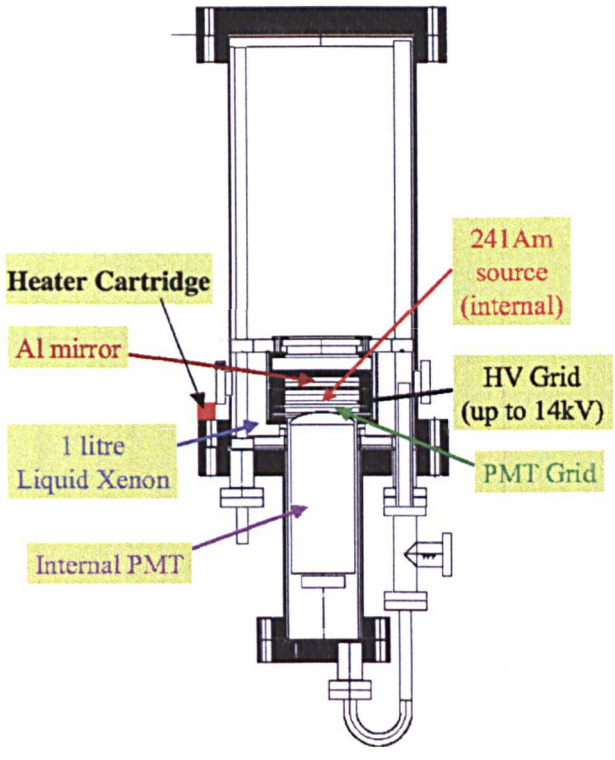


Fig. 5.3: Design drawing of the prototype chamber constructed and operated at Imperial College.

inside the detector on the high voltage grid. This source enables calibration of the system. Also ionisation produced by the emitted particles can be measured by drift and electroluminescence. The lower grid indicated in the schematic is set to the potential of the photocathode. This ensures that the field inside the photomultiplier is not affected by the drift field. A disturbance in the photocathode field would effect the quantum efficiency of the photomultiplier. The total liquid volume between the high voltage grid and liquid surface is $\sim$ 45cm^3. The dynode resistor chain for the photomultiplier is also within the xenon positioned below the base of the photomultiplier tube.

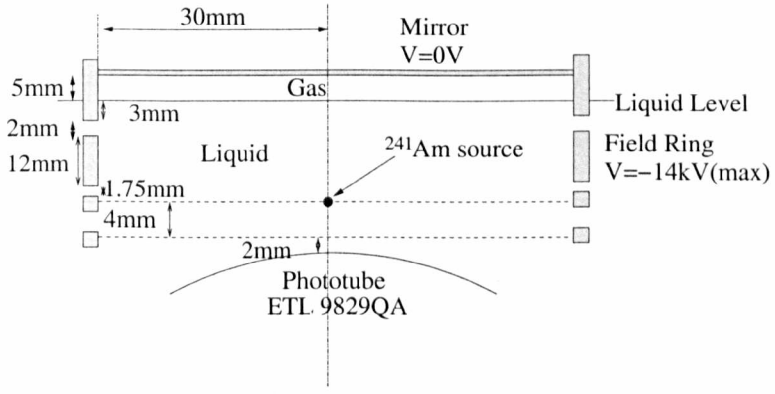


Fig. 5.4: Sketch of the internal structure of the electrode system.

5.4.2 Prototype Operation

Xenon gas, that has been purified using the method previously described, is passed into the cooled prototype chamber. During filling the gas can be passed through a filter which has a pore size of $\sim 1\mu$m. This removes particulate impurities from the xenon that would otherwise compromise the electrical properties of the active volume (by causing breakdown). Once the chamber is filled the temperature is controlled by an EROELECTRIC temperature control device. This regulates the on/off state of electric heaters that are positioned on the lower copper flange, see Fig 5.3. With this set up during stable running, the temperature is controlled to 0.1K stability. In this outline of the experiment, results from two modes of operation will be reported. The first mode is when the detector is run as a two phase detector. The second is when the detector is filled with liquid to the point when there is no gas gap between the liquid surface and the mirror. In this second mode, the detector operates as a drift chamber. By taking measurements of the charge arriving at the mirror from electrons created by the ^{241}Am source, it is possible to determine a limit on the lifetime of electrons in the liquid xenon.

5.4.3 Results from Two Phase Prototype

The main result achieved from the two phase prototype is the measurement of the ratio of the primary to secondary signals for α-particle recoils and gamma-ray scattering/photoabsorbtion events. To demonstrate the two phase principle consider Fig 5.5. The plot is of a event from the ^{241}Am source taken with

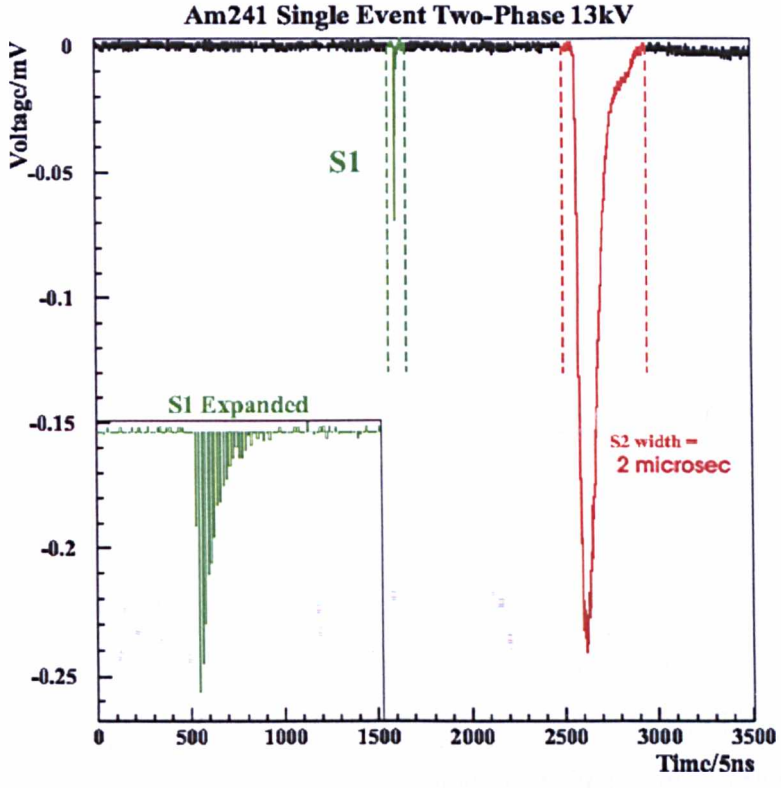


Fig. 5.5: Signal recorded by LeCroy digital oscilloscope. Digitisation is in 5ns bins. The primary (S1) and secondary (S2) pulses can clearly be identified. [99]

the potential between the field rings set at 13kV. The primary and secondary signals arising from recombination scintillation in the liquid and electroluminescence in the gas can be seen. The generic properties of this pulse are as follows. The primary pulse is much shorter and smaller than the secondary. The two signals are separated by a time τ_d=4μsec which is the drift time of the electrons from the event position to the surface. The width of the secondary is

the drift time of the electron in the gas, τ_{dg}=2μsec. In this sample event, the depth of liquid above the source position was in fact 11mm (contrary to the schematic in Fig 5.4), and the gas gap was 10mm. The pulse is also identified as an α-particle recoil due to its low S2/S1 ratio. The 5.49MeV α-particle has a very short range in liquid xenon. Therefore we can assume that the event originates from the source position. Assuming linear motion of the electrons between the source and the surface, we can approximate the drift velocities in the liquid and the gas at, V_{dl}=2.75mmμsec^{-1} and V_{dg}=5.00mmμsec^{-1}. The value for the liquid drift velocity complements the earlier theoretical discussion that suggested saturation of electron drift velocity at high fields to a value of 2.8mmμsec^{-1}. The final observation to take from this data is the large size of the secondary signal. An α-particle interaction in xenon is expected to have a high dE/dx. That we observe a large electroluminescence pulse from the densely ionising α-particle, suggests that the observation of ionisation from nuclear recoils is possible with this detector.

Data has also been acquired to compare the ratio of primary to secondary signals arising from gamma-rays and α-particles. During experimentation it has become apparent that the gamma-ray secondary pulse is very large in comparison to that of the α-particle, as would be expected. This means that sampling of both sets of pulses simultaneously is difficult due to the limitations of the dynamic range of the 8-bit LeCroy scope. To avoid saturation due to the secondary pulse, the potential across the field rings was set to 7kV. In Fig 5.6 the ratio S2/S1 is histogrammed for a set of events where the trigger is set on the amplitude of the secondary pulse. In this data, a ^{60}Co gamma-ray source (1.17MeV and 1.33MeV gamma-ray energies) was placed close to the detector wall, level with the active volume. This provides a gamma-ray flux incident over the entire liquid xenon active volume. It is worth noting that the gamma-rays are likely to interact before reaching the active volume, as there is significant material between the source and the active volume. However the energy of the interaction is not crucial in this measurement, as, by taking

the ratio of S2/S1, we essentially remove the energy dependence. Gamma-ray

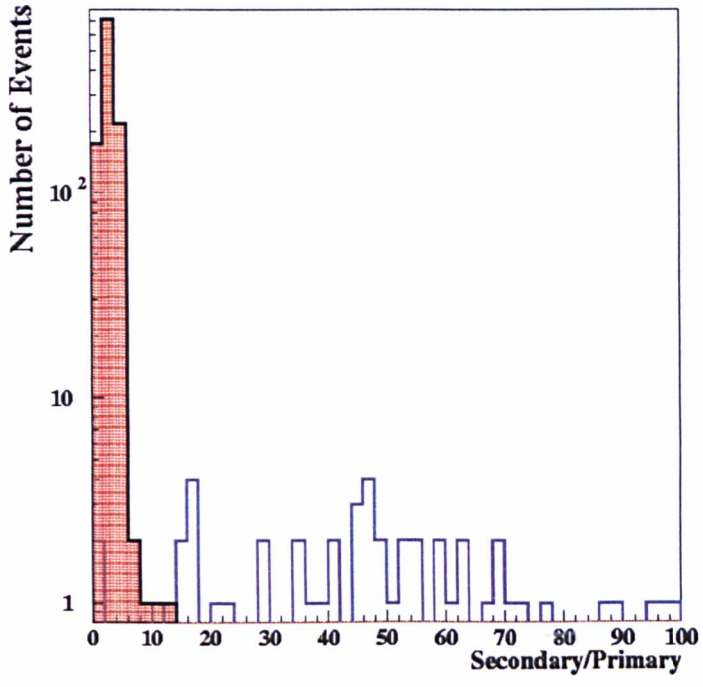


Fig. 5.6: Histogram of the S2/S1 ratio for events in the two phase prototype detector. The low ratio distribution (red) is attributed to α-particles (5.49MeV), the blue distribution to gamma rays (external ^{60}Co source) [99].

and α-particle signals are identified by τ_d. As the α-particles interact within <1mm distance from the source, the drift time of these events is constant. By cutting on the τ_d times of signals it is therefore possible to discriminate with $\sim$ 100% efficiency between α-particles and gamma-ray events. Fig 5.6 shows the distribution of S2/S1 for this experimental configuration. The two interaction types are indicated by the colouring in the histogram. The α-particle distribution is well defined at S2/S1 $\approx$ 5. The gamma-ray distribution has a much broader signature with a mean value of $\approx$ 50. Based on this data alone we can observe that, if we set a discrimination level at S2/S1=16 (well removed from the α-particle distribution), the discrimination factor is $\sim$90%.

There are subtleties involved in this measurement, which we shall not address

here (see next section). However, this data does prove the discrimination expected from a two phase system.

Charge Measurements and Electron Lifetime

The prototype can be run as a drift chamber. In this case the active volume is filled completely with liquid and a charge signal is read from the mirror. The signal from the mirror is passed into an Amptek A250 charge sensitive amplifier. The data aquisition was triggered by the primary scintillation pulse. The charge resulting from both ^{241}Am α-particles and cosmic rays was measured. The trigger level was increased in the latter case to avoid source events contamination. Longer drift times were measured by triggering on cosmic ray events in the detector with a reduced field applied across the electrodes. This could not be done with α-particles as at low fields insufficient ionisation is removed from the interaction due to recombination. High noise levels in the system meant readings had to be averaged. Typical plots from the charge measurements can be seen in Fig 5.7. The drift time measurements indicate that the electron lifetime in liquid xenon is $> 20\mu$sec. Indeed further measurements increased this estimate to $> 60\mu$sec.

5.4.4 Conclusions from Prototype Experiments

From the experimentation conducted so far, both the discrimination technique and the electron lifetime have been measured. The two phase experimentation demonstrates the power of discrimination between α-particles and gamma-rays. The calculated value of the discrimination factor earlier was based purely on the observed distributions. Difficulties from the fact that the ^{241}Am source is placed in a lead boat of diameter 1.2mm (see Fig 5.8), and that the gamma-ray interactions will preferably occur at the edge of the detector, were ignored. The lead boat essentially shadows the primary scintillation light produced by the α-particle interactions. Comparison of the α-particle primary scintillation energy spectrum with that of the 60keV gamma-ray distribution indicates that

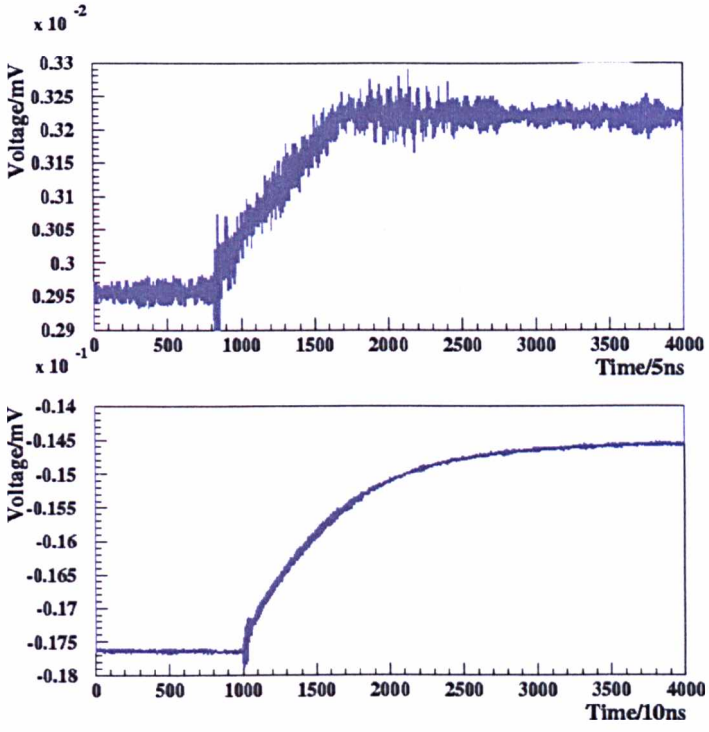


Fig. 5.7: Averaged charge output from α-particles with a 2kV applied field (top) and cosmic rays with a 200V applied field (bottom)[99].

this shadowing reduces the primary scintillation output by about a factor of 10. The preference of gamma-rays to interact at the edge of the detector reduces the S2/S1 ratio to that which would have been measured should the event have occured at the centre of the detector geometry. This is due to the reduction in the field strength in the gas phase at the periphery of the active volume, which decreases the electroluminescent signal from the gas in accordance with Equ 5.9. Both of these considerations will improve the previously calculated discrimination level. To fully understand the results of the prototype detector a Monte Carlo simulation is being undertaken by members of the Imperial College Dark Matter Group.

The fact that the electroluminescence signal, for a known energy deposition from a known particle, is dependent on the radial position of that event in the

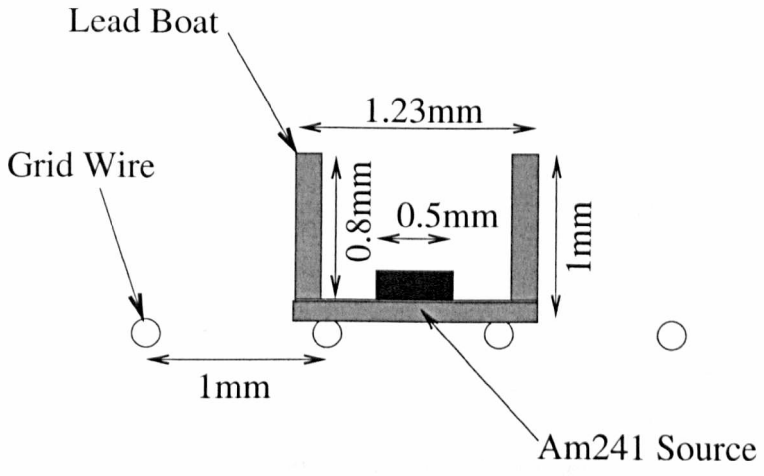


Fig. 5.8: Sketch of Am-241 source and lead boat in the two phase prototype detector.

active volume, is problematic in the prototype chamber. In the next section we address the design of the ZEPLIN III detector and a solution to this problem is suggested. Monte Carlo modelling in Chapters 6 & 7 examine this solution more closely.

5.5 The ZEPLIN III Dark Matter Detector

The design of ZEPLIN III is based upon the same physics principles that have been proven by the prototype detector. The main considerations during the design process were:

a) maximisation of light collection

b) maximisation of active target mass

c) maximisation of charge extraction

d) minimisation of radioactive contamination

e) minimisation of electronegative contamination

f) minimisation of cost.

The finalised design drawing is shown in Fig 5.9.

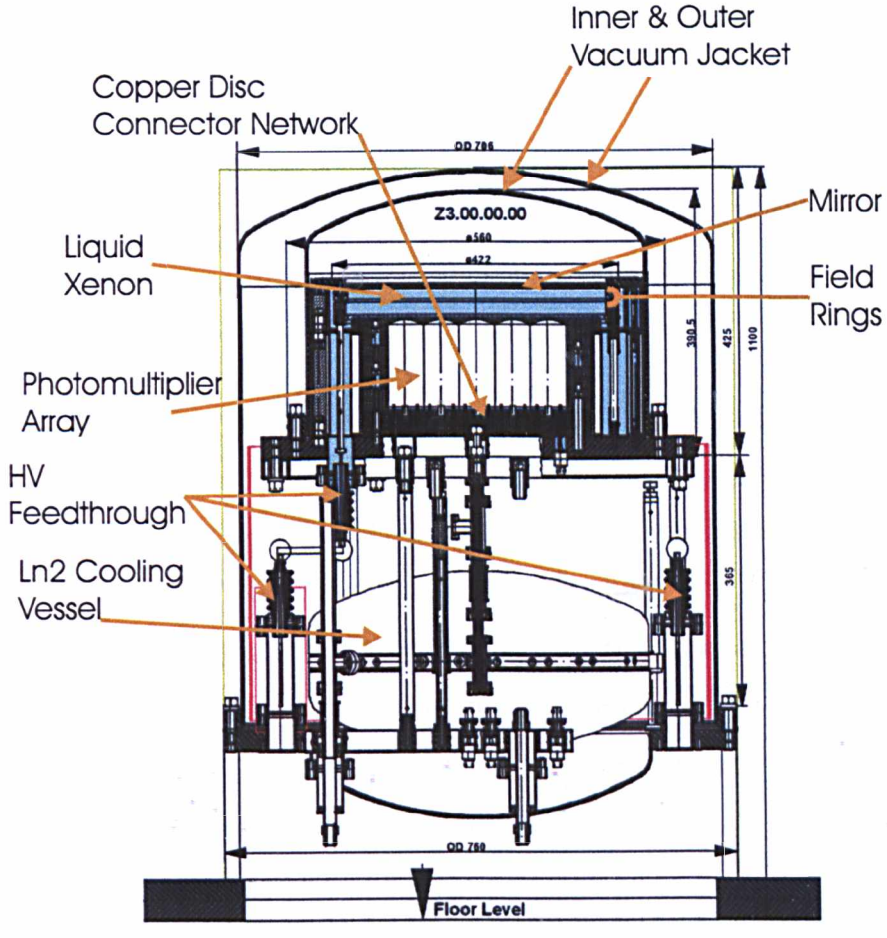


Fig. 5.9: Design drawing of ZEPLIN III detector.

5.5.1 Target Maximisation and Contamination Minimisation

The target volume - indicated as 'Liquid Xenon' in Fig 5.9 - has a 'slab' geometry viewed by 19 photomultipliers. The mirror surface at the top of the detector will be a thin film ($\sim$ a few μm) deposit of aluminium on a copper

substrate. The slab approach ensures a high light collection and that the charge drift distance is minimised. In total the detector will contain 30kg of liquid xenon, of which 15.2kg resides within the electrode structure. This is therefore the maximum target mass. Whilst we only have 50% useful xenon target the other half is used passively to provide insulation for the high voltage feedthroughs, shield the active volume from background radiation and provide conductive heating between the active xenon and the cool copper walls. The high voltage feedthroughs are rated to 40kV. ZEPLIN III is intended to run with 35 kV across the field rings - this corresponds to about $8kVcm^{-1}$ and $16kVcm^{-1}$ in the liquid and gas active regions respectively.

All large metal parts surrounding the active volume are high purity oxygen free copper. Radioactive impurities in the copper are at levels of $<$ 1ppb ^{238}U & ^{232}Th and $<$ 1ppm ^{40}K. The photomultiplier radioactivity is discussed further in Chapter 6. The purification procedure used for ZEPLIN III will be based upon our experience of the prototype detector. The new system will be designed to enable manipulation of larger gas volumes. The detector will be assembled in a clean area held at positive pressure with inflowing air passed through Class 100 filtration units.

5.5.2 Brief Overview of ZEPLIN III Design

ZEPLIN III is currently under construction at Imperial College. In this overview the main design concepts of the detector will be discussed.

The cooling system in ZEPLIN III is complex. Liquid nitrogen will be held in the vessel indicated in the sketch Fig 5.10. The mass of material to be cooled is large. Therefore the cooling power delivered to this mass must be maximised. To accomplish this a procedure based on flowing liquid nitrogen through the flange supporting the photomultipliers (F1 from hereon) has been proposed and the system designed accordingly. Within the circumference of F1 a burrow will be bored. This burrow will be connected to the liquid nitrogen vessel via two

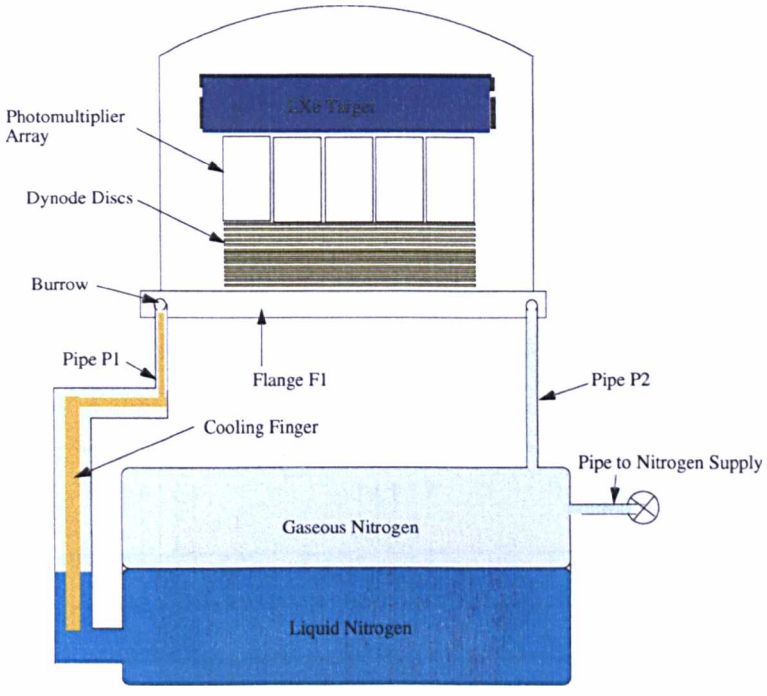


Fig. 5.10: Sketch of Zeplin III Design

pipes, one of which will connect beneath the liquid level of the nitrogen (P1 from hereon), the other will connect above into the gaseous nitrogen (P2 from hereon). Within P1 there will be a copper finger that extends from F1 down the length of P1. With the setup as described, cooling can be controlled in the following fashions. First, the level of the liquid nitrogen in the containment vessel dictates the extent of submersion of the finger in P1 and hence the cooling reaching the target vessel. Second, for rapid cooling, a positive pressure can be applied within the containment vessel which will subsequently force a rivulet of nitrogen through the burrow in F1. The latter of these two methods is vital to ensure cooling of the detector from room temperatures is achieved within the shortest possible time. The former method will be employed during stable operation of the detector. This technique will require experiment to clarify the procedures and parameterisation.

The other novel detail in the design of ZEPLIN III is the dynode resistor chain. With 19 photomultipliers immersed within the xenon the problem arises as

to how to connect them. Each tube requires 14 connections, 12 to define the potential of the dynodes the anode and the cathode. Therefore to connect each through F1 would require 266 feedthroughs. This was deemed unacceptable, due to cost and the machining that would be necessary to accomplish the connections. To remove this problem 12 discs were designed that would provide the dynode potentials to each photomultiplier. The interconnectivity of these plates is better understood by the example sketch in Fig 5.11. The use of 12

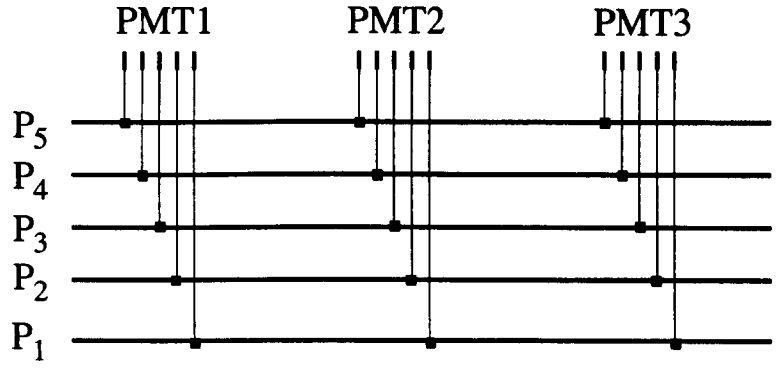


Fig. 5.11: Sketch of the disc arrangement for 3 example photomultipliers. Five connections are shown to five discs at potentials P_1,P_2,P_3,P_4,P_5

discs in this arrangement reduces the number of connections through F1 from 266 to 50 (38 connections are still required for the cathode and anode of each tube).

When constructed ZEPLIN III will be transported to the Boulby Mine, where it will be integrated with a Compton veto device. The veto device is similar to that depicted in Fig 4.20, only placed above the detector rather than below it, since the photomultiplier tubes in ZEPLIN III are below the sensitive volume. The veto is used to give anti-coincidence signals which arise from gamma-rays scattering through small angles in the active detector volume, and then being detected in the veto scintillator. In Chapter 6 the efficiency of the veto in reducing the background count is investigated. There are several technical areas which are still under investigation. The first is the ability to level the detector

so that the liquid level is parallel to the mirror to within < 1mm accuracy. The second is the form which the data acquisition system will take. With 19 photomultiplier tube signals digitising at 1ns intervals for a pulse length of 30μsec the total size of a single event is going to be about 0.5 megabytes.

5.6 Summary

In this chapter the two phase liquid xenon technology has been introduced and discussed. Results from a two phase prototype system have been presented, and discrimination between α-particles and gamma-rays has been measured. The results are consistent with 90% discrimination with the prototype cell design. Light collection effects in this test cell reduce the discrimination abilities of the test cell. The expected correction of a factor of 10 to the primary scintillation output from α-particles would increase the discrimination to $\sim$ 100%. Finally the design of the ZEPLIN III detector was introduced and examined.

The next chapter of this thesis reports Monte Carlo simulations of the ZEPLIN III detector.

CHAPTER 6

Monte Carlo Simulations of ZEPLIN III

6.1 Introduction

In this chapter we will focus on work into the evaluation of the performance of the ZEPLIN III detector. The general approach has been the compilation of a suite of computer codes, written in Fortran-77, to simulate the response of the detector and verify the two phase approach to dark matter detection. The work can be summarised under the following headings, each of which we will address in detail presenting results from the simulations:

- Light Collection
- Electron Drift
- Electroluminescence and Event Reconstruction

The motivations for these simulations are threefold: energy threshold, background and discrimination. These three concerns are ultimately the main measures of the efficacy of a dark matter detector. The aim is to reduce energy threshold to increase resolution of low energy events which, as mentioned previously, are expected from nuclear recoils (hence WIMPs).

6.2 Light Collection in ZEPLIN III

In the light collection modules of the simulations, we consider only parts of the detector geometry which are associated with the direct reflection of light. The following light collection simulations use GUIDEIT-V2.0 [100]. This is a widely used Monte Carlo package designed for modelling scintillator and lightguide systems. The code is used primarily as an engine over which the specifics of the ZEPLIN III problem are built.

6.2.1 Geometry and Materials Definition

In the light tracing simulations, we specifically targeted the ZEPLIN III internal structure which has a significant effect on the reflection of photons produced by interactions in the sensitive volume of the xenon mass. This gives an advantage of simplicity in the coding. After adopting this approach the geometry in Fig 6.1 was utilised.

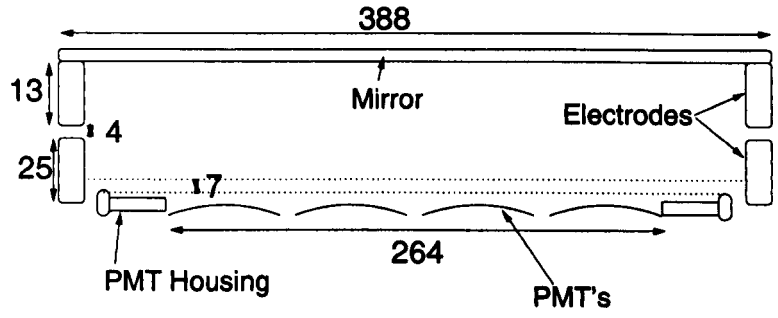


Fig. 6.1: Schematic of the light system in the ZEPLIN III internal geometry. Included are the electrodes, mirror and PMT housing. All numbers are measurements in millimetres.

The shapes are modelled in three dimensions. Thus the electrodes are modelled as cylindrical surfaces, the mirror as a circular surface and the LXe/GXe interface as a circular surface. The PMT housing is actually a circular surface within which are embedded black circular surfaces that represent the positioning of the photomultipliers. For a description of how to create geometries in

GUIDEIT the reader is referred to [100] on the understanding that GUIDEIT has evolved since 1993. Finally it should be noted that for all the simulation work the centre of the detector (defined as the centre of the central tube, see Fig 6.2) is placed at (10,10,10) in the (x,y,z) Cartesian coordinate system of the Monte Carlo. This is merely a facet of the programming and has no physical significance. We now look at the specifics of each component.

The Electrodes

In the actual detector the electrodes will be made of copper upon which will be deposited a thin layer $\approx 1\mu$m of an aluminium reflective coating. This coating is reputed to have a reflectivity at 175nm of between 80-90%. The lower electrode ring is centred on the same point as the centre of our coordinate system. The upper electrode is a combination of two connected cylindrical surfaces as indicated in the table below.

Component	Centre (x,y,z)/m	Radius/m	Height/m	Surface Finish	Reflectivity
Lower Electrode	(10,10,10)	0.194	0.025	Specular	0.9
Upper Electrode(Part I)	(10,10,10.029)	0.194	0.013	Specular	0.9
Upper Electrode(Part II)	(10,10,10.042)	0.194	0.005	Specular	0.9

Table 6.1: Table detailing the positions of the electrodes in the light simulation.

The definitions of the surface finish and reflectivity coefficients which are quoted in the table are the ones used throughout the main parts of the simulation work. The effects of altering these parameters on the detector performance were investigated and will be reported later.

The Mirror and PMT Housing

Essential in the light collection of both the expected primary and secondary signals is the presence of the polished mirror and PMT housing. These are both constructed in a similar way to the electrodes in that they are made of copper with a thin reflective aluminium coating. Their geometric positioning is given in Table 6.2.

The Photomultiplier Array

Component	Centre (x,y,z)/m	Radius/m	Surface Finish	Reflectivity
Mirror	(10,10,10.047)	0.194	Specular	0.9
PMT Housing	(10,10,9.996)	0.184	Specular	0.9

Table 6.2: Table detailing the positions of the mirror and PMT housing in the light simulation.

The tubes are arranged in a hexagonal close-packed pattern, as indicated in Figure 6.2, to give the maximum active area to dead space ratio. In the code these circular surfaces are referred to as 'gates'. When a photon hits a gate it is booked. In the following analysis of the GUIDEIT output the photon counts are adjusted to account for the quantum efficiency of the tube which is assumed to be 20% - the expected value for the EMI 9829QA tubes at 175nm. The quartz face of the tube is also taken into account. In the simulations we place a 2mm quartz sheet above the plane of the PMT's, to reproduce the Fresnel refraction and reflection expected from the PMT tube faces. The PMTs are also numbered for identification purposes. The geometric information of the photomultiplier ensemble is given in Table 6.3.

Component	Centre (x,y,z)/m	Radius/m
PMT 1	(10,10,10)	0.0235
PMT 2	(10.053,10,10)	0.0235
PMT 3	(10.0265,9.9541,10)	0.0235
PMT 4	(9.9735,9.9541,10)	0.0235
PMT 5	(9.947,10,10)	0.0235
PMT 6	(9.9735,10.0459,10)	0.0235
PMT 7	(10.0265,10.0549,10)	0.0235
PMT 8	(10.106,10,10)	0.0235
PMT 9	(10.0795,9.9541,10)	0.0235
PMT 10	(10.053,9.9082,10)	0.0235
PMT 11	(10,9.9082,10)	0.0235
PMT 12	(9.947,9.9082,10)	0.0235
PMT 13	(9.9205,9.9541,10)	0.0235
PMT 14	(9.894,10,10)	0.0235
PMT 15	(9.9205,10.0459,10)	0.0235
PMT 16	(9.947,10.0918,10)	0.0235
PMT 17	(10,10.0918,10)	0.0235
PMT 18	(10.053,10.0918,10)	0.0235
PMT 19	(10.0795,10.0459,10)	0.0235

Table 6.3: Table detailing the positions of the PMT's in the light simulation.

Xenon and Quartz Optical Properties

The optical properties of the electrodes and mirror have been defined. For

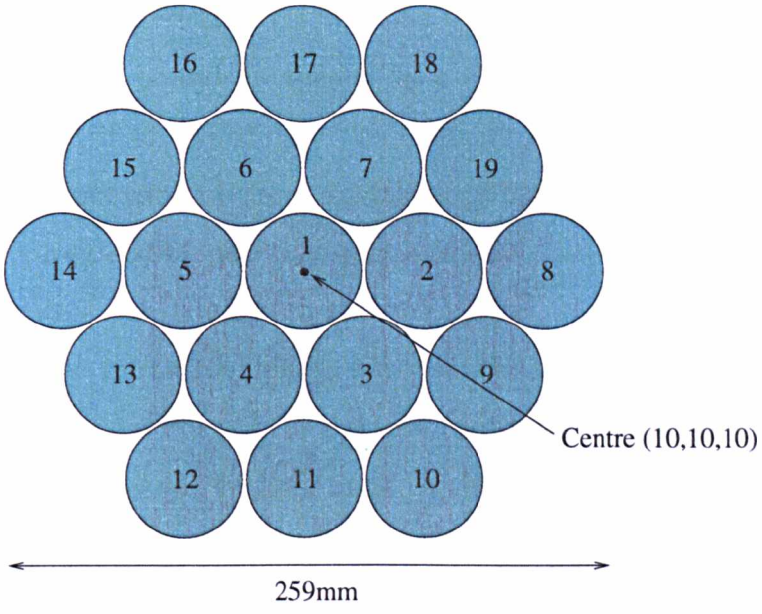


Fig. 6.2: The PMT array in ZEPLIN III. Each tube has an active photocathode diameter of 47mm.

xenon and quartz the important optical properties for the simulations are the refractive indices of each and the attenuation length for 175nm in each material. For quartz we took the usual value of 1.49 for the refractive index [124]. For liquid xenon we used n_{lxe}=1.59 [101]. The refractive index depends on the density of the liquid and therefore the temperature. The value we use is consistent with a liquid temperature of 170K. For the gaseous xenon we assume a refractive index of 1.

6.2.2 Physics Processes In Light Collection Simulation

The GUIDEIT Monte Carlo code includes the following physics processes:

- Fresnel reflection and refraction at refractive index boundaries
- specular and diffuse reflection at defined reflective surfaces
- light attenuation over a given path length.

Fresnel Reflection and Refraction

Light incident on a boundary defined by a change in refractive index will be refracted and reflected according to probabilities derived from the Fresnel equations. The computation of these probabilities is carried out in the GUIDEIT code. The processes of relection and refraction are most important at the interface between the liquid and gaseous xenon. Here we have a significant difference in the refractive indices between two nonconducting media. The effect, as we shall see later, is for light sourced from the gas to be lensed onto the PMT array. Conversely, light from the liquid incident on this interface is refracted towards the edges of the detector, or internally reflected.

Specular and Diffuse Reflection

In our code all metallic surfaces are defined as specular surfaces i.e. they reflect light according to Snell's Law where the angle of incidence and the angle of reflection, are equal. Diffuse reflection is not expected from surfaces in the defined ZEPLIN III geometry, assuming all metallic surfaces are prepared such that variations in the surface are restricted to scale lengths less than the wavelength of the incident light. However, simulations were run to see the effect of diffuse reflections. In this case incident light is reflected according to Lambert's cosine law of reflection, that is to say that the probability of an incident photon being reflected into an angle θ varies as cos θ.

Light Attenuation

The code also accounts for attenuation of photons over a given path length. We define the liquid xenon volume as the main source of light attenuation. The attenuation length of 175nm light in xenon has been measured by several groups, results indicate 0.3m$\leq L_{att} \leq$1m, Refs [102, 103, 104, 105, 106]. In our simulations we assumed a worse case scenario of L_{att}=30cm. Photon attenuation is then characterised by an exponential probability density function given by:

$$P(attenuation) = e^{-\frac{X}{L_{att}}} \tag{6.1}$$

where X is the path length of the photon. This distribution is then integrated and sampled.

6.2.3 Procedure for Light Collection Simulation

To assess the light collection efficiency of the geometry two types of simulation were run. The first was a program that produced events in the liquid xenon volume at random positions (x,y,z), within the boundaries dictated by the geometry. The aim here was to understand the efficiency with which the detector would detect the primary scintillation from an event in the liquid volume. A similar simulation was conducted in the gas to assess the effciency of collection for electroluminescent light. Secondly a scan of the (x,y) plane was performed at various heights in the detector, which enabled qualitative analysis of the dependence in the collection effciency on height and (x,y) positions, enabling us to characterise the uniformity of response. Simulations were performed in both the liquid xenon volume and the gaseous xenon gap.

In these simulations the number of initial photons emitted from each pseudo-interaction site was chosen to be suitably large - 10000 photons from each position - such that statistical fluctuations in the resulting efficiency calculations would be negligible. The photons were emitted isotropically from the source position over 4π.

6.2.4 Results of Light Collection Simulations

Results from simulations of random event positions throughout the liquid xenon volume indicate an overall light collection efficiency of 33% $\pm$ 5%. Fig 6.3 shows the positions of events for which light tracing was performed. The histogram in Fig 6.4 shows the distribution of light collection as a percentage. Notice the double peaked profile of this distribution. This is an effect induced by the geometry of the system. There are two distinct classes of events. Firstly the events for which direct light is the large proportion of the detected light

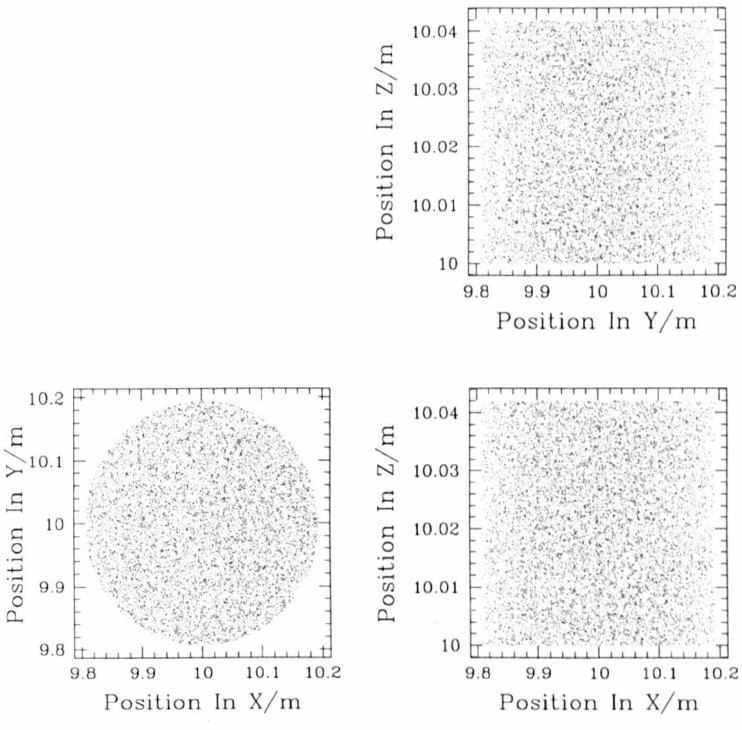


Fig. 6.3: Plots showing a sample of 10000 events created in the liquid xenon volume of the ZEPLIN III geometry, in the three planes YZ,XY,XZ.

and secondly events for which there is little or no direct light detected from the source to the photomultipliers. The blue curve in this distribution shows the percentage light collection for events within a defined radius of the detector, in this case 115mm from the central axis of the detector.

In Fig 6.5 the positions of the sources for events with a light collection efficiency greater than 35% in the first instance and less than 35% in the second are plotted. Our point here is exemplified by these plots. Events with collection efficiency less than 35% fall outside the radius at which the photomultipliers are positioned. Conversely for events for which the efficiency of collection is greater than 35%, they fall entirely within this radius. One can also see in these plots the actual shape of the PMT array being outlined by these events, and notice low efficiency areas in the dead areas between the tubes. A simple conclusion can be drawn from these simulations. If in some way we can gain

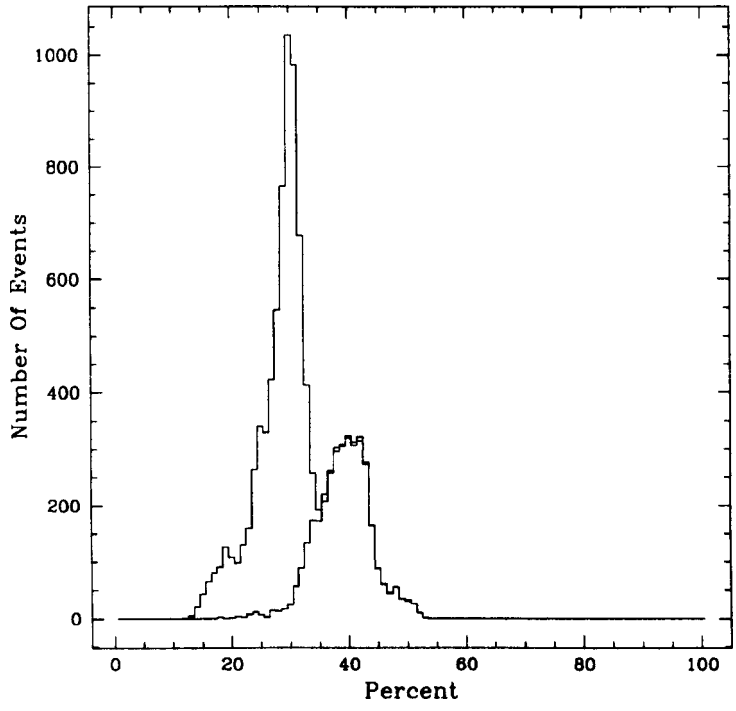


Fig. 6.4: Histogram of light collection efficiency for events in positions as in Fig 6.3. The blue curve only includes events from within a radius of 115mm from the central axis of the detector.

positional information, then active selection of events from high light collection efficiency areas will decrease the energy threshold of the detector. Pulse height correction could also be used to improve resolution.

In addition the uniformity of response in the z-direction was assessed. This was achieved by setting up scans at a variety of heights in the detector. Here we present results from scans at five levels in the detector. The results are shown in Fig 6.6.

Each bar in each plot represents the percentage of photons arriving on the defined photomultiplier gates from an event started from that XY position. The number of initial photons used was 10000, so statistical errors are negligible. Table 6.4 below gives the average light collection efficiency for each level and a width on the distribution over that plane. We note that for successive

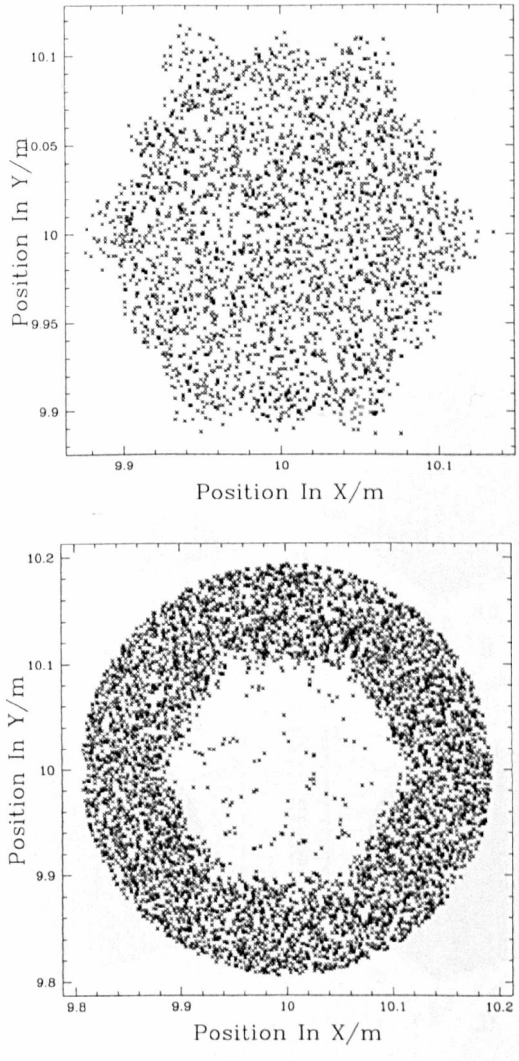


Fig. 6.5: Source positions in the XY plane for which the light collection is greater than 35% (upper plot), and less than 35% (lower plot). It is possible in these plots to note the PMT array distribution itself, and in particular areas of low efficiency between the tubes.

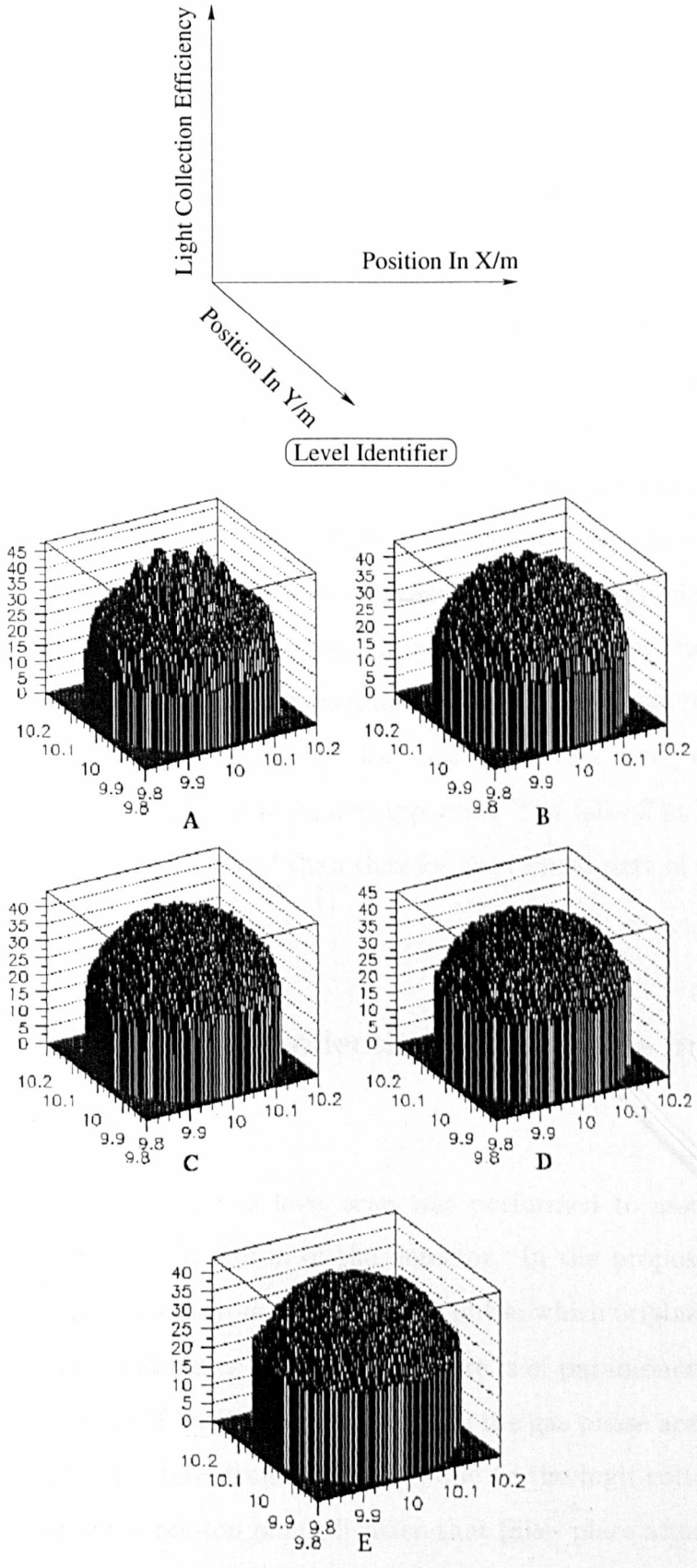


Fig. 6.6: Results from light collection efficiency scans. The levels are at 8.4 (A), 16.8 (B), 25.2 (C), 33.6 (D) and 41.9 (E) mm.

Level Identifier	Height Above PMT Array/mm	Average Collection Efficiency	Width
A	8.4	33%	7%
B	16.8	33%	6%
C	25.2	33%	6%
D	33.6	34%	5%
E	41.9	34%	5%

Table 6.4: Table of average light collection efficiencies for 5 levels in the liquid volume

planes the light collection efficiency distributions are consistent with uniform response. The scan results agree well (as one might expect) with the previous randomly distributed events. In plot A, the modulation in the efficiency is seen. This is due to the events occurring directly over a photomultiplier. This 'image' of the PMT array is washed out with successive steps in z. This effect is due to detected light from the sources becoming increasingly dominated by reflected light, and direct photons spreading more evenly over the photomultiplier array. Although there is concordance in the light collection between successive levels in the liquid volume, for each individual level, evidence for variation in the light collection is clearly apparent. The fall-off at the edges of the geometry is more pronounced than that for the central part of the detector volume.

6.2.5 Results of Light Collection Simulations in the Xenon Gas Gap

In the gas phase a similar five level scan was performed to assess the light collection efficiency in this region of the detector. In the proposed detector, signal triggers will be taken from the secondary pulse, which originates from the gas phase. Thus the efficiency to detect light here is of paramount importance to the threshold of ZEPLIN III. The signals from the gas phase are expected to be large, compared to those from the liquid, due to the high voltages applied across this gap and the photon multiplication that takes place after an electron extraction from the liquid phase. Previously we mentioned the importance of

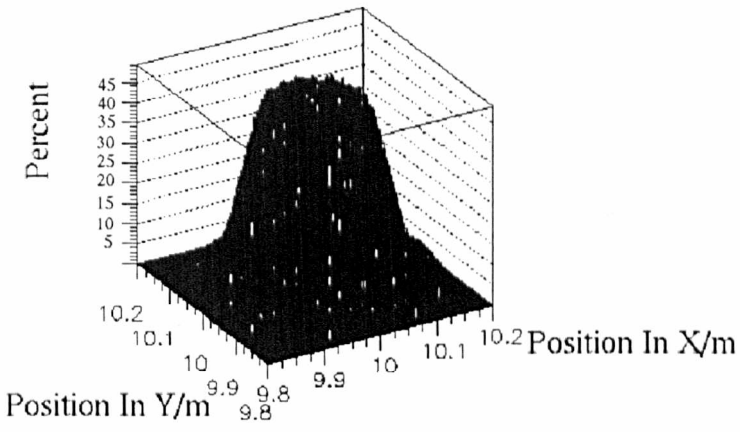


Fig. 6.7: Light collection distribution for sources started 1mm above the liquid level in ZEPLIN III.

the liquid/gas interface in the light collection efficiency of our detector. Before expanding on this we present a similar plot to those shown in Fig 6.6 for a scan in the gas phase.

This scan was performed 1mm above the liquid level of ZEPLIN III. The reflectivities of the surfaces were 90% as in the previous simulations of the liquid phase. We find both a similarity and a difference between the light collection in the gas and in the liquid. Firstly we note that the peak light collection in the gas is similar to that in the liquid. The striking difference however is the rapid fall off of collection as we move farther to the edges of the detector. The histogram of the percentage light collection for all events simulated in the gas shows this effect more powerfully. In Fig 6.8 we have again combined a histogram of events occuring at different radii within the detector. The red histogram indicates the inner events (0mm $\leq$ r $\leq$ 60mm), the blue edge events(132mm $\leq$ r $\leq$ 194mm) while the black indicates the others, where r is the radial position of the event in the (x,y) plane. The inner events (red histogram) are again the better detected as they were in the liquid volume. On close inspection we see that the distribution of these events has tightened at the higher end of sensitivity and also that the centroid of the peak

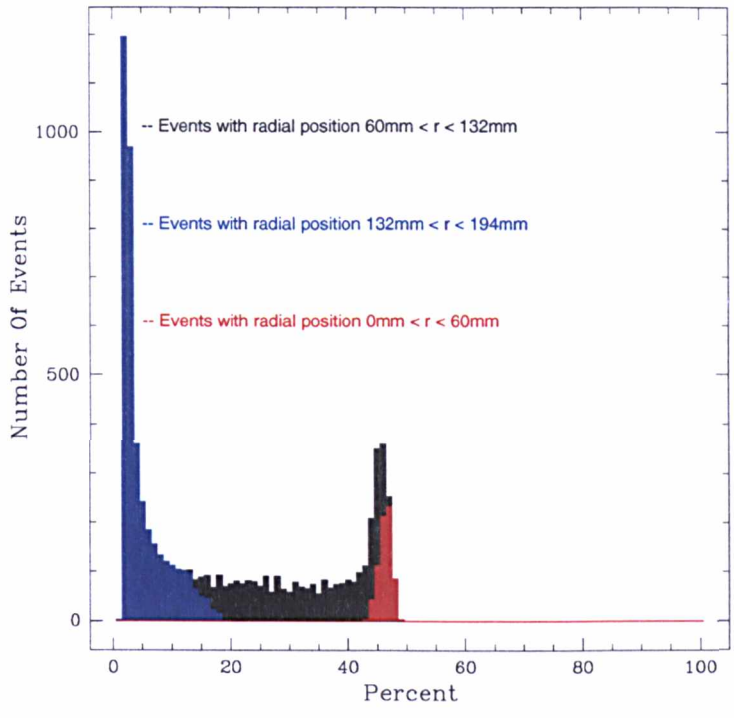


Fig. 6.8: Histogram of light collection percentage for events set off 1mm above the liquid level in the gas.

has moved noticeably to higher light collection efficiencies. Overall, however, the total distribution shows a much greater dispersion of collection efficiencies and in particular we note the increase of low efficiency events between 0 - 10% (blue histogram). To explain the characteristics of the gas phase curves we must return to the importance of the liquid/gas interface. We noted before the lensing effect that this interface will have on incident photons. In the central regions of the detector this effect increases the amount of light onto the PMT array in comparison to an event in the liquid volume. However, at this interface, we also expect partial reflection of incident photons so that whilst some of the most central events have an increased light collection compared to that expected in the liquid, this effect is dominated at larger radii by reflection from the surface.

6.2.6 Black Surfaces and Lambertian Reflection

Simulations were performed to investigate the worst case scenario, where all the surfaces are non reflective. In this instance the average light collection from events in the liquid was 12.4 ± 10.5%, and for events in the gas the figure was 9.3 ± 8.2%. Fig 6.9 shows a plot of the average light collection efficiency for events in the gas as a function of radius.

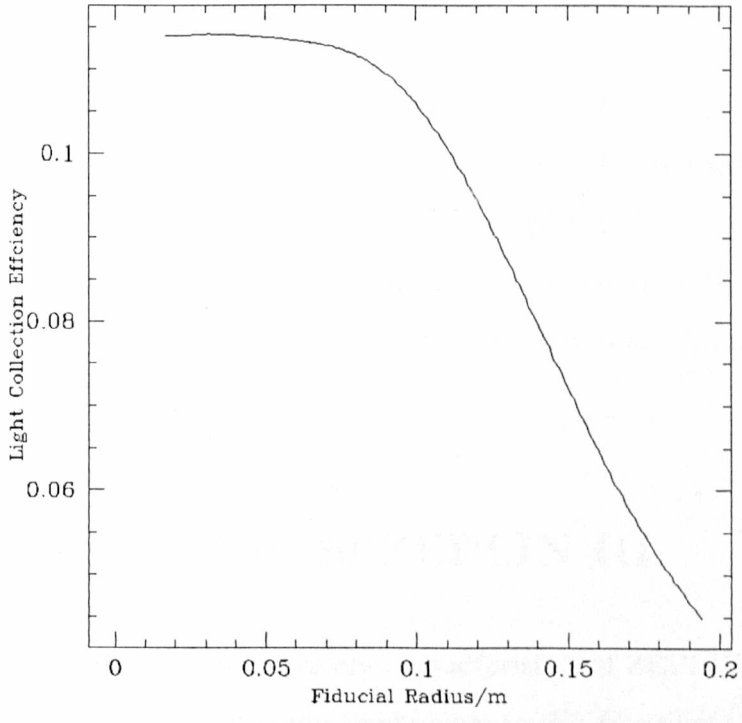


Fig. 6.9: Light collection efficiency in the gas region as a function of radius in the detector; all surfaces non reflective.

A further set of simulations were performed to measure the effect of replacing the specular reflective surfaces with Lambertian reflectors. For this scenario the light collection efficiency was 33 ± 6% (1σ) in the liquid. Therefore specular and diffuse reflectors of equal reflectivity give close to equal average light collections.

6.2.7 Summary of Light Collection Simulations

In conclusion, the geometry of ZEPLIN III and its light properties have been thoroughly investigated in the configuration and with the characteristics expected of the light system. The liquid volume has been shown to have an average efficiency of collection of 33 ± 5 % with spatial variations accounted for by the geometric properties of the detector. Light emitted from the gas gap has also been simulated and shown to have a decreased average efficiency of collection of 22 ± 16% with a differing spatial dependence to that in the liquid. This is due to the effects of the liquid/gas interface that acts both as a lens to enhance collection at the inner regions of the detector volume, and as a reflective surface to decrease the efficiency of collection towards the edges of the detector. The simulations demonstrate that with sufficient position reconstruction and the ability to define a fiducial volume based on this information, light collection can be maximised if events are solely taken from the centre of the detector volume.

6.3 Electron Drift in ZEPLIN III

We are now aware of the light system characteristics of ZEPLIN III. The next important feature of our detection mechanism in this two phase method is the detection of electrons. When a particle interaction occurs in xenon there are two channels for detection. The primary scintillation light from excited xenon atoms or dimers, and ionisation. The power of this technique as we have seen is derived from our ability to 'see' small amounts, down to single electrons, of ionisation. To do this a large potential is applied across the electrodes (Fig 6.1) to force electron drift towards the mirror and out into the gas phase where electroluminescence occurs which can be detected by the phototubes. The morphology of the field is extremely important, so it should be ensured that the field uniformity is maximised and electron drift paths are well defined and understood. The purity and cleanliness of the xenon is also paramount.

Electronegative impurities and 'dust' in the liquid xenon will capture drifting electrons and reduce the electroluminescence output. The simulations that follow examine the electric field distribution using a finite element analysis tool. Electron paths are constructed according to the calculated field distribution. Characteristics of electron drift and extraction from the liquid/gas interface are also addressed.

6.3.1 Electric Field Simulation

Electric field simulations of ZEPLIN III exploit the cylindrical symmetry of the electrode structure. With such symmetry a model in two dimensions is adequate to describe the field distribution, and in later use this can be extended to three dimensions by simple rotation. The model was created using Quickfield^{TM}, an interactive environment for electromagnetic, thermal and stress analysis. The software allows one to define a geometry with certain electrical properties: ϵ_r the relative electrical permittivity and U the potential to which a part is raised. A mesh of points is constructed (maximum of $\approx$200,000 nodes), the problem analysed, and an output file containing the field strengths at these nodes is produced. In this simulation a mesh with 45263 nodes was sufficient to give a density rendering $\approx$1mm resolution within the drift region of the ZEPLIN III geometry. The mesh was concentrated in proximity to the electrodes to increase resolution as this part of the geometry is of paramount interest electrostatically. Electrons created in this region will follow curved tracks, resulting in different drift times to those expected in the uniform field region of the detector. Electrons created very close to the electrodes will drift to the surface of the electrode before reaching the gas phase and electroluminescence is suppressed.

Fig 6.10 shows the mesh used in the electrostatic calculations.

Results from Electric Field Simulation

The results from the software can be given in two ways. For inclusion in the

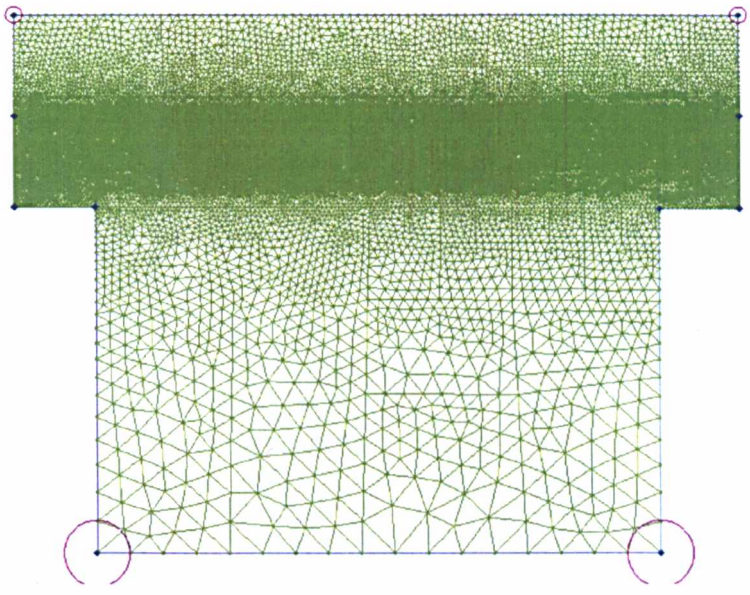


Fig. 6.10: The mesh used in the electrostatic calculations. Resolution limits the detail at the centre where the mesh densities are maximised.

main body of our simulations, we take a raw text file that describes the field completely in two dimensions. There are also features that enable graphical representation of the field, and for completeness one of these is shown in Fig 6.11. The distribution of the field strength throughout the ZEPLIN III geometry is shown. The potential difference between the two electrodes in this case is 15kV, the lower electrode (A) at -15kV and the mirror (B) held at ground. There are two grids (modelled as circular planes) at C and D. The grid at C is at the same potential as the lower electrode (A). The grid at D is held at -1500V the expected photocathode potential of the photomultiplier tube. The presence of the grids C and D results in the 'reverse field region' (RFR), by which we mean that the direction of the field is reversed relative to that in the uniform field region of the target volume. One of the actions of this RFR is to prevent ionisation from energy depositions in the liquid volume directly above the PMTs being drifted to the gas region. Therefore effectively we have a 7mm dead space above the tubes which acts as a shield to radioactive background from the tubes. In the gamma background simulations in Chapter 7 the effect

of this shield is investigated.

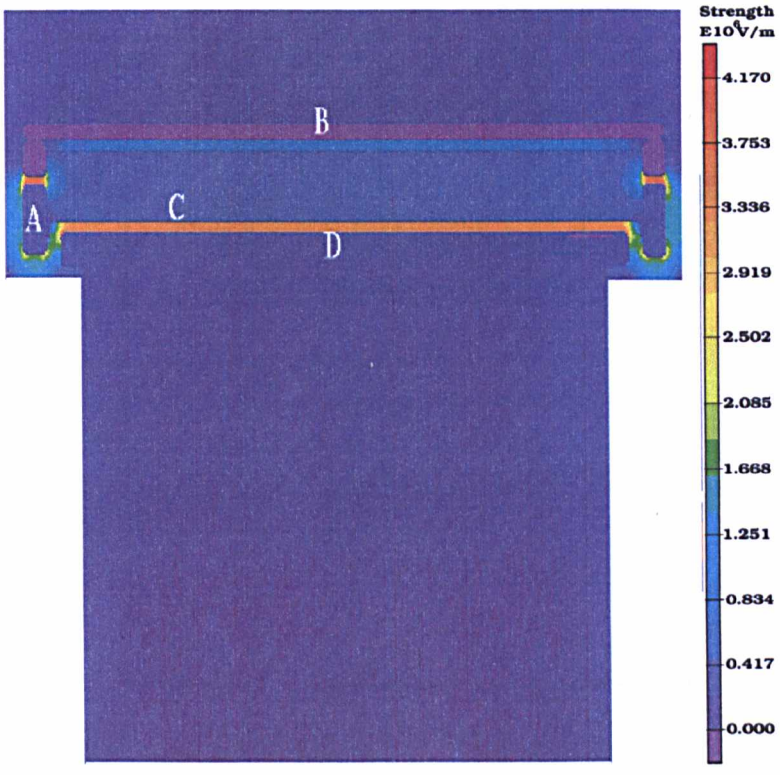


Fig. 6.11: Field strength plot for ZEPLIN III geometry. The four labelled parts are: A - the lower electrode at -15kV, B - the mirror/upper electrode at 0V, C - the position of the lower electrode grid at -15kV and D - the position of the PMT shield grid at -1500V. The orange region is the reverse field between the two grids C and D.

From Fig 6.11 the impression is that the field is extremely uniform within the detector volume up to the areas near the electrodes. To aid visualisation of this Fig 6.12 is a plot of the equipotentials of the field. In this figure it is clear to see that the equipotentials are near flat for most of the region within the electrode structure.

Fig 6.13 is a blow up of the region one centimetre near to the electrode. Clearly visible in this magnified image is the curve of the field lines along which electrons will drift if produced in this region.

Quantitatively it will be useful to pick some average values of the field in

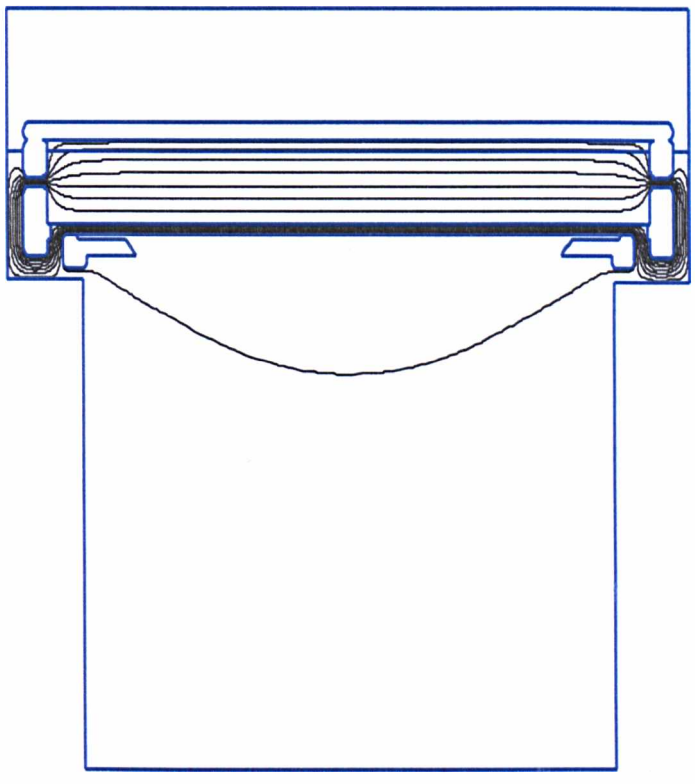


Fig. 6.12: Equipotential plot for ZEPLIN III geometry. The inner blue structures are the electrodes, mirror and grids. The outer blue boxes are the boundaries set on the problem.

certain regions.

Region	Average E-Field Strength/kVcm^{-1}
Uniform Field Region In Liquid	4.17
Uniform Field Region In Gas	8.34
Reverse Field Region (RFR)	33.36

The electric field simulation provides a fine resolution map of the electrostatic properties of the ZEPLIN III geometry. In the full Monte Carlo simulation, the field map is used to calculate the trajectories of electrons and the field dependence of the light output of events in the gas and liquid phases.

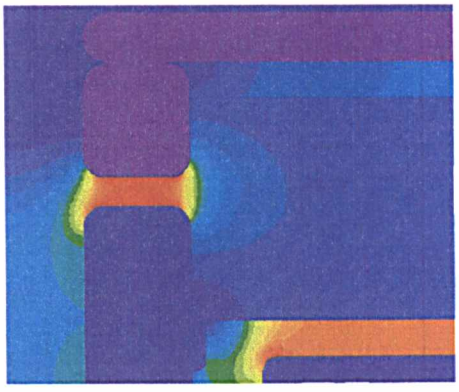


Fig. 6.13: Magnified graphical representation of electric field strength near the electrodes. The colours follow the weighting as defined in Fig 6.11.

6.3.2 Electron Drift Simulation

One of the underlying principles of ZEPLIN III is the drift of electrons through liquid xenon. In the Monte Carlo simulations we make some assumptions about the physics: we assume that any electrons produced in an ionisation event are stopped within a distance which is negligible compared to that required by the accuracy of the modelling. Ultimately we aspire to millimetre level positioning of events in the detector. Therefore any physics processes which affect the detector's ability to do this at an insignificant level can be ignored. Let us take an example to highlight the assumption. A Compton scatter in the liquid xenon deposits an energy of the order of 100keV. The Compton electron released can undergo three important interactions: ionisation and excitation of nearby atoms through collisions with orbital electrons, and *bremsstrahlung* (radiative losses through Coulombic interactions with the nucleus). Our assumption will only hold if the combined effect of these three mechanisms is sufficient to stop an electron within 1mm. The stopping power of the first two processes is calculated from the theory by Hans Bethe [107]. Additionally the *bremsstrahlung* contribution is found from a combination of theoretical calculations and accurate numerical results, taken from [109]. The National Institute of Standards and Technology (NIST) provides a facility that performs

these calculations online and the reader is referred to [110]. Presented here is a graph produced by the NIST software, Fig 6.14.

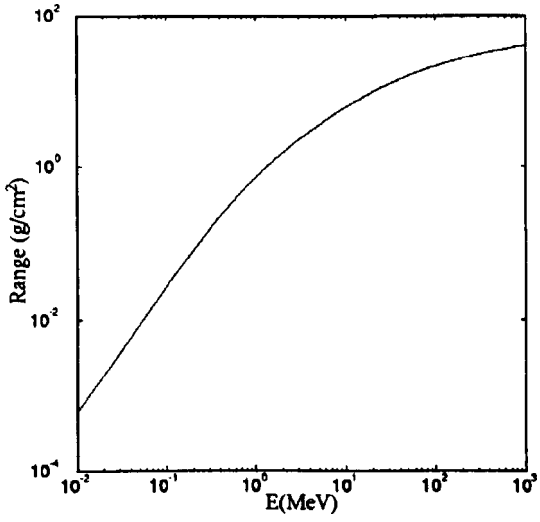


Fig. 6.14: Graph of the projected stopping power of xenon for electrons of energy, E.

We can see for our example electrons of energy 100keV that the range is of the order 10^{-2}gcm^{-2}. By taking a value of 3.05 gcm^{-3} for the density of liquid xenon and evaluating (range/ρ) we infer the expected distance travelled by an electron of this energy to be $\sim$30μm. This is negligible compared to the constraints we defined earlier. This thermalisation path that the electron follows will of course increase at higher energies. However interactions at these energies are of little interest to a dark matter detector and will be easily recognised from the large signal.

Secondly we assume that the dispersion of the electron cloud produced from ionisation at the event site as it travels through the liquid xenon is also negligible. Dispersion of thermalised electrons as they are drifted through liquid xenon can be approximated by combination of the two equations:

$$\mu = \frac{v_d}{E} \tag{6.2}$$

$$D = \mu k_b \frac{T}{e} \tag{6.3}$$

where μ is electron mobility (m^2/V.s), v_d is drift velocity (m/s), E is field strength (V/m), D is the dispersion coefficient, k_bT the thermal energy of the liquid xenon and e the electronic charge [111]. Taking the following values: μ ~0.22 m^2/V.s (at T=164K) and $t_{d_{max}} \sim 20$ μs, the dispersion coefficient is D~3000mm^2/sec [111]. Therefore, the associated amount of dispersion expected for a maximum drift length in ZEPLIN III is 0.06cm^2. Assuming that this dispersion is circular over a plane the radius of dispersion is 0.1cm. Again our initial assumption is vindicated.

The problem of electron drift in the liquid xenon is now reduced to following a 'test charge' from an event site to the liquid/gas interface. The velocity of the electron is modelled using the equations given in Eqn 6.4. Using these equations allows the Monte Carlo code to model the position, speed and drift time of the electrons.

To complete this section we look at some modelled electron trajectories. The plots in Fig 6.15 show electron paths through the modelled potential. In these

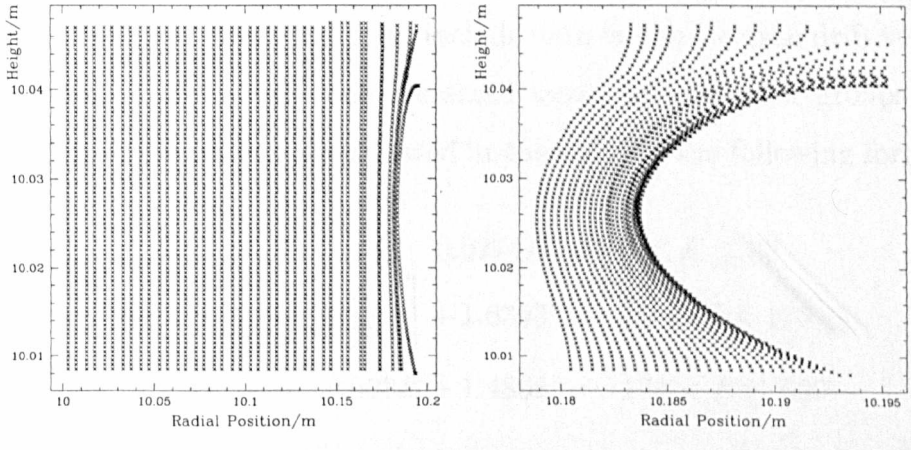


Fig. 6.15: A plot of Monte Carlo results for electrons produced in the modelled electric field for ZEPLIN III (See Fig 6.11). On the left trajectories for the entire xenon volume and on the right a zoom plot of trajectories close to the detector edges.

plots electrons are 'born' just above the lower electrode grid at rest. The paths are then followed according to the electrostatic motion equation, Equ 6.4. The

paths follow the field precisely as expected. The right hand plot shows a zoom of the region close to the electrodes. Following the tracks it is clear to see that at a radius of 0.182m the tracks are no longer reaching the defined gas/liquid level which resides at a height of 10.042m. Therefore, electrons produced from an interaction outside this radius will not produce electroluminescence. This will be referred to as the Electrode Dead Area (EDA). As mentioned, tracks are curved near the EDA. Therefore an event here will produce a longer drift time compared to a similar event in the uniform field region. The only way to address the problems associated with the EDA is to distinguish events in this region from events in the uniform region of the detector. This is the driving force behind the position reconstruction work. If it is possible to resolve the (x,y) coordinates for any event, then this process can be used to discard non-linear effects in the EDA.

6.3.3 Drift Velocity Simulation

To model the time separation of primary and secondary light detection and the duration of the secondary pulse, we include data on the electron drift velocities in liquid xenon. This has been measured separately by other groups [112]. The plot in Fig 6.16 is approximated in the code by the following formulae:

$$v(E) = \begin{cases} 0.0274E & : \quad 0 < E \leq 30 \\ \left[\frac{-2.9081}{1+e^{\frac{(E+3.2308)}{34.635}}}\right] + 1.6393 & : \quad 30 < E \leq 170 \\ 0.008E + 1.4862 & : \quad 170 < E \leq 600 \end{cases} \tag{6.4}$$

where $v(E)$ is the electron velocity (mmμsec^{-1}) at field strength E (Vcm^{-1}). These data are for fields of low strength (max. 0.6 kVcm^{-1}). Both linear regions fit the data with R^2 values of 0.9757 (low field range) and 0.9906 (high field range). At higher fields the modelling assumes a linear extrapolation with saturation at 3mmμsec^{-1} as indicated from the measurements in [112].

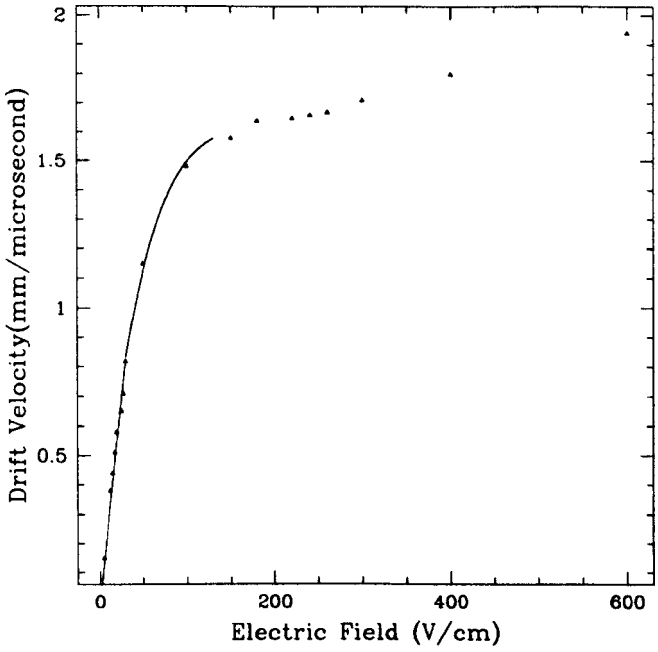


Fig. 6.16: Electron drift velocities in liquid xenon as a function of applied electric field. Calculated curves from fitting equations Equ 6.4 are shown in blue, red and yellow.

6.3.4 Electron Yields for Gamma Rays in Liquid Xenon

When a gamma ray deposits energy and creates electrons in liquid xenon the percentage of electrons that can be removed from that interaction and drifted is dependent on the initial energy deposition. Electrons imparted with more energy from the inital interaction will be able to overcome potentials that may have otherwise trapped slower moving electrons. Therefore, to model gamma rays interacting in our detector we must account for this effect. Again we turn to previously published information and perform some simple fits to allow integration into the code. In simulation, we reproduce these distributions with Equ 6.5.

$$\frac{1}{N_e} = \frac{30.07}{E_\gamma E} + \frac{0.40}{E} + 1.00 \tag{6.5}$$

where N_e is the fraction of electrons free to drift for a field strength E, after a gamma interaction of deposition E_γ. This simple formulation comes from

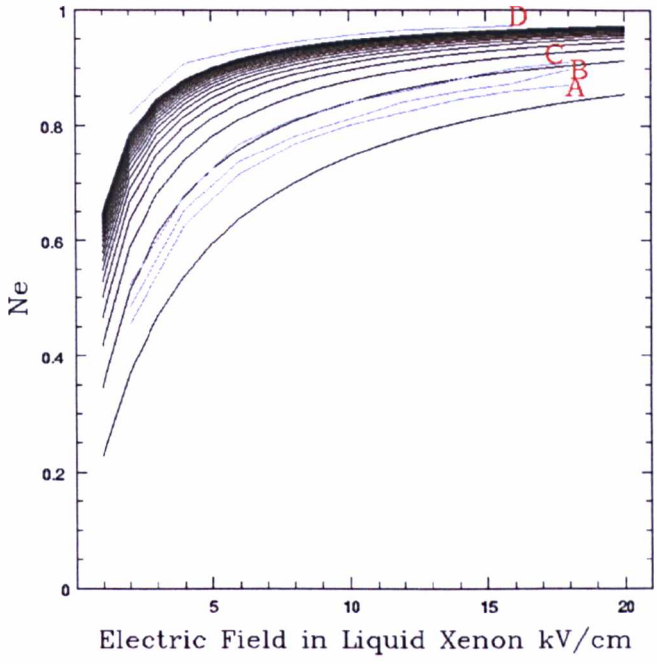


Fig. 6.17: Electron yield for gamma rays of different energies. Blue curves represent data for incident gamma energies at 15.3, 17.3, 21.4 662 keV [113] (600keV data) [114] (15.3,17.3,21.4keV data). Black curves represent model parameterisation for 10keV$\leq E_\gamma \leq$ 200keV with ΔE_γ=10keV between curves.

plotting the available data [113, 114] as $1/N_e$ vs 1/E and realising the straight line dependence in Fig 6.18. Further comparison when plotting the gradient of these lines versus $1/E_\gamma$ renders another straight line dependence which in turn gives us the relationship in Equ 6.5.

6.3.5 Electron Extraction from Liquid Xenon

When electrons have been drifted from their production site to the surface of the liquid xenon, the simulation incorporates the probability of extraction of an electron from the liquid xenon. Here we again use experimental determination of the dependence of electron extraction with field strength at the liquid surface. We use the data shown in Fig 6.19, taken from [115].

The method of fitting is similar to the equations in Equ 6.4. Again we use

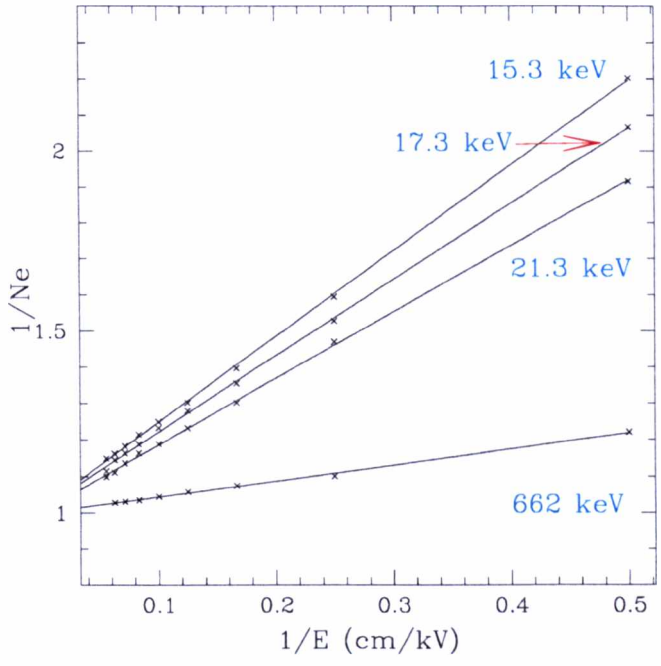


Fig. 6.18: Straight line fits for data presented in Fig 6.17.

three approximations to the form of Fig 6.19 shown in Equ 6.6.

$$P(E) = \begin{cases} 0.3941E - 0.6935 : 1.75 < E \leq 3.9 \\ 0.0117E^3 - 0.2127E^2 + 1.3021E - 1.696 : 3.9 < E \leq 6.5 \\ 1 : 6.5 < E \end{cases} \quad (6.6)$$

Where $P(E)$ is the probability of extraction of a single electron from the liquid xenon at a field strength E (in $\mathrm{kVcm^{-1}}$).

Electrons are extracted if a randomly chosen number produced in the code is less than, or equal, to the probability of extraction.

6.4 Electroluminesence and Event Reconstruction

In this section we will not consider in detail the physics involved in the production of photons from multiplication in the gas phase of ZEPLIN III. Rather

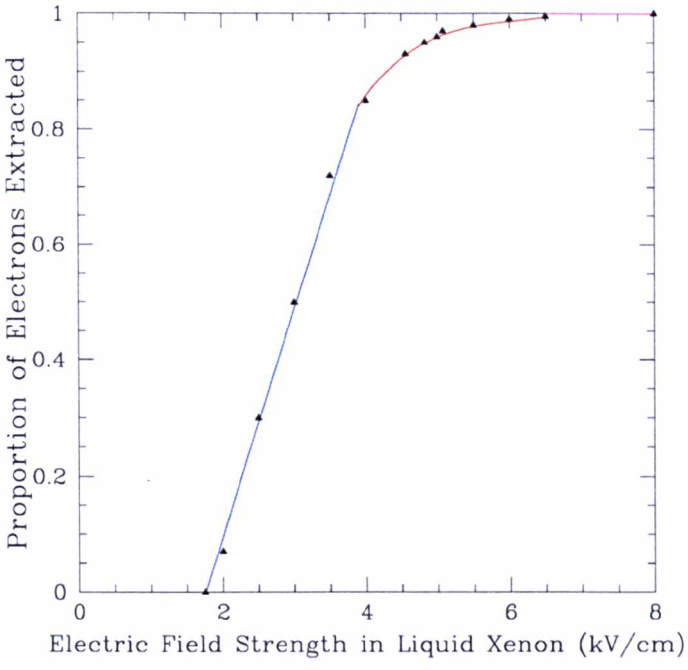


Fig. 6.19: Extraction probability as a function of electric field strength in liquid xenon. Data points fitted according to Equ 6.6 [115].

we will take empirical photo-yield values and look at the prospects for event reconstruction in ZEPLIN III. In this chapter we have examined the capabilities for light and charge collection in the proposed detector. The measure of the efficiency of our detector to locate events is a reflection of a combination of these detector functionalities. Event reconstruction will enable us to define a fiducial volume. This section looks only at the theoretical response of our detector, in that events for reconstruction are created not from a real input energy spectrum, but from defined user inputs to aid systematic studies.

6.4.1 Electroluminescence Calculations

The process of drifting an electron in the gas is similar to that used in the liquid. We use the same coding technique and the same equations of motion for the electron in an electric field as in Equ 6.4. In the gas we need to Monte Carlo the production of photons as the electron passes through the gas.

The step size in the Monte Carlo is chosen such that the number of photons produced by a single electron is statistically significant, of the order of ten. The number of photons generated by a single electron is given by Equ 5.9, which was given as:

$$N_{ph} = 70(E - 1.3p)x \tag{6.7}$$

N_{ph} is the number of secondary photons, E is the electric field strength ($\mathrm{kVcm^{-1}}$), p is the gas pressure in atmospheres and x is the distance through which the electron has travelled in the xenon gas. For a step size of 0.5mm, a field strength of E=10$\mathrm{kVcm^{-1}}$ and gas pressure p=4 atm, Equ 6.7 yields N_{ph}=21 per electron. This satisfies our constraint on single electron extraction into the gas. It should be noted that Equ 6.7 is taken from an experiment where electrons are being drifted through gaseous xenon at room temperature. The correction for the effect of low temperatures is in the value of the pressure. We should use the vapour pressure of xenon at 173K. Fig 6.20 shows three points of data taken from [117, 118]. A simple linear extrapolation between the two low temperature points yields a xenon vapour pressure of ~4 bar and we adopt this for the simulations.

In the Monte Carlo code the number of photons calculated from Equ 6.7 is inputted to the light collection software and traced as before. We have already investigated the performance of the light system for sources in the gas, which coupled with the above formula, suggest for a single electron the total number of photons detected should be ~13 (including a 20% quantum efficiency in the photomultiplier tubes) in the more efficient light collection regions. This calculation uses Equ 6.8 to evaluate the expected number of photons detected.

$$N_{det} = N_{ph} \times \frac{d}{x} \times L_{coll} \times Q_{\lambda} \tag{6.8}$$

Where N_{det} is the total number of photons detected, N_{ph} is the number of photons produced over a distance x (with field and pressure values the same as in the previous calculation using Equ 6.7), d is the total drift distance

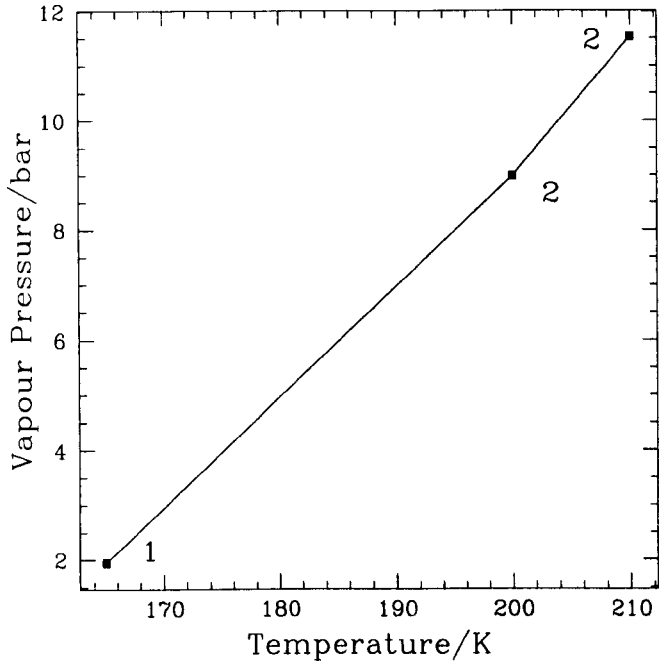


Fig. 6.20: Vapour pressure of gaseous xenon as a function of temperature. Point 1 taken from [117] and the points 2 taken from [118].

(taken as 5mm), L_{coll} is the light collection efficiency (taken as 30%) and Q_λ is the quantum efficiency of the tubes (taken as 20%). This number of detected photons should be sufficient to enable event reconstruction in the (x,y) plane.

6.4.2 Event Reconstruction

The configuration of the ZEPLIN III dark matter detector is very close to that of an Anger camera [119]. This method of employing an array of photomultiplier tubes as an imaging system has been utilised in medical imaging since the early 1970's, where sub-centimetre accuracy has been reported [120]. However our system differs from the classic gamma camera set-up in that:

- there is no internal collimator usually utilised in gamma camera imaging to select the direction of the photons incident on the camera
- a liquid/gas interface is present in the optical system.

For the two reasons above we cannot necessarily use previously reported algorithms for spatial reconstruction. In our analysis of the spatial resolution of our detector we will use a template matching technique [121]. In this technique a Monte Carlo is performed to produce template photomultiplier distributions at pre-defined heights in the gas. The template runs use large numbers of photons to reduce the effects of statistical fluctuations. The output from these separate template files is then compared to any test output file using χ^2-reduction. An example of an output PMT template is shown in Fig 6.21. This figure shows

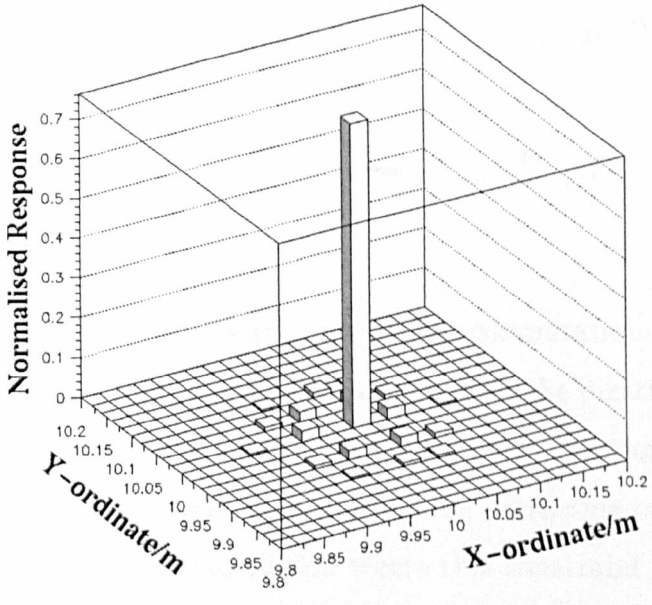


Fig. 6.21: Simulated normalised photomultiplier response for an event along the central axis of ZEPLIN III.

the response of the tubes in ZEPLIN III to an event situated on the central axis of the geometry. The histogram bars represent the response of the tube which is positioned at that point in the (x,y) plane. The response in each tube is normalised to the total number of photons collected over all the tubes. In comparison Fig 6.22 shows the response distribution of the tubes for an off-centre event. Qualitatively one can clearly see the variation in the photon distributions. In the analysis we set up the template files by simulating the response of our geometry to events in the gas over a predefined (x,y) matrix

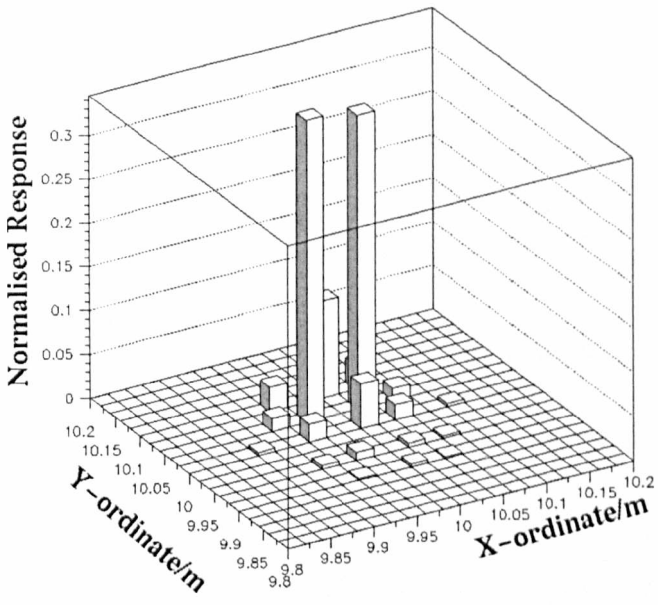


Fig. 6.22: Simulated normalised photomultiplier response for an off-centre event in ZEPLIN III.

of points. These files can be large and due to computational restrictions the matrix is limited to a 4mm mesh. We would expect the position uncertainty of the detector to increase with fewer photons detected. In order to test the worst case scenario - which we would expect to be the extraction of a single electron from the liquid - we run a simulation where this constraint is hardwired into the code. Essentially this will give us the lower limit on our spatial precision.

The comparison between the template files and event photomultiplier distributions is performed in the following way. Let us denote $R_n(x,y)$, the template response in number of photons detected in tube, n, at a position (x,y) in the gas. Also let us define $r_m(x_e,y_e)$ the integrated number of electroluminescence photons detected in tube, m, for an event that occurred at position (x_e,y_e) in the liquid. For the counts in the tubes from the simulated event we set:

$$f_{r_m} = \frac{r_m(x_e, y_e)}{\sum_{n=1}^{19} r_n(x_e, y_e)} \tag{6.9}$$

where f_{r_m} is the fractional response of tube, m. We now sum the total number of counts in the template distribution and multiply this with the measured

Mesh spacing in template	4mm
Number of photons per template node	5000
Specular reflectivities	0.9
Number of events simulated	10000
Field applied over electrodes	35kV
Tube quantum efficiency	20%
Monte Carlo step size in gas	0.5mm

Table 6.5: Table of Monte Carlo inputs.

event fractional distribution, ie:

$$S_{r_m} = f_{r_m} \sum_{n=1}^{19} R_n(x,y) \tag{6.10}$$

where S_{r_n} is the measured distribution normalised to the template counts, over tubes n. The χ^2 between these two distributions is then:

$$\chi^2 = \sum_{n=1}^{n=19} \frac{(S_{r_n} - R_n(x,y))^2}{R_n(x,y)} \tag{6.11}$$

This calculation is performed for all the template nodes. The best fit distribution is then the distribution which has the lowest χ^2 value. The position, (x,y), of the template node with the lowest χ^2 value is taken as the reconstructed position.

Results from Single Electron Extraction

Here we present results from a simulation where a number of events are created in the liquid. In each of these events a single electron is drifted and extracted according to the previously described procedure and electroluminescence light traced. After recording the photomultiplier response the χ^2 fitting procedure is performed. Table 6.5 lists some parameters of the simulation and the output. From the total of 10000 events simulated in this example, the total number of events giving rise to detected electroluminescence was 7577. Of the events that gave no detectable signal 1644 of those were events created in the RFR of the detector, resulting in no charge drift to the surface. A histogram of the radial positions of the remaining events which created no electroluminescence

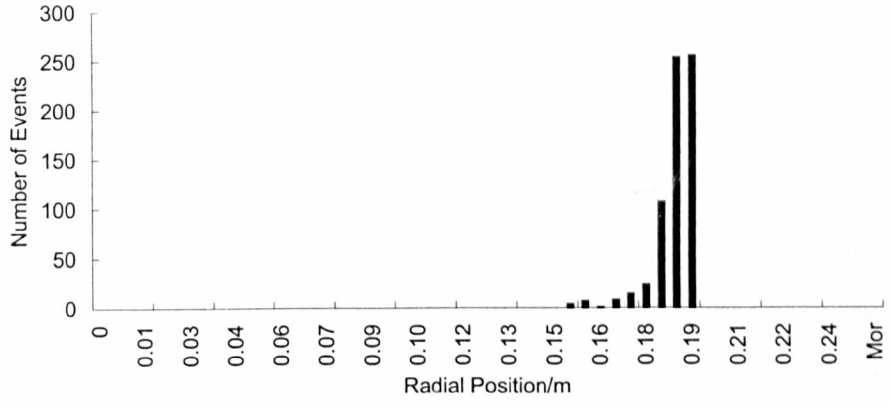


Fig. 6.23: A histogram of the radial positions of simulated single electron extraction from theliquid which gave no detectable electroluminescence. This plot excludes events from the RFR.

is shown in Fig 6.23. In Fig 6.23 we see that the effect of poor light collection at the edges of our detector is to suppress the ability to see single electron extraction events at these radial positions in the geometry. Turning to the reconstruction of events with these low extraction levels, Fig 6.24 shows the results of the χ^2-reduction on all the 10000 events. In this plot we choose to display the reconstructed x and y coordinates against the original event positions. This plot shows that our reconstruction algorithm is working even

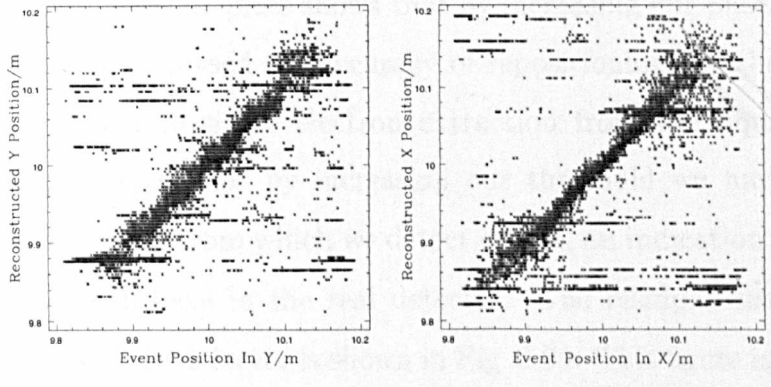


Fig. 6.24: Plots showing the reconstructed positions of all events for the x and y dimensions seperately.

at the single electron level. The correlation between the reconstructed and

original event position is clearly visible. However the horizontal lines present in the plots do suggest imperfect reconstruction. Many events originating randomly throughout our detector are being reconstructed at the same x or y value. This in itself suggests a lack of information, which we can associate with a low light collection effect. This hypothesis can be tested by limiting the reconstruction algorithm to events that result in a higher number of detected photons. This is analogous to triggering on larger signals in the detector. For comparison Fig 6.25 shows the same plots after we require the detection of at least ten photons in the photomultiplier array.

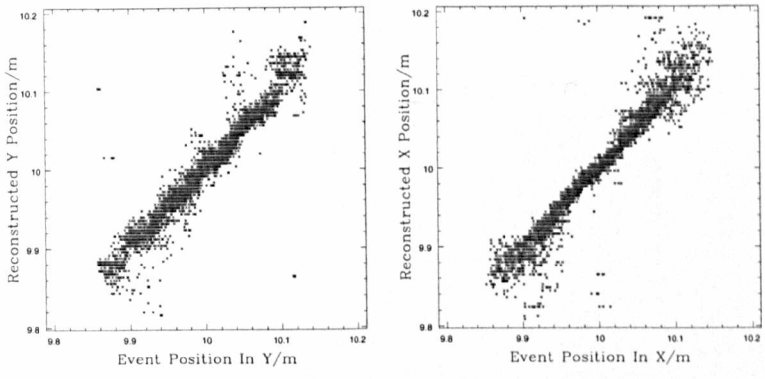


Fig. 6.25: Plots showing the reconstructed positions of events in x and y, with a lower limit of 10 photons detected in the photomultiplier tubes.

This second set of scatter plots shows that by increasing our photon detection threshold we have increased the accuracy of repositioning, for the case where we limit the model to single electron extraction from the liquid. Note in the simulation output that by increasing our threshold we have in essence constrained the radius from which we detect events, an indication of the power of selection we will have in the real detector. The residual distribution for different regions of the detector is shown in Fig 6.26. This figure is a plot of the accuracy of reconstruction for events within an annulus of width 20mm, that give a secondary signal. The accuracy is defined as the distance between the reconstructed position and the actual position of the event. Events are included in the different histograms if the original event position was within the given

annulus definition. The power of this projection is to enhance the argument for increased position accuracy for events towards the central axis of the detector. The width of the distribution falls as events are chosen closer to the central axis where light collection is more efficient. For the larger radial annuli (bottom left hand plots in the figure), we again notice the appearance of complications in the low light level χ^2 reduction technique that we have employed. Requiring high light detection thresholds removes these disparities, for example see Fig 6.27 & 6.28. The trade-off is between visible energy threshold and reconstruction efficiency.

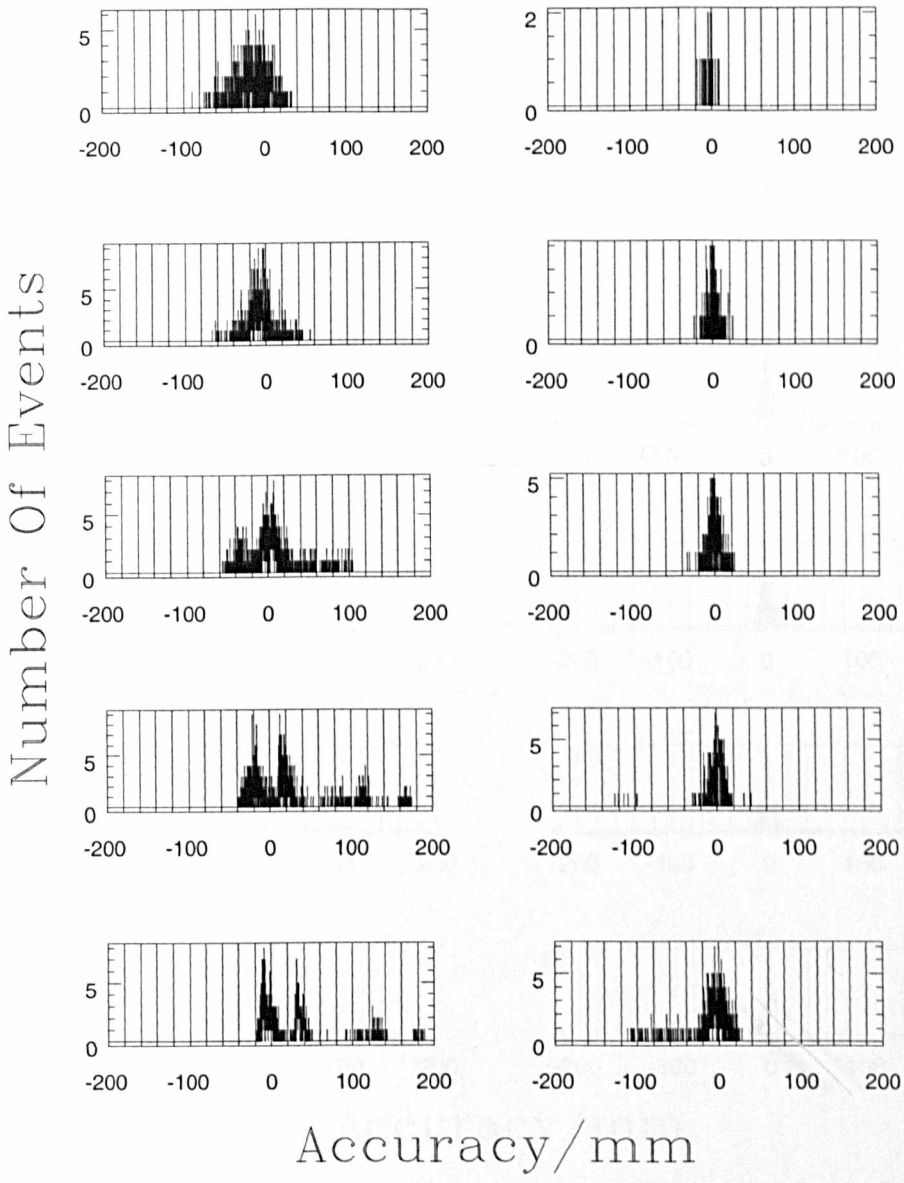


Fig. 6.26: Histograms of reconstructed position accuracy for different regions of the detector. Plots run from bottom to top starting on the left. Each plot is a selection of events from annuli of 20mm width of successively decreasing radii (194mm to 14mm). Accuracy is the measure of the difference of the actual event (x,y) position to the repositioned coordinates, in mm.

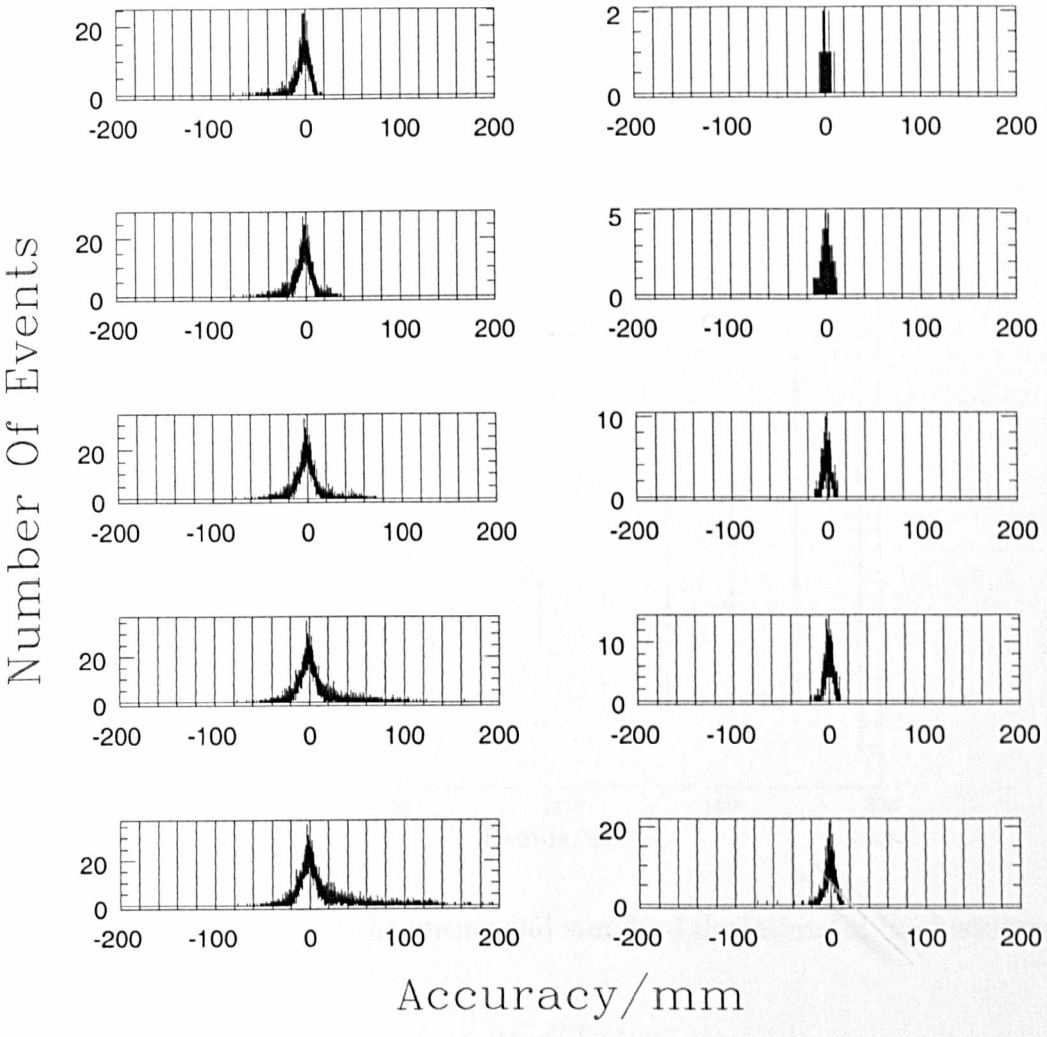


Fig. 6.27: Accuracy histograms for four electrons traversing the gas gap.

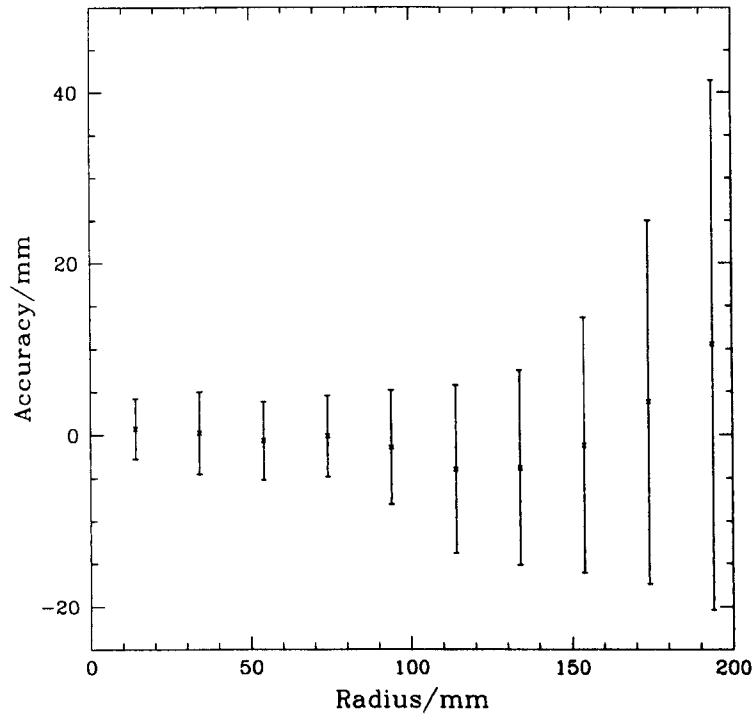


Fig. 6.28: Scatter plot of the means and standard deviations of the histograms from Fig 6.27.

6.4.3 Summary

In this chapter the main components of the Monte Carlo program have been detailed. Results from light collection and charge drift studies have been reported. The light collection efficiency of the ZEPLIN III geometry was found to be 33 ± 5% for events in the liquid volume. In the gas gap between the liquid surface and the mirror the average light collection was found to be 22 ± 16%. The electric field morphology in the ZEPLIN III detector was modelled using a finite element analysis program. The simulations gave a map of the electric field in two dimensions. Numerical approximations for electron drift velocities and electron yields for gamma-rays were introduced. The latter is used in the modelling of gamma-rays in the next chapter. A numerical approximation of the electron extraction probabililty was also given. The final part of this chapter examined the position reconstruction ability of the ZEPLIN III detector. To assess the worst case scenario, 10000 events were modelled for which only single electron extraction into the gas phase was assumed. Positions were reconstructed using the χ^2 reduction technique detailed in Section 6.4.2. Accuracy distributions were constructed for successive annuli in the detector. The distributions were found to be non-gaussian for events in the annuli outside a radius of 154mm. Within 154mm radius, the annuli cuts gave gaussian distributions. The widths of the gaussians decrease as events are selected nearer to the centre axis of the detector. This effect is probably due to the increased light collection efficiency. To investigate the effect of higher light levels, simulations were run for which four electrons were extracted into the gas phase. Results from these simulations indicated that the non-gaussianity in the single electron accuracy histograms was due to low light collection at the edge of the detector. The results from these simulations also suggested that events could be repositioned with sub-centimetre accuracy if they occurred within a radius of 144mm from the central axis of the detector.

CHAPTER 7

Background and Data Analysis Simulations

7.1 Introduction

In this chapter we examine the background expected in the ZEPLIN III detector. Photomultipliers are directly inserted into the liquid xenon volume in the detector. They have both ^{238}U and ^{40}K radioactive species and therefore generate the main background in the detector. Monte Carlo programs have been written to trace gamma-rays from the tubes interacting with the detector and Compton veto. Results from these have been input to the Light And Charge (LAC) code, and data for 0.23 days equivalent running has been produced. Data production uses code to produce expected photomultiplier responses to the recorded photon numbers and arrival times. The photomultiplier responses are then analysed to produce predicted electroluminescence/primary scintillation ratios. These plots demonstrate the discrimination of ZEPLIN III.

7.2 Gamma Ray Transport

7.2.1 Interaction Cross Sections

Uranium and potassium decays result in gamma-ray emission from low keV energies up to several MeV. Photons of this energy can interact with matter via the photoelectric effect, coherent scattering, Compton scattering and pair production. In our analysis we include all of these processes except the coherent scattering. Coherent scattering will not deposit energy in the target, and will therefore not lead to detectable signals and so, to simplify the coding, this can be ignored. Interaction cross sections for the other processes were obtained from the NIST photon cross sections database available at [122], an example of which is shown in Fig 7.1. This shows the cross sections for gamma interactions with a xenon atom. Additionally for our gamma-ray transport code we need to incorporate the angular dependence of the Compton scattering process. This is given by the differential form of the Klein-Nishina formula, based on the original work [123]:

$$\frac{d\sigma}{d\Omega} = \frac{r_o^2}{2\left(1+\gamma\left(1+\cos\theta\right)\right)^2}\left[1+\cos^2\theta+\frac{\gamma^2\left(1-\cos\theta\right)^2}{1+\gamma\left(1-\cos\theta\right)}\right] \quad (7.1)$$

where $d\sigma/d\Omega$ is the differential cross section for a scattering event into an angle θ, r_o is the classical electron radius ($2.817\text{x}10^{-15}$m), γ=hν/$m_e c^2$, h is Planck's constant, ν the frequency of the gamma-ray, m_e the mass of an electron and c is the speed of light in a vacuum.

Look-up tables for all the elements present in our detector were created from the NIST database. Without discussing the geometry too thoroughly here, for this modelling it was deemed sufficient to include large mass parts of the detector. To this end the elements for which we required data were: nitrogen, oxygen, xenon, copper, iron and hydrogen. These elements make up the majority of the scattering material in the detector.

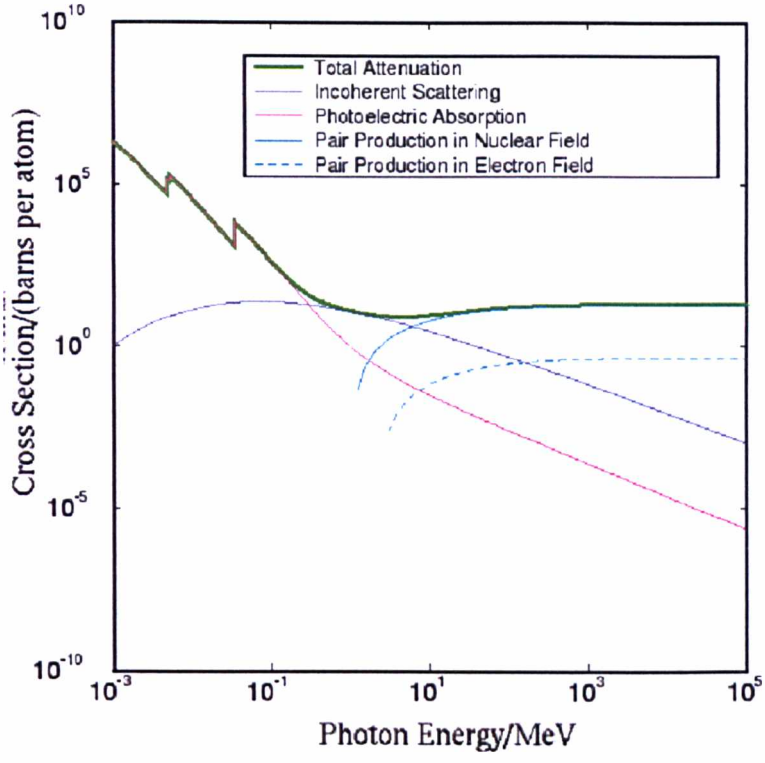


Fig. 7.1: Cross sections for gamma-ray interactions with xenon (Z=54) included are: photoelectric absorption, incoherent (Compton) scattering and pair production processes.

7.2.2 Gamma Simulation Code Structure

A box diagram of the complete gamma interaction code is shown in Fig 7.2. This will aid our discussion of the code.

A :

This box sets the initial properties of the gamma-ray to be transported. There are three considerations here. Firstly line spectra of both the ^{238}U and ^{40}K are used to give probabilities of emission of gamma-rays of a certain energy, see Fig 7.3. ^{40}K has a single gamma decay of energy 1.46 MeV. Secondly we select the initial trajectory of the gamma in the frame of the detector at random over the sphere of 4π radians. Its speed is c.

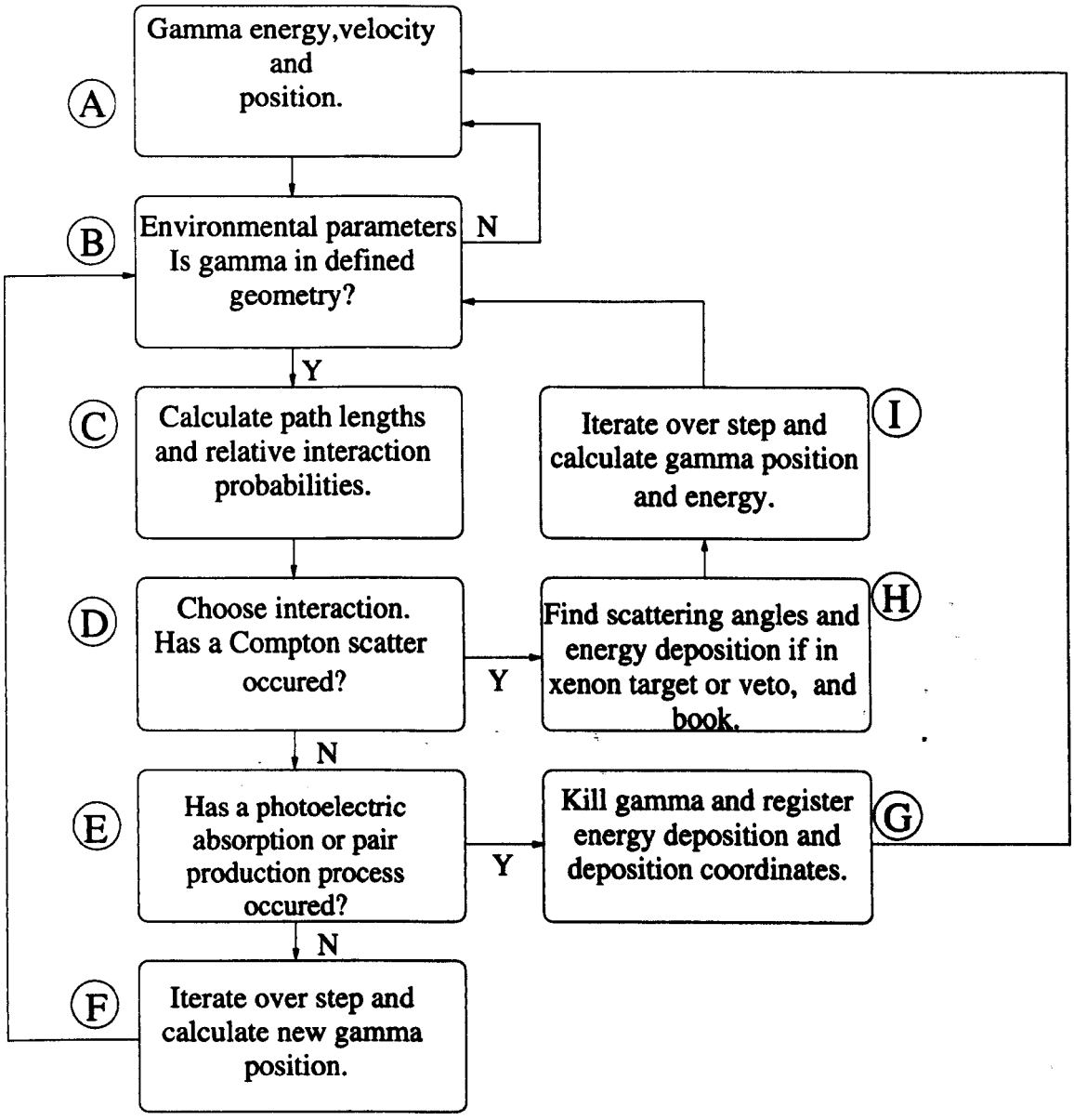


Fig. 7.2: Box diagram for gamma-ray interaction code developed for investigation of gamma-ray background from photomultiplier tubes. Circled letters are labels for each box, Y indicates true (1) logic and N indicates false (0) logic.

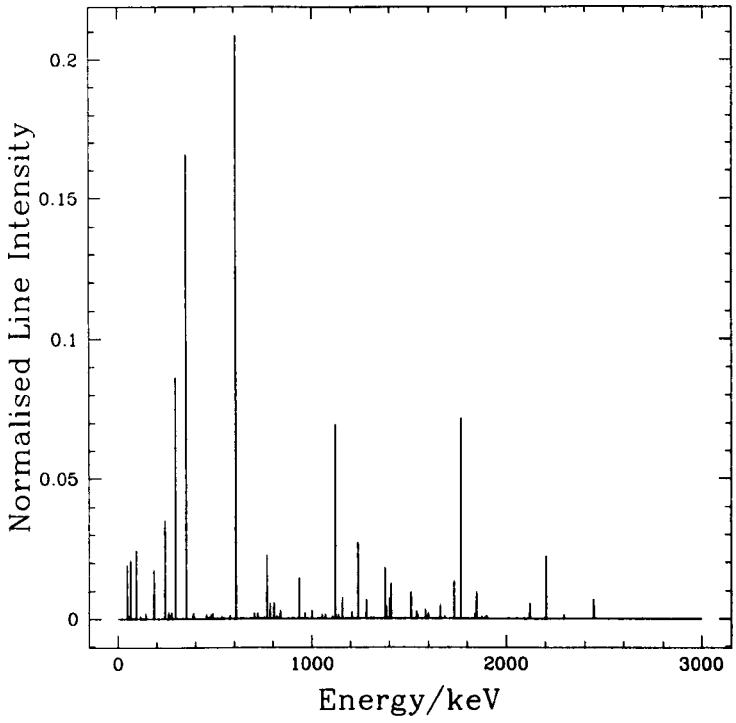


Fig. 7.3: Line spectrum used as input to ^{238}U background simulation. Data from [117].

Finally we randomly produce the gamma-ray's position of emission. The centre of the frame of reference for the system, for compatability with the LAC code, is chosen to be (10,10,10). Emission from the photomultipliers is localised to the position of the graded seal which constitutes the highly radio-impure component of the photomultiplier. According to the manufacturers this seal is located approximately at the half point of the tube length. Therefore, in the simulation, source positions are limited to a ring around the tube at this position.

B :

Geometric and material definitions are considered. The position of the gamma-ray is compared to defined volumes. A volume is identified together with its material content. Material parameters are then passed to box C. For the elements they are atomic number Z, density ρ and atomic

molar mass, M_a. If the material is a mixture or a compound, either air or the veto liquid scintillator (Phenoxyloethane (PXE)), then the elemental weight fractions are passed in parallel with the elemental properties. If the gamma-ray has exited from the geometry the code returns to box A.

C :

This unit has two parts. For an elemental material, for example copper, cross section data for all modelled processes are obtained from the NIST look-up tables. The total cross section for any interaction to occur is the sum of the individual components:

$$\sigma_{tot} = \sigma_{\phi} + \sigma_{C} + \sigma_{pn} + \sigma_{pe} \tag{7.2}$$

where σ_{tot} is total cross section, σ_{ϕ} photoelectric absorption cross section, σ_C Compton scattering cross section, σ_{pn} pair production in nuclear field cross section and σ_{pe} pair production in the orbital electron field cross section. This box calculates all the probabilities associated with the four interaction cross sections according to:

$$\begin{aligned} P(\sigma) &= 1 - e^{-n\sigma dx} \\ n &= \frac{\rho N_a}{M_a} \end{aligned} \tag{7.3}$$

where $P(\sigma)$ is the probability of interaction for a process with cross section σ, n is the atomic number density, dx is the path length through the material and N_A is Avagadro's constant.

D :

This box decides which of these processes occurs, based on the probabilites given by box C. Random numbers are compared with each probability and if this number is below the given probability then the interaction is deemed to have occured. It is possible for more than one

interaction to be chosen in this way. If this occurs we simply choose randomly between each of the possible interactions. If Compton scattering is chosen then the code goes to box H.

E :

Here the code decides, given the information from box D, whether to book an energy deposition or to continue the passage of the photon through the geometry.

F :

No interaction has taken place so the gamma-ray is transported to its new position, simply by taking its initial direction vector and iterating over one step length in the Monte Carlo.

G :

One of the following processes has occurred: photoelectric absorption, pair production in the nuclear field or pair production in the electric field. The gamma-ray is killed and its position and energy deposition registered. No secondary effects from these processes are considered.

H :

A Compton scatter has occurred. This box calculates the angle of deflection relative to the normal of the incident gamma-ray. Sampling is performed on the normalised probability density function for Compton scatters, which is the step-wise integral of Equ 7.1 normalised to the total cross section for a Compton scatter. A random number is chosen and an angle of scatter selected accordingly. The latitudal angle of scatter in the frame of the scattered gamma-ray is chosen randomly over 2π.

I :

The new position of the gamma-ray is calculated either by using deflection angles set as a result of a Compton scatter, or else the gamma-ray is simply iterated over the step, as in box F.

7.2.3 Geometry and Material Parameters

In the code we set up a description of the ZEPLIN III geometry and materials. Referring to the detailed geometry in Fig 5.9, the detail is deconstructed into the dominant volumes of interest. These include:

- the veto volume, modelled as a cylinder supporting a hemispherical dome. 3mm stainless steel walls and filled with PXE liquid scintillator.
- the air gap. This is the volume between the outer surface of ZEPLIN III and the inner surface of the veto.
- the vacuum shell of ZEPLIN III modelled as 3mm thick cylindrical shell, with supporting disc. Constructed from copper.
- inner ZEPLIN III shell modelled as 3mm thick cylindrical shell, with supporting disc. Constructed from copper.
- dynode discs modelled as 20mm thick copper disc.
- photomultiplier emf screen, modelled as two cylindrical copper parts.
- electrodes and mirror: two cylinders and a disc both constructed of copper.
- gaseous xenon which fills all internal volume above defined liquid level.
- liquid xenon which fills all internal volume below defined liquid level.

Table 7.1 gives the explicit placing and dimensions of each defined volume in the simulation. Fig 7.4 is a sketch of the veto geometry.

It should be noted that the air gap, liquid xenon and gas xenon volumes are not defined explicitly. Instead they are inferred from other volumes. In the code logical operators are used to define these volumes.

The materials defined in the geometry definition are copper, air, PXE, iron, vacuum, liquid xenon and gaseous xenon. The properties used for the elements

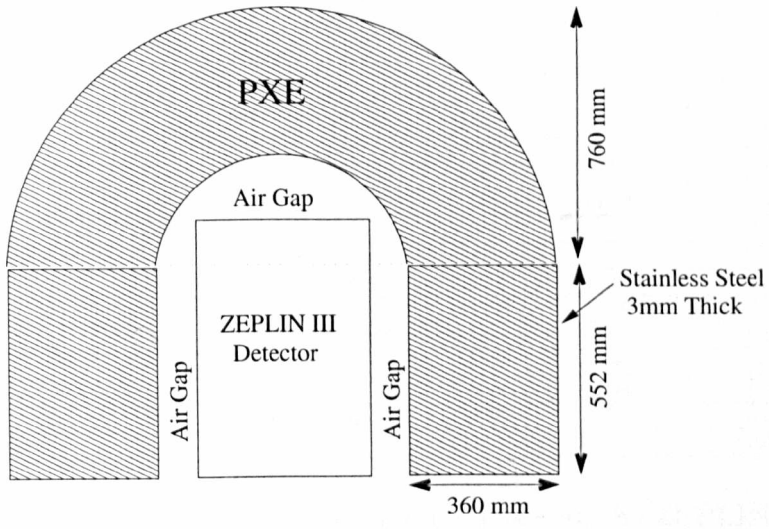


Fig. 7.4: Sketch of the veto and ZEPLIN III detector arrangement.

in the Monte Carlo are given in Table 7.2. Note that stainless steel is assumed to contain only iron atoms.

Air and the veto scintillator are also modelled. The veto scintillator is treated as a homogenous mixture of carbon and hydrogen atoms. In general for a material consisting of two atoms A and B we define their number density ratios n_A and n_B. If we are considering an interaction for which each component atom has a cross section σ_A and σ_B, then the total cross section of the mixture is $\mathrm{n}_A\sigma_A + \mathrm{n}_B\sigma_B$. A probability can then be assigned for an interaction over a defined path lengh in that mixture. If a random number is produced that is less than, or equal to, this probability then an interaction occurs. The atom which is considered to have resulted in that interaction is chosen on the basis of the relative number densities of each component. The physical properties of that atom are used for the later calculations. Table 7.3 details the information that is used in the Monte Carlo in this procedure.

With the definitions of the geometry, materials and the tracking code complete, the simulation is now in a position to determine the background effects from the tubes. In the next section we discuss some tests of the code and further explore some of the mechanisms used.

Volume	Shape	Centre	Height	Inner Radius	Outer Radius	Material
Veto	Cylinder	(10,10,9.374)	0.552	0.400	0.760	PXE and Steel
Veto	Hemisphere Shell	(10,10,9.926)	-	0.400	0.760	PXE and Steel
Vacuum Shell	Disc	(10,10,9,374)	0.030	-	0.380	Copper
Vacuum Shell	Cylinder	(10,10,9.404)	0.82	0.350	0.353	Copper
Vacuum Shell	Disc	(10,10,10.221)	0.003	-	0.353	Copper
Target Shell	Disc	(10,10,9.767)	0.06	-	0.319	Copper
Target Shell	Cylinder	(10,10,9.827)	0.360	0.239	0.242	Copper
Target Shell	Disc	(10,10,10.184)	0.003	-	0.242	Copper
Copper Dynode	Disc	(10,10,9.830)	0.02	-	0.185	Copper
PMT Screen	Cylinder	(10,10,9.827)	0.224	0.217	0.242	Copper
PMT Screen	Cylinder	(10,10,9.827)	0.174	0.130	0.217	Copper
PMT Vacuum	Disc	(10,10,9,874)	0.126	-	0.130	Vacuum
Electrode	Cylinder	(10,10,10)	0.025	0.194	0.209	Copper
Electrode	Cylinder	(10,10,10.029)	0.018	0.194	0.209	Copper
Mirror	Disc	(10,10,10.047)	0.007	-	0.209	Copper
Active Volume	Disc	(10,10,10)	0.042	-	0.194	Liquid Xenon

Table 7.1: Table of the volumes and materials used in the ZEPLIN III gamma-ray code.

Element	Atomic Number	Molar Mass (kg mole^{-1})	Density (g cm^{-3})
Copper	29	0.0635	8.92
Xenon (lq)	54	0.13102	3.052†
Xenon (g)	54	0.13102	5.8×10^{-3}
Stainless Steel	26	0.0559	7.7

Table 7.2: Table of the elemental parameters used in the ZEPLIN III gamma-ray code. Data taken from [124, ?].

7.2.4 Diagnostic Testing and Limitations

Each subroutine used in the program was developed and tested individually. Confirmation of correct data input from the NIST database was achieved. To test the calculations of interaction probabilities, gamma-rays of known energy were created at known positions. The cross sections and probabilities were output and checked against calculated predictions. In all materials, results from this test verified that the subroutines used in these calculations were operating correctly. The production of the integral probability distribution function for the differential Compton cross section was also tested. The results for five decades of energies between 1keV and 10MeV are displayed in Fig 7.5. Multiple points in these distributions were compared with calculations prepared analytically. In all cases the subroutines produced correct results

Mixture	Atomic Number A	Atomic Number B	n_A (atoms m^{-3})	n_B (atoms m^{-3})
PXE(Veto)	12	1	6.8×10^{28}	3.89×10^{28}
Air	7	8	2.10×10^{25}	5.91×10^{24}

Table 7.3: Table giving the physical preoperties of mixtures used in the ZEPLIN III gama-ray code. Data for PXE from [125]. Calculations for air assume ideal mixture of atomic oxygen and nitrogen at standard room temperature and pressure.

with insignificant errors. To check the initial properties of the gamma-ray to be simulated, a dummy input spectrum and source position model was run. The aim was to reproduce the input ^{238}U spectrum and record the position of emission. Two plots are shown to verify the input production. Fig 7.6 is the plot of the energy spectrum of initial gamma ray energies, and Fig 7.7 is the spatial distribution of sources in the (x,y) plane. The results shown are for a run comprising more than 270000 events. Fig 7.6 can be seen to reflect the true ^{238}U spectrum shown in Fig 7.3 to within much less than one per cent. Additionally, Fig 7.7 indicates that gamma-rays are produced from the correct positions.

A significant ingredient in the gamma-ray code is the registering of energy deposition after a scattering event. In this scenario, if a scatter takes place and the angle of deflection is θ, then the energy deposited is calculated by:

$$\begin{aligned} h\nu' &= \frac{h\nu}{1+\gamma(1-\cos\theta)} \\ D &= h\nu - h\nu' \end{aligned} \tag{7.4}$$

where $h\nu'$ is the energy of the scattered photon, $h\nu$ the energy of the incident photon and γ is as previously defined. D is the energy deposition in the material. Fig 7.8 is a plot showing the variation of the ratio $h\nu'/h\nu$ as a function of scattering angle for an incident photon energy of 500keV. This figure indicates the Compton energy deposition routine is functioning correctly.

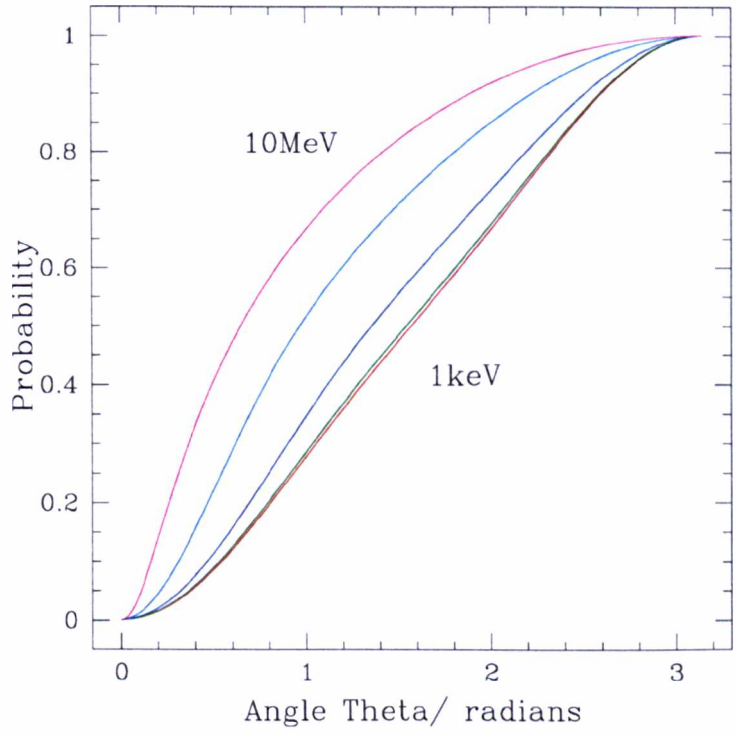


Fig. 7.5: The integrated probability distribution functions for 1keV, 10keV, 100keV, 1MeV and 10MeV incident gamma-ray energies. The energies increase from left to right on the plot. Theta is the angle of scatter for the scattered gamma-ray, relative to the incident gamma-ray.

The problem of transporting the photons through the defined geometry was solved by using three dimensional transformation matrices. For a particular photon, it is necessary to record the history of interactions and their respective θ, ϕ deflection angles. This enables direction vectors and position coordinates to be related between the photon and detector frames of reference. To illustrate this, assume that a photon undergoes a Compton scatter, resulting in deflections θ_1, ϕ_1. Denote the initial direction vector of the photon in the detector frame (**i**,**j**,**k**). The direction vector of the photon after scattering is then given by Equ 7.5.

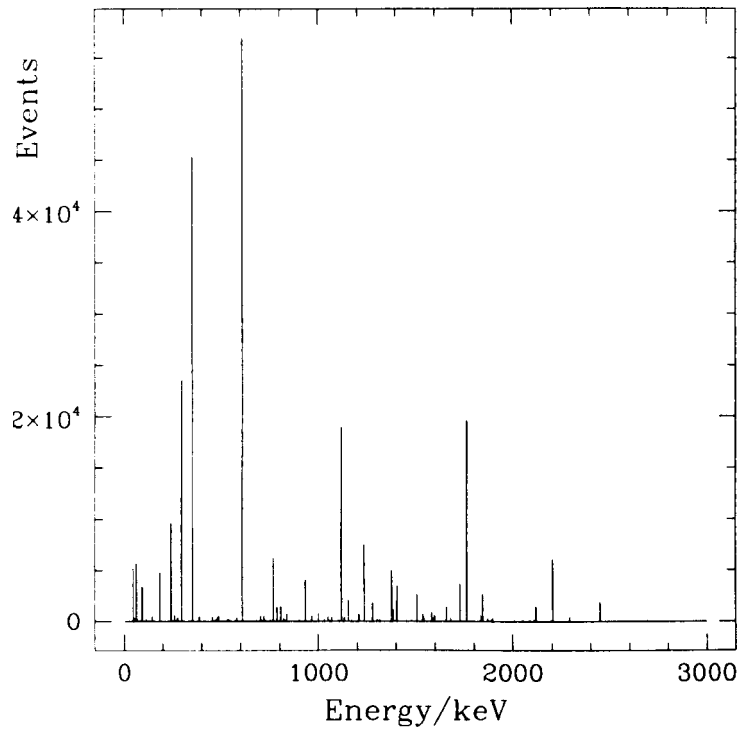


Fig. 7.6: Simulated input energy spectrum of > 273000 gamma events from ^{238}U contamination.

$$\begin{pmatrix} 1 & 0 & 0 \\ 0 & \cos\phi_1 & \sin\phi_1 \\ 0 & -\sin\phi_1 & \cos\phi_1 \end{pmatrix} \begin{pmatrix} \cos\theta_1 & 0 & \sin\theta_1 \\ 0 & 1 & 0 \\ -\sin\theta_1 & 0 & \cos\theta_1 \end{pmatrix} \begin{pmatrix} \mathbf{i} \\ \mathbf{j} \\ \mathbf{k} \end{pmatrix} = \begin{pmatrix} \mathbf{i}_f \\ \mathbf{j}_f \\ \mathbf{k}_f \end{pmatrix} \quad (7.5)$$

Now the scattered photon undergoes a second Compton scatter with deflection angles θ_2, ϕ_2. The final direction vector of the photon in the detector frame is now given by Equ 7.6.

$$\begin{pmatrix} 1 & 0 & 0 \\ 0 & \cos\phi_2 & \sin\phi_2 \\ 0 & -\sin\phi_2 & \cos\phi_2 \end{pmatrix} \begin{pmatrix} \cos\theta_2 & 0 & \sin\theta_2 \\ 0 & 1 & 0 \\ -\sin\theta_2 & 0 & \cos\theta_2 \end{pmatrix} \begin{pmatrix} \mathbf{i}_f \\ \mathbf{j}_f \\ \mathbf{k}_f \end{pmatrix} = \begin{pmatrix} \mathbf{i}_{ff} \\ \mathbf{j}_{ff} \\ \mathbf{k}_{ff} \end{pmatrix} \quad (7.6)$$

Multiple scattering events are expected to be frequent (see later discussion), so the abililty of the code to cope with these occurences was implicit in the problem. The matrix transformations were investigated thoroughly by hard-coding,

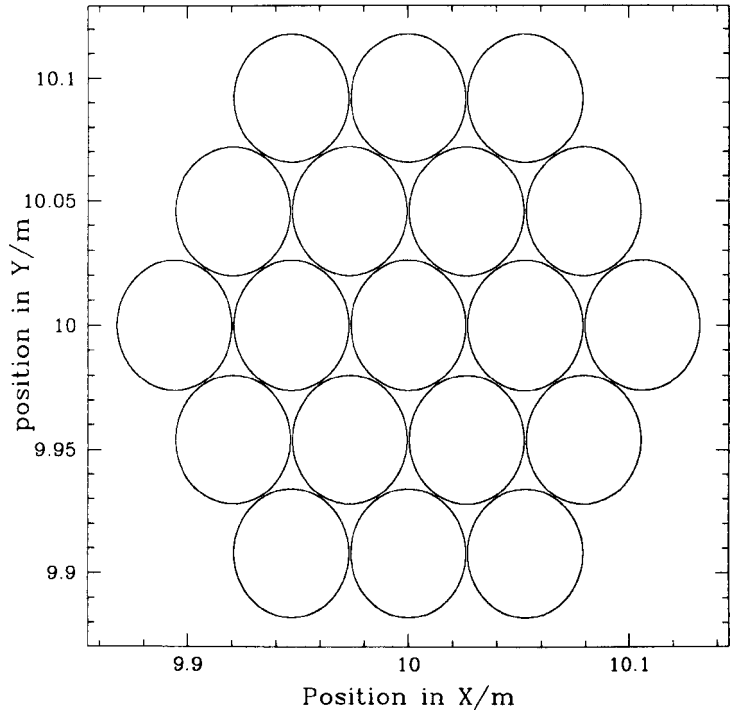


Fig. 7.7: Simulated starting positions for gamma-rays in photomultiplier tubes.

in particular, angles of deflection and comparing these to pre-determined expected results. The code performed well and gave insignificant errors in these cases.

After establishing that all components of the code were operating correctly the suite was in a form suitable for some more integral tests. Figures 7.9 & 7.10 represent test gamma-rays produced with initial vertical velocities. The four sets of plots (two in each figure) are for photon energies, 10keV, 100keV, 1MeV and 10MeV. These figures represent the passage of photons through liquid xenon. From these plots it is deduced directly that the range of photons through liquid xenon increases with increasing gamma energy, as expected. It is also noted that as the initial energy of the photon increases above 10keV the likelihood of Compton scattering increases. This can be observed by the traces becoming more complex due to increased scatterings. Low energy photons only travel a small distance before becoming photoelectrically absorbed. As hinted

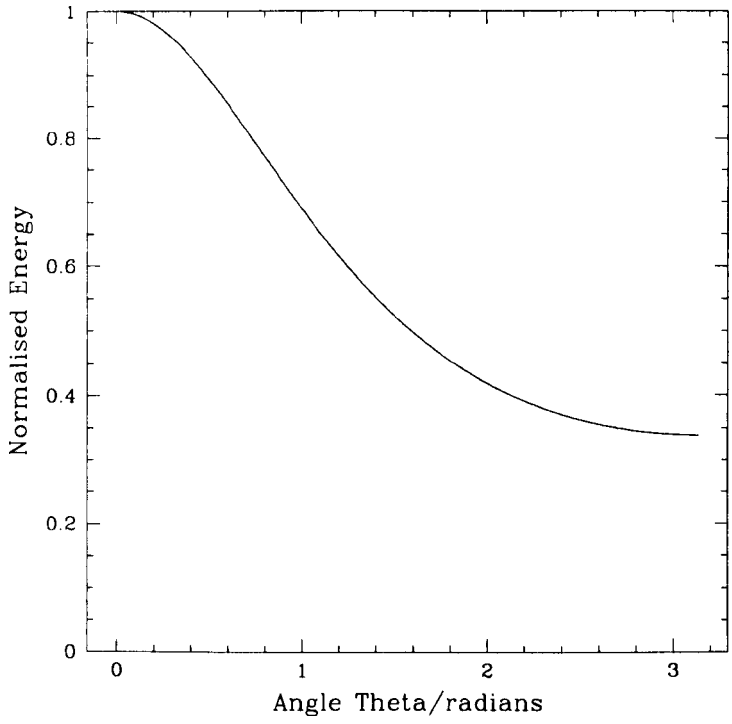


Fig. 7.8: Output plot showing the variation of the ratio of the Compton gamma-ray energy to incident gamma-ray energy (500keV), as a function of the deflection angle θ.

earlier, multiple scattering of photons becomes evident in the 1MeV simulated data. At the highest energy, 10MeV, photons are seen to pass through a significant thickness of liquid xenon without much interaction. To check more quantitatively the ranges of the photons, which the simulations produced, the plots are compared to the absorption lengths given by Table 7.4. Both sets of information, the theoretically predicted absorbtion lengths and the Monte Carlo traces, are in agreement.

Code Limitations

In the description of the code, the concept of secondary effects arising from the primary process being simulated were mentioned. The code, for example, simply registers an energy deposit (equal to that of the gamma-ray involved) and the position when either a photoelectric absorption or one of the

Initial Photon Energy/keV	Absorption Length
10	20μm
100	1.7mm
1000	5.8cm
10000	8.2cm

Table 7.4: Table of absorption lengths for gamma-rays of given energy in liquid xenon.

pair-production processes occurs. Also the electron resulting from a Compton scatter is not transported. The issue to tackle is whether these oversights lead to gross errors in the simulation of positioning of events. The considerations here are the same as those mentioned in Section 6.3. Is there a process which will result in light emitted from a point far from the initial interaction point? Again it can be asserted that any large deviation of the light source from the initial interaction point must have resulted from a process involving a high energy, which in the detector would be easily recognisable by the large signal. Fig 6.14 shows that electrons even with energies of a few hundred keV have expected path lengths of only a few hundred μm.

In the photoelectric effect a simple ionisation and recombination scenario has been assumed. A more accurate investigation into this effect would have to include K-shell effects. The increase in the photoelectric cross section used in the code incorporates the effect of the K and L atomic electron - the cross section is raised at the calculated energies for which the cross section for absorption by electrons in these shells increases. However, the code does not follow the subsequently emitted x-ray after the filling of the K-shell vacancy from an electron in a higher orbital shell. For this limitation, it is assumed that the distance travelled before this x-ray is reabsorbed by the material is negligible compared with the concerned scales of interaction. For the pair production processes, the omitted physics from the code is concerned with high energies. The complexities of high energy photons producing pair production and *bremsstrahlung* emission by electrons, combining to form electron-photon

showers, can also be ignored due to the high energies required, which would make this phenomenon easily distinguishable, and of no concern for a dark matter detector.

In practice the code is simple to use. A new user would require a few hours of tutoring, and currently the code is maximised to perform the problem described. Minor alterations, in the geometry and cross section reference data, could increase the scope of the code's application. There are more complete software suites available, for example the GEANT series of codes, and these were considered for this application. These codes are extremely complex and opaque to the user. Therefore, whilst containing less physics, this handwritten code has performed excellently for the understanding of this problem. The results will contain errors due to some broad assumptions made in the secondary physics processses but, as examined, these should not contribute significantly to the energy region of interest.

7.3 ^{238}U and ^{40}K Background

Results from the described code are presented. The predicted energy spectrum arising from gamma interactions in the xenon target is reported. Effects of the RFR and veto in reducing the event rate are examined.

The results presented are for a total of 4.85×10^5decays. In the following the running time of the detector to which this corresponds is calculated. Table 7.5 below gives the details of the radioactive contamination of the components inside the 9829QA photomultiplier. Numbers within brackets are quoted errors.

The intensity of the gamma-rays from ^{238}U is calculated to be 3.13×10^3 kg^{-1} day^{-1} ppb^{-1} [126]. The ^{40}K rate is calculated to be 0.00331 Bq kg^{-1} ppm^{-1} [127]. The estimate of the number of gammas expected from all 19 tubes in one days running is 1.45×10^6 from ^{238}U and 0.72×10^6 due to ^{40}K. This ratio

Material	Description	Mass/gm	Potassium conc./ppm	Uranium conc./ppb
Glass	Window	4	5(1)	8(1)
Glass	Front Tubing	16	54(10)	77(4)
Glass	Graded Seals	14	7200(100)	420(50)
Glass	Rear Tubing	18	300(10)	100(40)
Glass	Base	13	1400(20)	1100(30)
Ceramics	Sideplates	20	200(70)	50(20)
Ceramics	Rods	5	30(20)	20(10)
Internal Generators	Potassium	0.1	25000(2800)	0(0)

Table 7.5: Table showing the contributions to the radioactivity levels in photomultipliers from constituent materials.

is preserved in the radioactive modelling. Hence, from the overall number of generated events, this data-set represents a real time of 5.4 hours.

7.3.1 Deposited Energy Spectra

The gamma-ray code produces list output which details: energy depositions in the liquid xenon target, the position of the deposition, the process that leads to that deposition and, finally, whether the gamma-ray that produced the deposition is 'seen' in the Compton veto. In Fig 7.11 the energy depositions in the fiducial volume are shown. Note that the plot at this time does not integrate multiple events for a single gamma-ray. In considering multiple events for a single photon, it must be realised that scintillation from these events is emitted coincidentally, due to the lengths involved in our detector. Therefore, multiple energy depositions for a single photon should be summed as this represents more comprehensibly the deposited energy for that photon. The energy spectrum after multiple events have been integrated is shown in Fig 7.12. The effect of this summation on the spectrum is to reduce the number of low energy depositions and single line intensities are increased. This indicates that within the liquid xenon a substantial number of the photons are completely absorbed.

The spectra presented have several features worthy of comment. At low energies the spectrum is a featureless exponential. At higher energies near 300keV there is a peak. At an energy near 1.2MeV a sharp edge in the spectrum is

observed. The statistical fluctuations in the plots are magnified during progression to higher energies - this is a facet of the low number of high energy events in the data-set and the 1keV binning being too fine for high energies. The peak at 300 keV is attributed to backscattered photons which have Compton scattered off material before entering the liquid xenon volume. The final feature observed is interpreted as the Compton edge to the 1.46 MeV potassium background, which theoretically should occur at 1.24MeV. This concurrs with the position indicated by the spectrum. Taking the spectrum in Fig 7.12 as the fundamental energy deposition spectrum, it is possible to place an upper limit on the contribution to the count rate in our detector. Taking the volume of target to be 4.97×10^{-3} m^3 gives a target mass of 15.2 kg. Integrating the counts between 0 - 10keV renders a total count of 727 from the simulated data. Therefore the estimate of the background count rate without discrimination, active vetoing and fiducial cuts is 21.3 dru between 0 - 10keV. Assuming a $\sqrt{N}$ error on each keV bin in the simulation renders an error estimate of ± 0.8 dru.

The effect of the veto can be observed in Fig 7.13, where events that have scattered in the veto and deposited a detectable energy (assumed to be in excess of 30keV), have been removed from the spectrum. With the veto, the integrated number of counts between 0 - 10keV is now 561. This reduces the background count rate in this range to 16.4 dru. The final estimation on the background rate must also account for the effect of the RVR. Performing a position cut on the deposition data, such that events which result in deposits in this 7mm layer of xenon are removed, renders a final estimate on the background rate of 9.2 dru. Errors in the given rate calculations are estimated to be negligible. The figures apply for liquid xenon with a density ρ=3.052 gmcm^{-3}, which applies at T=170K. Fig 7.14 shows the low energy spectrum (between 0-50keV) after all of the above factors are included.

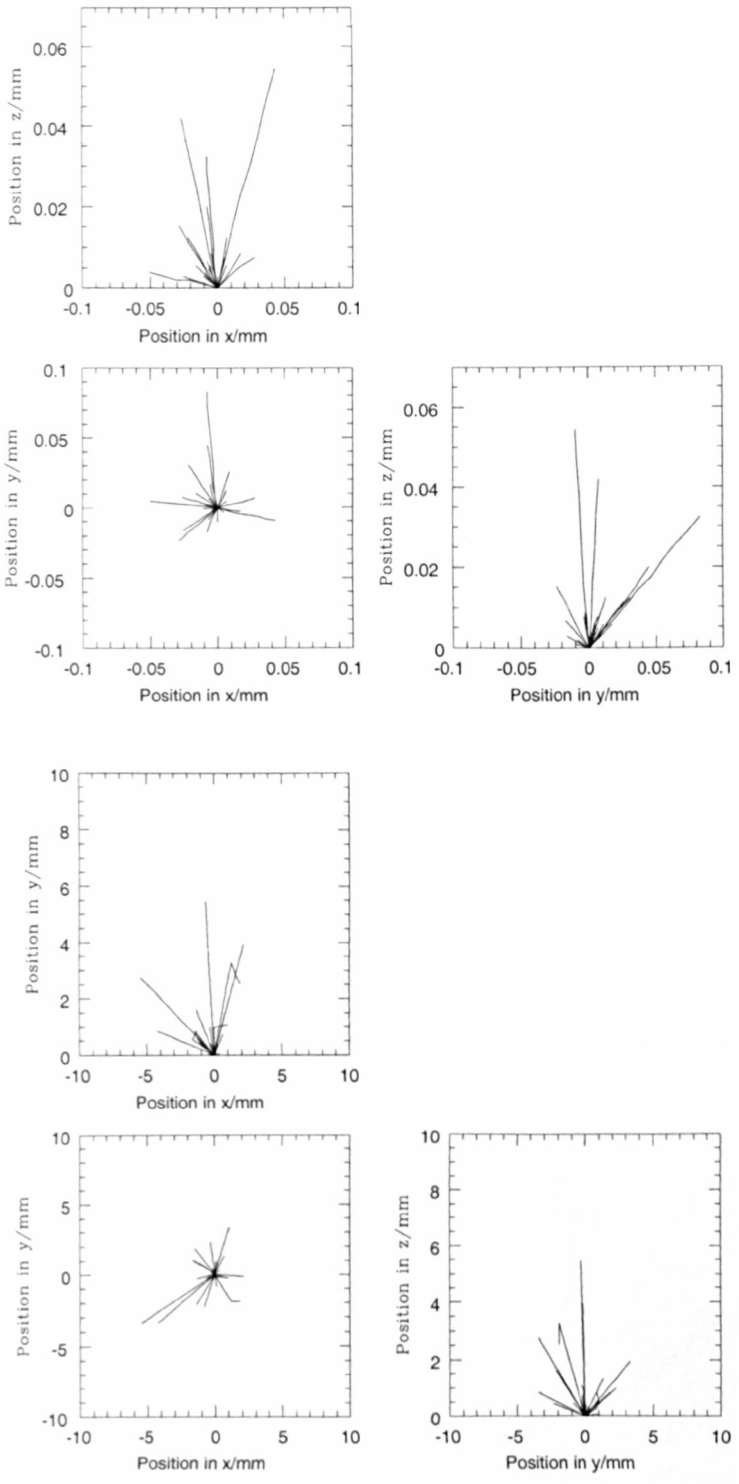


Fig. 7.9: Simulated gamma-ray paths for initial photon energies of 10keV (top set of three plots) and 100keV (bottom set of three plots).

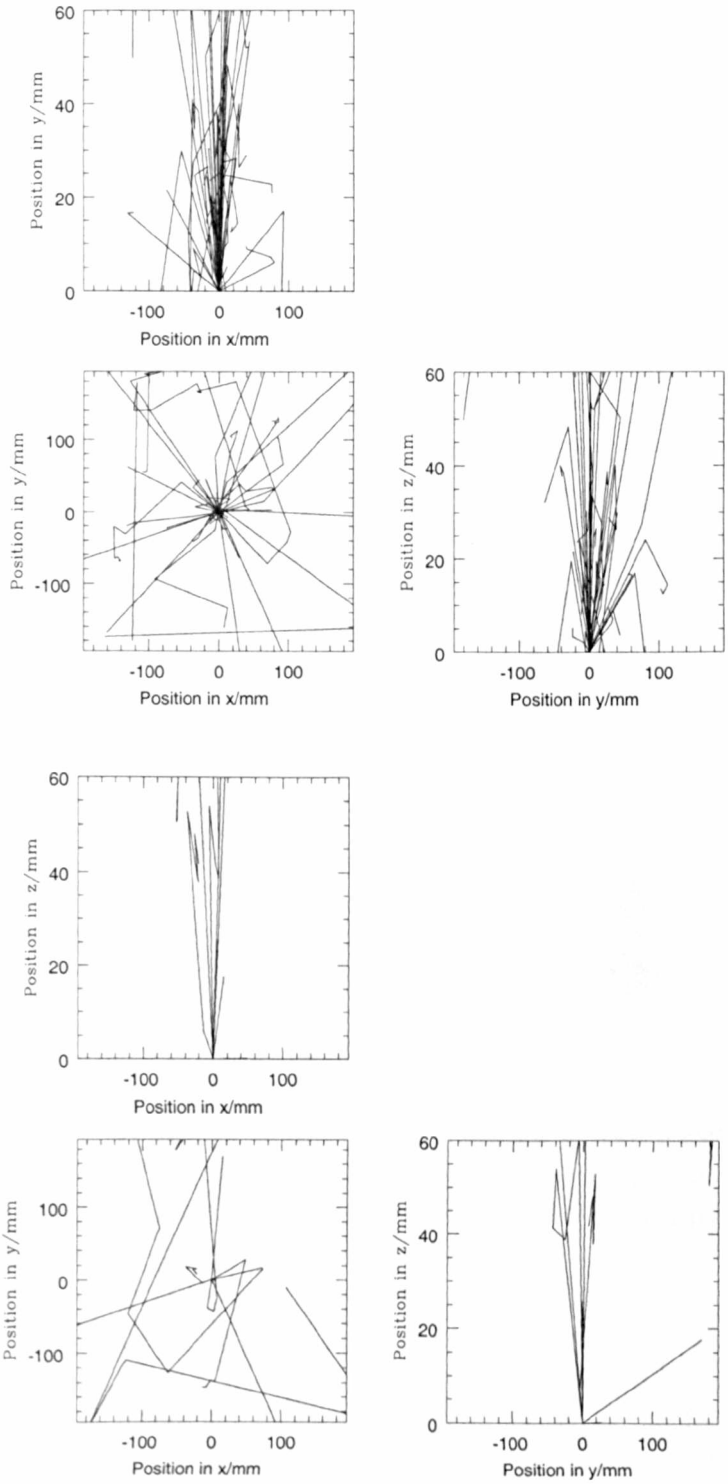


Fig. 7.10: Simulated gamma-ray paths for initial photon energies of 1MeV (top set of three plots) and 10MeV (bottom set of three plots).

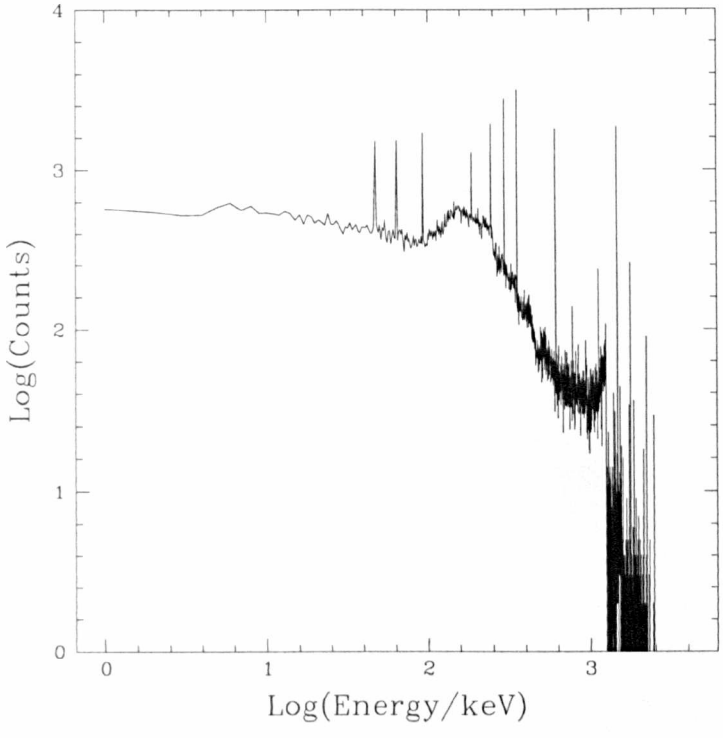


Fig. 7.11: Simulated energy depositons for events in the whole liquid xenon volume arising from ^{238}U and ^{40}K decays in the photomultiplier quartz. The energy deposition is the real energy deposited, multiple depositions for a single photon are treated as single events.

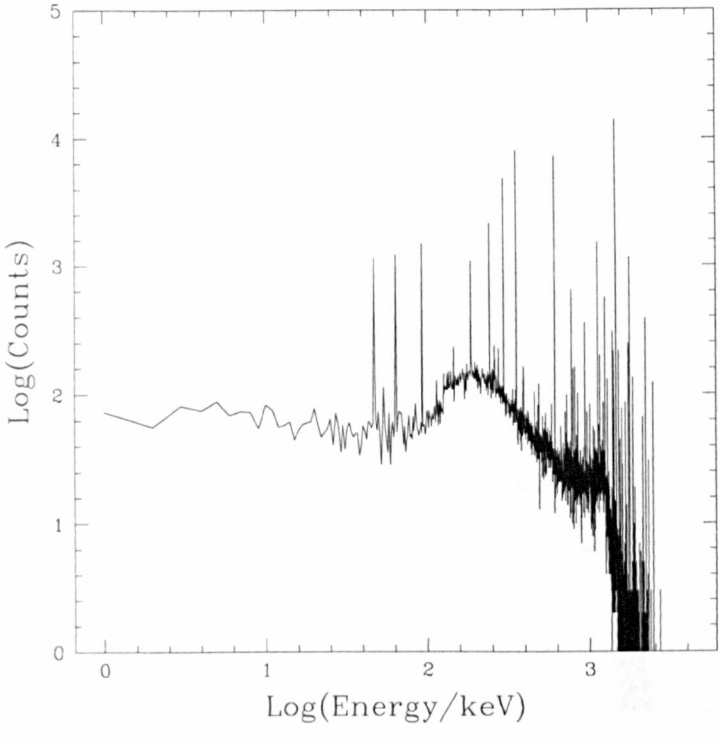


Fig. 7.12: Simulated energy depositons for events in the whole liquid xenon volume arising from ^{238}U and ^{40}K decays in the photomultiplier quartz. The energy deposition is the real energy deposited, multiple depositions for a single photon are integrated.

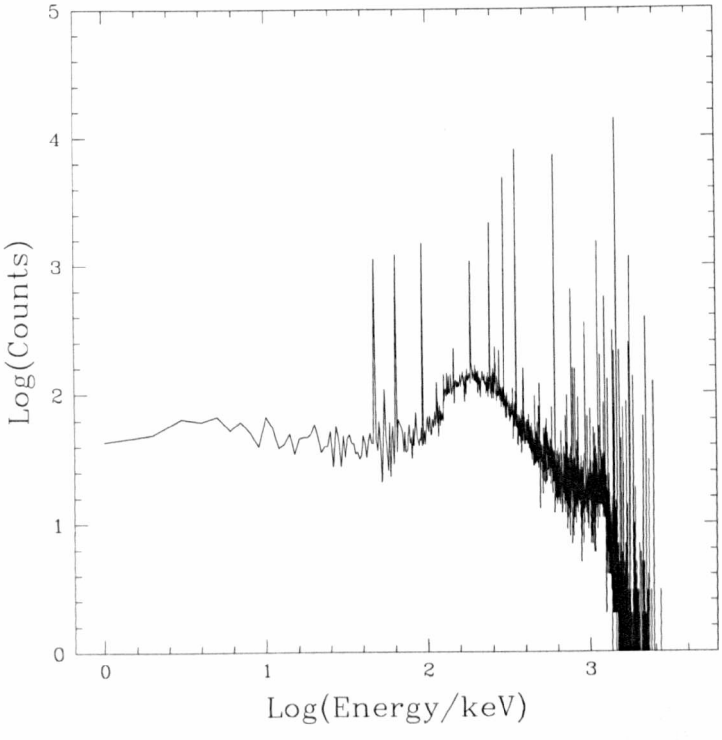


Fig. 7.13: Background energy spectrum with vetoed events removed.

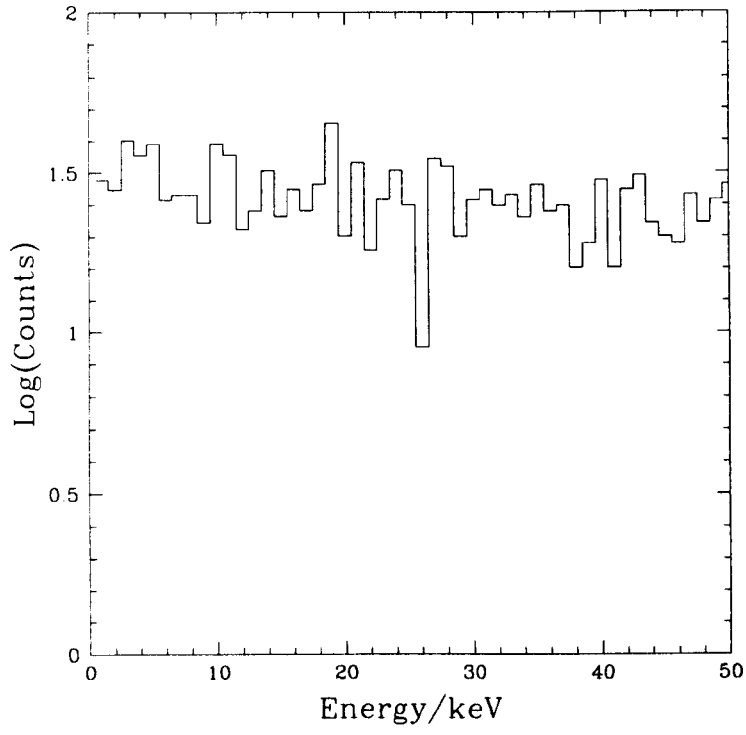


Fig. 7.14: Low energy depositions in xenon target volume due to radioactivity in the glass of photomultiplier tubes. These simulated data represent 5.4 hours real time running of ZEPLIN III detector. Vetoed and RFR events have been subtracted.

7.3.2 Light Code Application to ^{238}U and ^{40}K Background

The energy depositions and event positions simulated by the transport code were input into the light and charge collection code discussed in Chapter 6. This will enable characterisation of the background traces expected from the detector. Also the effects of the electric field distribution in the ZEPLIN III configuration to the detector were investigated.

Energy depositions were converted to primary scintillation and electrons following the discussion in Chapter 5. These photons and electrons were then transported. Output files containing the number of photons detected by each photomultiplier for both the primary(S1) and secondary(S2) scintillation were then input to a photomultiplier simulation code. Due to computational restrictions, only events that deposited energy $<$ 20keV were investigated (1 event renders a file of $\sim$10Mbytes). This energy range is the region of interest for discrimination studies.

Photomultiplier Simulation Code

The output from the LAC code is the number of photons detected by a certain photomultiplier. The photomultiplier code functions in two parts. First it models the arrival times of the photons. This is performed by assuming a single exponential decay time constant to the emission probability of a photon in xenon. The decay time constant is dependent on the energy of the gamma-ray energy, as measured by us [128]. At the time of arrival of this photon, the code constructs a single electron response. For the single photoelectron the photomultiplier response can be modelled using:

$$V(t) = -(1 - e^{-t/\tau_1})e^{-t/\tau_2} + noise \tag{7.7}$$

where $V(t)$ is the voltage at time t, τ_1 is the rise time of the photomultiplier, τ_2 is the fall time of the photomultiplier response and *noise* is random noise

generated on the pulse at the 0.5 photoelectron level. From [85] the values for τ_1 and τ_2 are 2ns and 3ns respectively, and these are used in the code.

To simulate the S2 pulses a similar procedure is used but with the time constant for the relaxation in the gas set to 28 $\pm$ 4ns. A single photon response is then placed at times corresponding to the time of photon emission offset by the drift time between steps in the gas.

Example Pulses from Photomultiplier Code

Fig 7.15 shows an example of signal traces from the 19 photomultiplier tubes from a single event in the liquid.

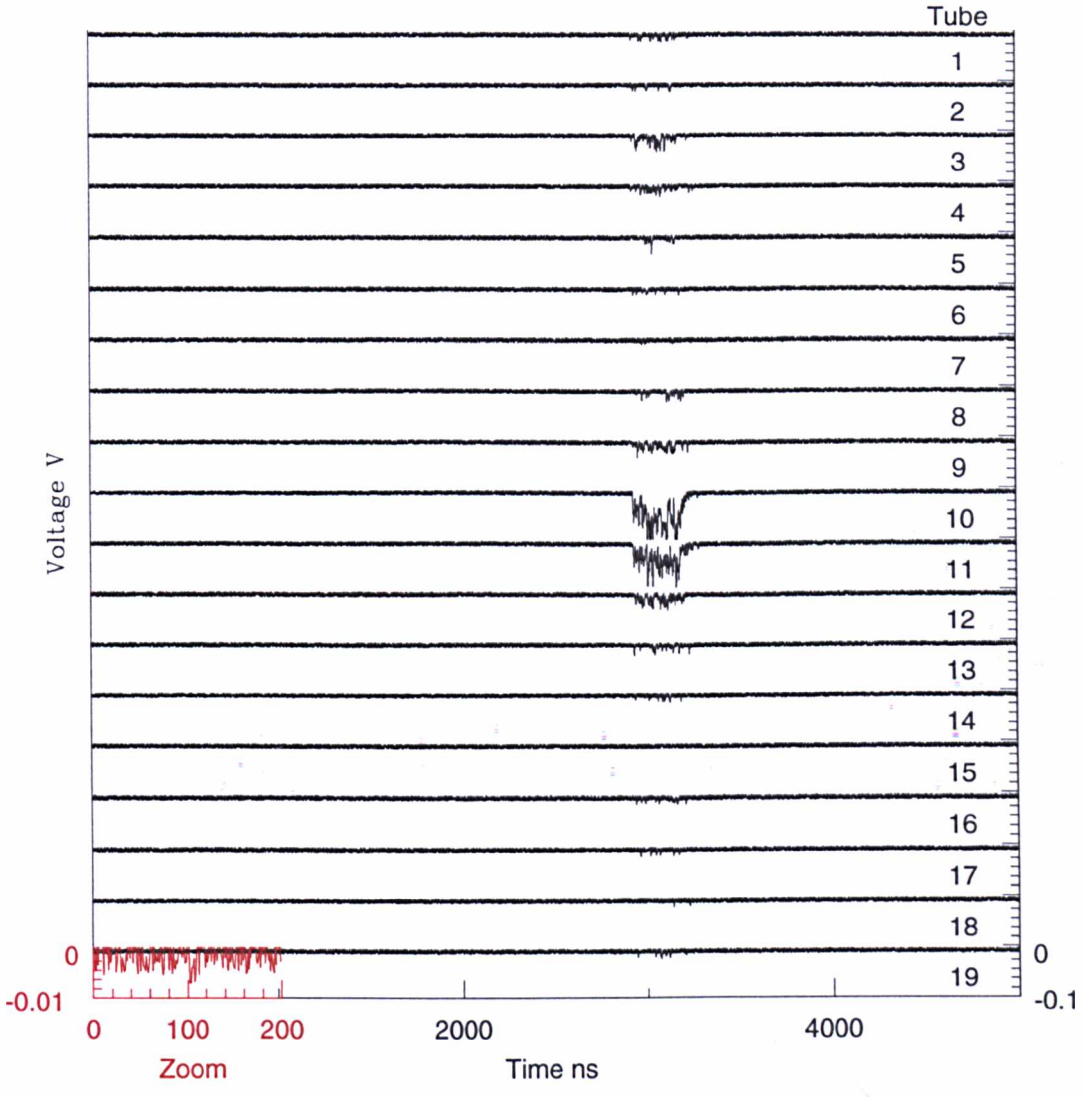


Fig. 7.15: Example of simulated pulses from a gamma-ray event in the ZEPLIN III two phase xenon detector. Pulses are from the 19 photomultiplier tubes running from top to bottom. S1 signal is in tube 19 (zoom bottom left).

Data sets containing pulses such as these were analysed. In the next section results from this analysis are presented and in particular measures of the discrimination of ZEPLIN III are found.

7.3.3 Results from Background Analysis and the Discrimination Power of ZEPLIN III

In this final section the results are given of the analysis of the dataset produced by the photomultiplier simulation code.

Energy Spectra for Background Events with $E_{depos} < 20$keV

The S1 scintillation signals from all the tubes for a single event are summed to give an energy spectrum of events due to background in the energy range 0-20keV. Similarily a spectrum of the S2 pulse area can be produced. The spectra are shown in Fig 7.16.

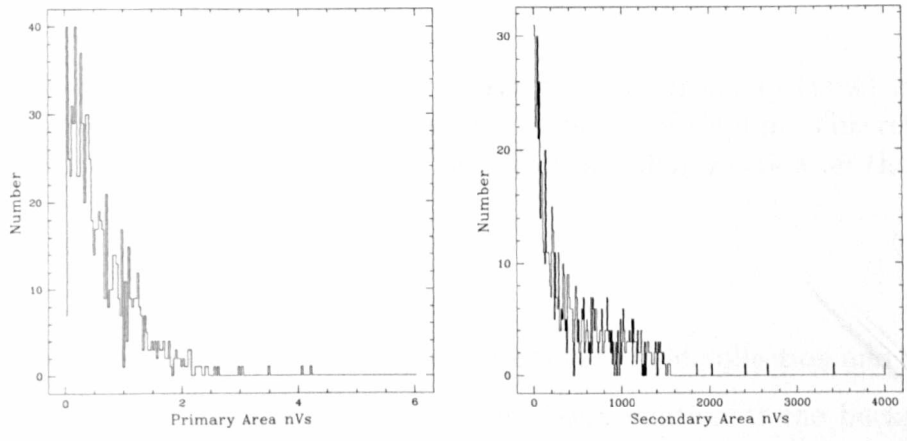


Fig. 7.16: S1 scintillation area spectrum (left) and S2 area spectrum (right).

Calculation of Discrimination in ZEPLIN III

The discrimination factor for ZEPLIN III depends on the ratio of the S2 to S1 signals from gamma-rays and nuclear recoils. The simulated background data

can be used to predict this for gamma-rays. For nuclear recoils an assumption can be made based on the data aquired from α-particle excitation of the two phase prototype, results from which were reported in Chapter 5.

Fig 7.17 shows the scatter plot of S1 versus S2 area for the background data. From the diagram we note the reduction in the ratio S2/S1 outside the defined

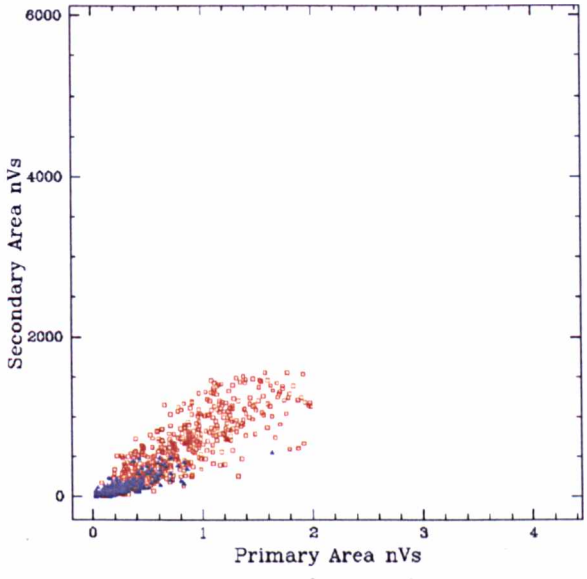


Fig. 7.17: Primary vs secondary signal scatter plot, triangles (blue) indicate events from outside a reference volume with a radius of 130mm. This reference volume is only used to demonstrate the effect of radial position on the signal sizes.

fiducial volume. This is probably a combination of light collection and electric field effects. To deduce a measure of the discrimination of the background from this plot, the following procedure was followed. The ratio S2/S1 was histogrammed for all the data points. This is shown in Fig 7.18. These data are clearly non-gaussian suggesting a source of systematic variability in the data. Hypothesising that the source of this systematic was from geometric effects i.e. that the non-gaussianity arose from the distribution of events throughout the detector volume, a correction procedure was employed. From the light collection and electric field simulations it is expected that the most uniform

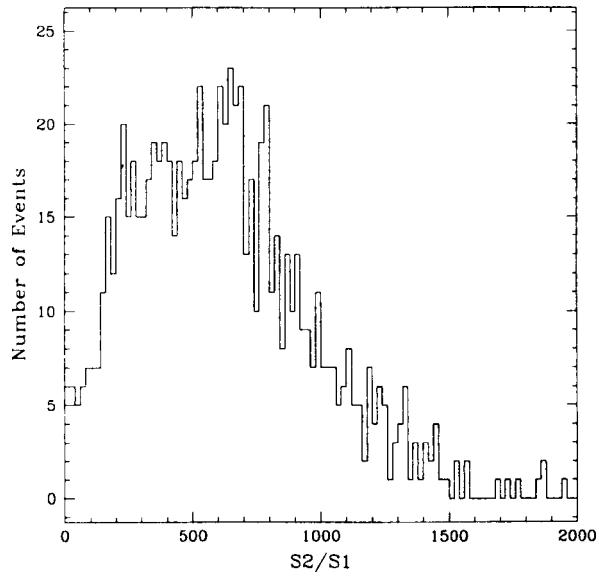


Fig. 7.18: Histogram of the ratio S2/S1 for gamma-ray background events.

response occurs at the centre of the detector. A volume containing events in this region can be used as a reference, with subsequent annuli responses being normalised to this region. An inner volume with radius 4cm was chosen as the reference volume, and the mean, μ_{norm}, of the S2/S1 ratio was calculated for those events within that volume. Similar distributions were created for successive annuli with radial limits of: 4cm-6cm, 6cm-8cm, 8cm-10cm, 10cm-12cm, 12cm-14cm, 14cm-16cm, 16cm-18cm, 18cm-20cm. The mean of the S2/S1 distributions for each annulus, μ_i, was compared to μ_{norm} and a correction factor, $k = \mu_{norm}/\mu_i$, was determined. The S2/S1 values for events were then corrected by the multiplicative factor, k. The corrected S2/S1 distribution is shown in Fig 7.19. This distribution still suffers a skew at high values of S2/S1. In order to characterise this distribution a sixth order polynomial was used. The equation of this polynomial is given in Equ 7.8. The polynomial fits the data well with an R^2 value of 0.88.

$$\begin{aligned} y &= 3.5604 \times 10^{-18}x^6 + 3.0127 \times 10^{-14}x^5 + 8.7976 \times 10^{-11}x^4 \\ &+ 8.9824 \times 10^{-8}x^3 + 1.4824 \times 10^{-5}x^2 + 5.2877 \times 10^{-2}x \\ &+ 0.90457. \end{aligned} \tag{7.8}$$

Where y is the number of events and x is the S2/S1 value. Fig 7.19 can be

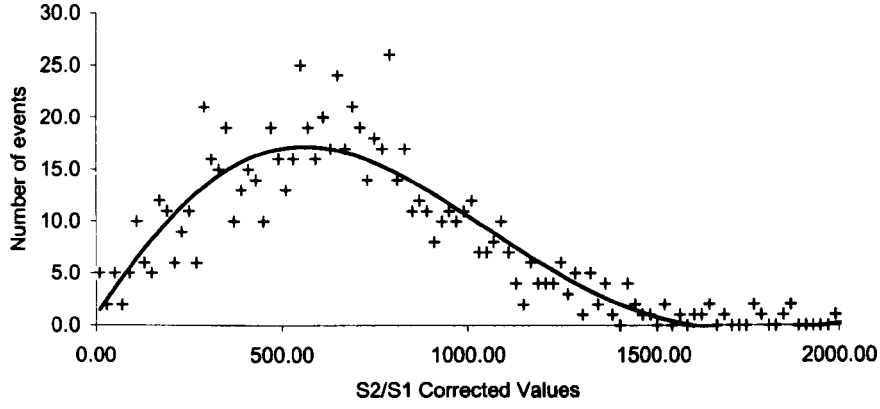


Fig. 7.19: Plot of the ratio S2/S1 for gamma-ray background events in the range 0-20keV after radial correction.

used to determine the background discrimination efficiency between 0-20keV. The statistics in this data set are not sufficient to allow investigations into the energy dependence of the discrimination.

To examine this question we must first assume a distribution for the expected nuclear recoil S2/S1 distribution. Earlier it was shown (Section 5.4.3) in experimental results that α-particles in a two phase prototype detector gave an S2/S1 ratio distribution of 5 $\pm$ 3, with a possible reduction of a factor of $\sim$10 due to the experimental setup. It is suspected that the ionisation from a neutron or WIMP nuclear recoil will be less than that of the α-particle. In the following calculations it is assumed that the nuclear recoil distribution will have a mean of μ_{nuc}= 5 as this is the worst case value and will give an upper

value of the discrimination factor. The neutron distribution is then a scaled version of the gamma-ray distribution. The neutron distribution for a value μ_{nuc}=5 is shown in Fig 7.20. The discrimination factor can be found by inte-

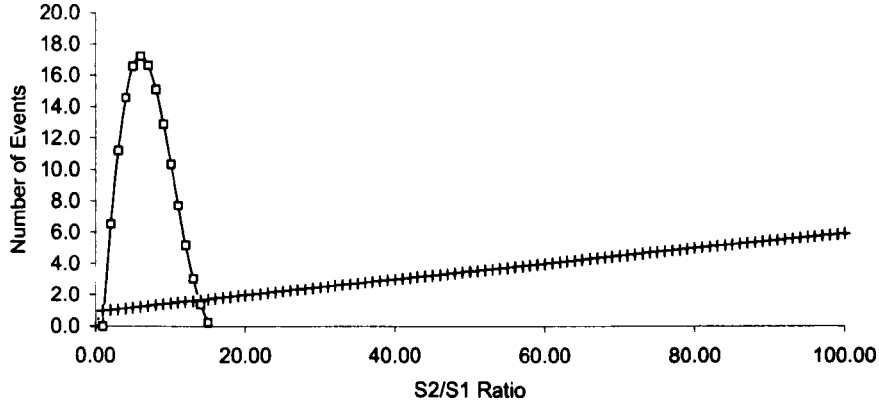


Fig. 7.20: Plot of Secondary/Primary ratio for simulated neutron distribution.

grating the area of the gamma-ray background distribution that passes below a defined discrimination level, $(S2/S1)_{dis}$. The discrimination level is set at a position that is well removed from the neutron distribution. In this case a value of 20 is chosen. Integrating the gamma-ray background distribution below this level and comparing this with the total area of the distribution renders a discrimination factor of 99.81%. The Monte Carlo programs indicate that the ZEPLIN III experiment will have powerful background rejection of 99.81% in the energy range 1-20keV. It must be noted that the discrimination factor will most likely depend on energy decreasing at lower energies. Unfortunately this investigation was unable to explore this dependency due to the constrictions of computing power and time. In the remaining parts of the thesis the discrimination factor is assumed to be constant in the range 1-20keV.

7.4 Summary

In this chapter results have been presented from Monte Carlo programs of the gamma-ray background from photomultipliers in ZEPLIN III. The code employed simulated the main volumes of the ZEPLIN III geometry. Transportation code for gamma-rays was developed and simulations were made of the expected gamma-ray spectrum from the photomultipliers. The expected background spectrum in the detector was found to be flat in the region 0-50keV and correspond to an expected rate of 9.2 dru. This spectrum was then linked into the light and charge code reported in Chapter 5. Photomultiplier responses were then added to the output of the light and charge code and the datastream was then analysed. Analysis of this data, assuming a possible value for the nuclear recoil S2/S1 ratio, indicated that the expected discrimination factor of ZEPLIN III is 99.81% in the range 1-20keV. The width of the background S2/S1 distribution is larger than was expected. Future work will be focussed in examining this distribution. By increasing the number of simulated events the energy dependence of the discrimination factor could be investigated.

CHAPTER 8

Sensitivity of ZEPLIN III

8.1 Introduction

In this short chapter results from the previous chapters are used to predict the sensitivity of ZEPLIN III. Plots are presented showing the sensitivity of ZEPLIN III to the spin independent interaction of the neutralino. The sensitivity plots are calculated using the formulae presented in Chapter 2, and in particular Eqn 2.16. The background estimates from the previous chapter are required for the calculations as well as the value for the quenching factor determined in Chapter 4, and also the discrimination factor from Chapter 7.

8.2 Sensitivity Plot Formulas

In order to calculate a sensitivity we use the following equation Eqn 8.1 which is a manipulation of Eqn 2.16.

$$\frac{N_0}{r} = \left[\frac{dN}{dE_r}\right]_{obs} q_r E_0 e^{\frac{E_r}{q_r E_0 r}} F^{-2}(E_r). \tag{8.1}$$

This equation allows one to calculate limits in terms of the actual count rate in the detector in events kg^{-1} day^{-1}. Let us look at the terms in the equation individually. $\left[\frac{dN}{dE_r}\right]_{obs}$ is the observed differential count rate in the detector at a particular energy E_r. The next term, q_r, is the quenching factor. In this analysis it is assumed that the quenching factor is independent of energy. E_0 is the incident kinetic energy of a dark matter particle and is equal to $0.5 M_d v_0^2$, where , M_d, is the neutralino mass and v_o is the characteristic WIMP velocity. The exponential term has two additional parameters. The first is E_r which represents the recoil energy of the target nucleus. In the following calculations E_r is set to the expected energy threshold of the detector as the lowest energy bins are most effective in setting the limits. The second parameter in the exponential contains the kinematic factor which, as before, is $r = \frac{4M_d M_T}{(M_d+M_T)^2}$. Finally $F(E_r)$ is the form factor, and accounts for the shape of the nucleus. In this analysis we assume $F(E_r)$=1. This will be the case if the energy threshold is low enough.

To convert the limit gained from Equ 8.1 into a limit of the detector - in terms of the cross section of interaction of a neutralino with a single nucleon - it is necessary to apply some conversion equations. First to obtain the total cross section limit $\frac{N_0}{r}$ is multiplied by the factor shown in Equ 8.2.

$$\sigma_{total} = \frac{N_0}{r} \frac{A}{1000 L n_0 v_0} \tag{8.2}$$

Finally to convert this total cross section to a cross section of a WIMP interacting with a single nucleon σ_{total} needs to be scaled as in Equ 8.3 [38].

$$\sigma_{WIMP-nucleon} = \frac{\sigma_{total}}{M_d M_T A^2 r} \tag{8.3}$$

Now let us look at the values of all the terms in these equations.

8.3 Values for Sensitivity Calculations

Table 8.1 gives the values of the terms used in the sensitivity calculations. The first term $\frac{dN}{dE_r}$ is calculated by taking the background rate and multiplying

Term	Value
$\frac{dN}{dE_r}$	0.0175dru
q_r	0.17
v_0	220kmsec^{-1}
E_0	$0.269M_d$
E_r	variable
M_T	123GeV
A	131
L	6.022×10^{23}
$F(E_r)$	1

Table 8.1: Values used in the sensitivity calculations.

it by the discrimination factor. The background rate and discrimination factor are taken from Chapter 7 and are equal to 9.2 dru and 99.81% respectively (note that the discrimination factor is assumed to be independent of energy as discussed at the end of Chapter 7).

8.4 Results From Sensitivity Calculations

The results from the sensitivity calculations are presented here in the format similar to the limit plots presented in Chapter 2. Fig 8.1 shows the limits expected from the ZEPLIN III detector. In this figure three detector thresholds of 1keV, 2keV, and 5 keV have been considered. The effect of the detector threshold can be seen in the figure. The higher the detector energy threshold the less sensitive the detector is to neutralino interactions. From Fig 8.1 we can see that the disparity in the sensitivities, for differing energy thresholds,

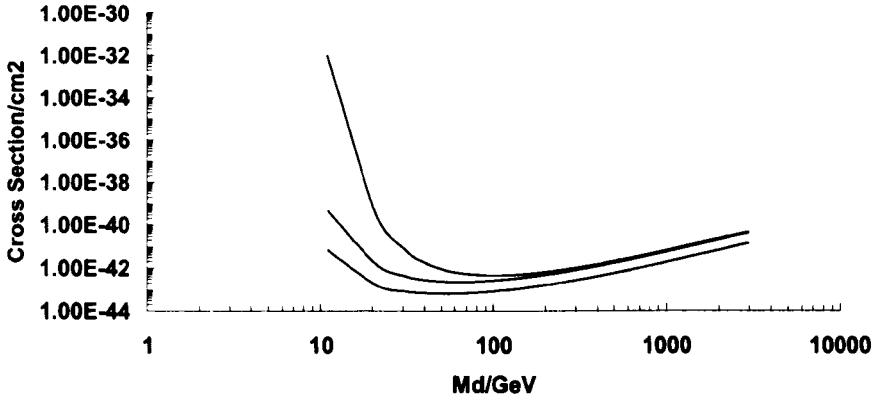


Fig. 8.1: Spin independent limit plot for ZEPLIN III detector for three detector energy thresholds. The upper curve corresponds to a detector threshold of 5keV, the middle curve represents the limit for a detector threshold of 2keV, and the lower curve is a limit for a detector threshold of 1keV.

is more apparent at lower masses. It is clear from Fig 8.1 that ZEPLIN III will be a competitive dark matter detector. Comparing this figure with Fig 2.6 from Chapter 2 shows that ZEPLIN III should give a limit comparable to the worlds leading dark matter detectors and will completely cover the DAMA region of interest.

8.5 Summary

In this short chapter the sensitivity of ZEPLIN III to neutralino dark matter has been presented. The calculation used numbers found through simulation and experiment including: the quenching factor, background rate and discrimination factor. Assuming a detector threshold of 1keV it was possible to construct exclusion plots similar to those presented it Chapter 2 making a direct comparison of the ZEPIN III detector sensitivity to other leading dark matter detectors possible. The exclusion plots presented show that ZEPLIN III will be sensitive to a spin independent cross section of $7 \times 10^{-44}\text{cm}^2$. Comparing this limit with Fig 2.6 from Chapter 2 we note that ZEPLIN III will

cover the DAMA region of interest.

CHAPTER 9

Conclusion

The latest cosmological models supported by astrophysical observations indicate that the Universe is flat and dominated by a Cosmological Constant energy density. The results from the observations of high redshift Type Ia supernovae suggest that the contribution of Cosmological Constant energy density to the total energy density of the Universe is approximately 0.7 or 70%. Limits on the baryonic energy density content of the Universe - from light element nucleosynthesis observations and theory - of 0.022 or 2.2% leaves a mass energy density deficit of nearly 28%. This deficit is evidence for a new type of undetected nonbaryonic matter. Evidence for the existence of nonbaryonic matter also exists when one considers the Large Scale Sturcture of the Universe. Measurements of the galaxy clustering on large scales suggests that the energy density deficit cannot be accounted for by a contribution from massive neutrinos as this results in too little fine scale structure. More locally, measurements of the rotation curve of the Milky Way and MACHO observations of the Large and Small Magellenic Clouds confirm the presence of this new form of matter in our Galaxy. The currently favoured candidate for the nonbaryonic dark matter is the Lightest Supersymmetric Particle, the neutralino. The neutralino should be detectable by its interaction with ordinary matter. Detectors currently running around the world attempt to detect the neutralino's interaction with matter by sensing one or more of the three following signatures of a neutralino event: scintillation, ionisation or heat. Neutralinos have a small cross section of interaction with ordinary matter of approximately 10^{-42}cm^2 per nucleon. In a xenon detector, this cross section gives an event rate of 0.5 events day^{-1} kg^{-1}. Theoretically the recoil spectrum of the neutralino lies in the 0-10keV region. Due to the low rate and low energy deposition in the detector target, dark matter experiments are conducted underground with radio-pure materials

so that unwanted background events are minimised. Despite the best efforts of experimenters, background events are still at high enough rates to swamp a dark matter signal. To further combat background, rejection techniques are employed in most experiments. These techniques in general rely on the fact that neutralinos interact with matter differently to the background, behaving akin to neutrons rather than gamma-rays. A neutralino signal should also be modulated over time due to the motion of the Earth about the Sun. Such a modulation has been reported by the DAMA experimental team in their NaI crystal scintillating detectors. This result has yet to be confirmed by another dark matter group. Indeed results from the CDMS team exclude some of the projected neutralino mass to cross section region suggested by the DAMA result.

Liquid xenon is a suitable dark matter detector target. The physical properties of the element lend it to the detection of both spin dependent and spin independent neutralino interactions. The liquid is dense, clear and scintillates with a high light yield in comparison to other scintillators, such as NaI. The peak scintillation line from the liquid is at 175nm and thus photodetecors sensitive in this range must be used to detect the light from an event. The 9829QA photomultiplier has been chosen by this group as it is sensitive to this wavelength of light and is also operable at liquid xenon temperatures as demonstrated by the results presented in Chapter 3 and from the two phase prototype detector in Chapter 5. Xenon detectors currently come in two guises. The simplest is the single phase detector which detects scintillation from events in the liquid. At Imperial College we have performed experiments using a single phase test chamber, investigating: the reflective properties of selected materials, the decay time constants of xenon scintillation and the quenching factor of liquid xenon. The results from the reflectivity measurements were used to determine the characteristics of the reflector used in the ZEPLIN I dark matter detector which is currently running in the Boulby mine. The second detector method is the two phase detector. In this techinique both the scintillation and ioni-

sation from an event are detected, the scintillation from the liquid phase and the ionisation in the gas phase after the charge is drifted from an event site in the liquid. The ionisation from a nuclear recoil in the liquid is expected to be much lower than that from an electron recoil. Hence a two phase detector is expected to have powerful background rejection capabilities. Such capabilities were indicated by the results from the two phase prototype detector presented in Chapter 5. The ZEPLIN III dark matter instrument is designed to operate as a two phase detector and is the focus of Chapters 6 & 7.

The ZEPLIN III detector is designed for high light collection efficiency and electron drift and extraction efficiency. The slab geometry and photomultiplier array give a light collection efficiency of 33% $\pm$ 5% in the liquid and 22% $\pm$ 16% in the gas gap. The electric field configuration in ZEPLIN III is uniform up to approximately 1cm from the edge of the electrodes where the field lines become curved. At a radius of 182mm in the detector, the field lines no longer reach the liquid surface and therefore electron extraction from the liquid to the gas is suppressed. The electron drift characteristics of ZEPLIN III are modelled by fits to known curves. These include: a drift velocity curve, electron yield for gamma-rays curve and an extraction probability curve. Using these curves it was possible to create a Monte Carlo model of the electron drift, gamma-ray light yield and electron extraction for gamma-ray events in the ZEPLIN III detector. The photomultiplier array in ZEPLIN III acts as an imaging system similar to that of an Anger camera. Using a template matching χ^2 reduction technique, and selecting events for which more than 10 photons were detected in the array, it was possible to show that position reconstruction in ZEPLIN III is possible. The accuracy of reconstruction varied from nearly 2mm accuracy, for events at the centre of the detector, to 12mm for events at the very edge of the detector.

The Monte Carlo modelling presented in Chapter 7 focuses on the expected gamma-ray background in the ZEPLIN III detector. Specifically the radioactive background from the photomultiplier tubes was considered as this is the

main source of contamination. The gamma-ray spectrum from the source contaminants was inputted and the resulting gamma-rays were traced through the detector geometry. The resulting output spectrum was obtained and after further analysis was found to be flat in the 0-50keV energy range and have a rate of 9.2dru. The background spectrum for events depositing 20 keV or less was inputted to the light simulation code developed in Chapter 6 and then finally into a photomultiplier simulation code. The resulting signals from the photomultiplier code were analysed and plots of the primary (S1) to secondary signal (S2) size were presented. The resulting data of the S2/S1 ratios was then corrected for radial position and used to find the discrimination factor for ZEPLIN III, given an assumed nuclear recoil distribution. The discrimination factor was found to be 99.81%.

To conclude this thesis the sensitivity of the detector was examined. Using values for: the quenching factor, background rate and discrimination factor obtained from earlier parts of this thesis it was possible to derive expected exclusion plots for ZEPLIN III. These exclusion plots indicated that ZEPLIN III will be sensitive to a spin independent cross section of about $7 \times 10^{-44}\text{cm}^2$, given a detector threshold of 1keV. This sensitivity is comparable to other dark matter detectors and most importantly explores the DAMA region of interest.

In conclusion, two phase liquid xenon detectors such as ZEPLIN III are a bright prospect for the future of dark matter experimentation. The expected excellent discrimination powers of liquid xenon technology will be an invaluable addition to the various detection strategies employed around the world. ZEPLIN III is expected to be built and deployed underground by the end of 2003, and so data and exclusion limits should be available by the end of 2004.

References

[1] J. C. Kapteyn 1922 Ap. J, 55, pg 302, 1922.

[2] J. H. Oort Bull. Astr. Neth 6, 249, 1932.

[3] G. Gilmore, Proc. 2nd Int. Dark Matter Conference 1996 (IDM96), Sheffield, UK, September 1996. In press, World Scientific. Available at URL; http://uk.arXiv.org/abs/astro-ph/9702081

[4] J. C. Mather et al. SPIE Conf. Proc. 2019, 146, 1993.

[5] Fixsen et al. 1996, Astrophysical Journal, 473, pg 576, 1996.

[6] A. A. Penzias, R. W. Wilson, ApJ, 142, pg 419, 1965.

[7] G. F. Smoot Ap. J, 396, L1, 1992.

[8] S. Burles et al., Phys. Rev. Lett. 82, pg 4176 (1999).

[9] R. Stomper et al., Submtted to Ap. J. Letters, May, 2001. Available at URL; http://uk.arXiv.org/abs/astro-ph/0105062

[10] C. B. Netterfield et al., Submitted to Ap. J., April, 2001. Available at URL; http://uk.arXiv.org/abs/astro-ph/0104460

[11] P. de Bernardis et al., Submitted to Ap. J. May, 2001. Available at URL; http://uk.arXiv.org/abs/astro-ph/0105296

[12] M. Zeilik et al., 'Introductory Astronomy and Astrophysics', Saunders College Publishing, 1992.

[13] G. 't Hooft, Nucl. Phys. B79 pg 276, 1974; A. M. Polyakov, JETP Lett. 20, pg 194, 1974.

[14] A. Guth, Phys. Rev. D23 347, 1981.

[15] M. Tegmark et al., Phys. Rev. D63 043007, 2001.

[16] S. Esposito et al., JHEP 0009 038, 2000.

[17] A. H. Jaffe et al. Phys. Rev. Lett., 86, pg 3475-3479 2000.

[18] S. Perlmutter et al., LBNL-4180, ApJ v.516 no.2., 1998.

[19] A. G. Reiss et al., Ast. J 116, pg 1009, 1998.

[20] L. V. E. Koopmans et al., 1999, Ap.J. 527, pg 513, 1999.

[21] R. G. Carlberg et al., Ap.J. 462, pg 32, 1996.

[22] K. B. Fisher et al., MNRAS 267, 927, 1994.

[23] S. Zaroubi et al., Ap.J. 486, pg 21, 1997.

[24] P. R. Roelfsema and R. J. Allen, Astron. Astrophys., vol 146, pg 213, 1985.

[25] V. C. Rubin, Sci. Am., vol. 248, pg 88, 1983.

[26] F. Zwicky, Helvetica Physics Acta, vol. 6, pg 110, 1933.

[27] R. Fusco-Femiano et al., Ap.J., vol 429, pg 545, 1994.

[28] B. Binggeli et al., Astron. J., vol. 94, pg 251, 1987.

[29] S. Warren, 'Current Issues of Astronomical and Planetary Environmental Concern', printed by Editions Ziti, pg 97, 1999.

[30] D. Wittman et al., to be published. Available at URL; http://uk.arXiv.org/abs/astro-ph/0009362

[31] M. Merrifield et al., Astron. J., vol. 103, pg 1552, 1992.

[32] C. Alcock et al., Nature, vol. 365, pg 621, 1993.

[33] C. Alcock et al., Ap. J., vol. L9, pg 499, 1998.

[34] C. Alcock, Science, vol. 287, pg 74, 2000.

[35] K. Sahu, Nature, vol. 370, pg 275, 1994.

[36] L. Roszkowski, to be published. Available at URL; http://uk.arXiv.org/abs/hep-ph/0102325

[37] T. Kajita et al., Nucl. Phys. Proc. Suppl., vol. 77, pg 123, 1999.

[38] P. F. Smith and J. D. Lewin, Phys. Rep. 187, no. 5, pg 203, 1990.

[39] T. Han and R. Hempfling, Phys.Lett. B415 pg 161-169, 1997.

[40] J. Primack et al, Ann. Rev. Nucl. Sci. 38, pg 751, 1988.

[41] T. J. Sumner, Proceedings of 2nd Int. Dark Matter Workshop, pg 227, 1999.

[42] V. Mandic et al., 'The Lower Bound on the Neutralino-Nucleon Cross Section', to be published. Available at URL; http://uk.arXiv.org/abs/hep-ph/0008022

[43] V. Mandic, R. Gaitskell, S. Golwala 'Direct Detection of WIMP Dark Matter, Sensitivity Plots ...An interactive plotter for experimental and theoretical data'. Available at URL; http://cfpa.berkeley.edu/ cdm-suser/limitplots/

[44] J. Ellis, A. Ferstyl and K. A. Olive, Phys.Rev. D63 (2001) 065016. Available at URL; http://arXiv.org/abs/hep-ph/0007113

[45] G. Jungman, M. Kamionkowski and K. Griest, Phys. Rep., vol. 267, pg 195, 1996.

[46] D. E. Groom et al., European Physical Journal C15, 1, 2000. Available at URL; http://www-pdg.lbl.gov/2000/contentssports.htmlastroetc

[47] M. Crouch, Proc. 20th Int. Cosmic Ray Conf., Moscow, vol.6 , pg 165, 1987.

[48] Yu. M. Andreev et al., Proc. 20th Int. Cosmic Ray Conf., Moscow, 6, 200, 1987

[49] M. Aglietta et al., Astropart. Phys., 3, pg 311, 1995.

[50] M. Ambrosio et al, Phys. Rev. D52, pg 3793, 1995.

[51] Ch. Berger et al, Phys. Rev. D52, pg 3793, 1995.

[52] P. F. Smith et al., Phys. Lett. B, vol. 379, pg 299, 1996.

[53] C. H. Lally "Development of a Cooled Sodium Iodide Scintillation Detector and its use in a search for Dark Matter", Ph.D. Thesis, University of London.

[54] G. J. Davies "Development of a Liquid Xenon Detector for use in Dark Matter Searches", Ph.D. Thesis, University of London.

[55] D. P. Snowden, C. J. Martoff and J. M. Burwell, Phys. Rev. D, vol. 61, 101301(R).

[56] K. Buckland et al., Phys. Rev. Lett., 73, pg 1067, 1994.

[57] A. Sonnenchein et al., Proceedings of 2nd Int. Dark Matter Workkshop, pg 347, 1999.

[58] G. Chardin et al., Proceedings of 2nd Int. Dark Matter Workshop, pg 365, 1999.

[59] J. D Lewin and P. F. Smith, Astroparticle Physics, vol. 6, pg 87, 1996.

[60] R. Bernabei et al., ROM2F/2000-32 to appear in Proceed. of the Int. Conf. PIC20, June 2000.

[61] K. Fushimi et al., Proc. Int. Dark Matter Conf. 2000, to be published.

[62] L. Baudis et al., Phys. Rep. v.307 pg 301-308, 1998.

[63] J. Jochum et al., Proc. Int. Dark Matter Conf. 2000, to be published.

[64] A. Benoit et al., to be published. Available at http://uk.arXiv.org/abs/astro-ph/0106314

[65] R. Adusaidi et al., Phys. Rev. Lett. 84, p.5699, 2000.

[66] R. Bernabei el al., Phys. Lett. B480, pg 23-31, 2000.

[67] N. J. C. Spooner et al., Phys. Lett. B vol 473, pg 330, 2000.

[68] Morales et al., from talk given at TAUP99 Conference, see proceedings.

[69] L. Baudis et al., to be published. Available at http://arXiv.org/abs/hep-ex/0012022

[70] J. Seguinot et al. Nucl. Instr. and Meth. A354, pg 280-287, 1995.

[71] T. Takahashi et al., Phys. Rev. A 12, pg 1771, 1975.

[72] T. Doke et al., Nucl. Instr. and Meth., A291, pg 617, 1990.

[73] N Ishida et al., Nucl. instr. Meth., A384, pg 380, 1997.

[74] A. S. Howard, Private Communication 2001.

[75] N. Schwenter E. -E. Koch and J. Jortner, "Electronic Excitations in Condensed Rare Gases", Springer Tracts in Modern Physics, vol. 107, 1985.

[76] S. Kubota et al., Phys. Rev. B20, pg 3486, 1979.

[77] K. S. Song et al., Can. J. Phys., 49, pg 26, 1971.

[78] S. D. Druger et al., Journ. Chem. Phys., vol. 50, pg 3143, 1969.

[79] P. G. LeComber et al., Phys. Rev. B11, pg 3124, 1975.

[80] J. Lindhard et al., K. Dan. Vidensk. Selsk., Mat.-Fys. Medd 33 (1963) 10.

[81] J. Lindhard et al., K. Dan. Vidensk. Selsk., Mat.-Fys. Medd 36 (1968) 10.

[82] A. R. Satler, Phys. Rev. A, no. 6, vol. 135, pg 1815.

[83] I. P. Flaks, Soviet Physics - Technical Physics (Russian translation), vol. 31, no. 3, pg 263-269, 1961.

[84] The ICARUS Collaboration, 'Scintillation Efficiency of Nuclear Recoil In Liquid Xenon', ICARUS-TM 99/14, 1999.

[85] Electron Tubes Ltd., 'photomultipliers and accessories' (product catalogue), 1996.

[86] Electron Tubes Ltd., Private Communication, Nov. 1999.

[87] A. Bewick, Private Communication, 1998.

[88] D. R. Tovey et al., Phys. Lett. B, vol.433, pg 150, 1998.

[89] N. J. C. Spooner et al., Phys. Lett. B, vol. 321, pg 156, 1994.

[90] G. J. Davies et al., Phys. Lett. B, vol. 322, pg 159, 1994.

[91] N. J. C. Spooner et al., Astrop. Phys., vol. 5., pg 299, 1996.

[92] R. Bernabei et al., Phys. Lett. B, vol. 436, pg. 379, 1998.

[93] E. B. Gordon et al., Chem. Phys. Letts., vol. 217, no. 5, pg 605, 1993.

[94] S. Kubota et al., Phys. Rev. B, vol. 17, no. 7, pg 2762, 1978.

[95] A. G. Molchanov et al., Kvantovaya Elektron. 1, pg 1122, 1974 (Russian).

[96] V. Egorov, Instr. Exp. Tech. 1, pg 53, 1988 (Russian).

[97] A. Parsons et al., IEEE trans. Nucl. Sci., NS-37, pg 541, 1990.

[98] H. Brauning et al., Nucl. Instr. and Meth. A348, pg 223, 1994.

[99] A. S. Howard et al., 'Measurements with a Two-Phase Xenon Prototype Dark Matter Detector', to be published in Proc. International Dark Matter Conference 2000, World Scientific publishing.

[100] D. A. Simon et al., Nucl. Instr. and Meth. A335, pg 86-101, 1993.

[101] A. Braem et al., Nucl. Instr. and Meth. A320, pg 228-237, 1992.

[102] T. Doke et al., Nucl. Instr. and Meth. A420, pg 62-80, 1999.

[103] P. Belli et al., Nucl. Instr. and Meth. A336, pg 336, 1993.

[104] I. M. Obodovsky, Proc. Inc. Conf. Liquid Radiation Detectors, Waseda University, pp. 235-245., 7-10 April 1992.

[105] N. Ishida et al., Nucl. Instr. Meth. A 384, pg 380, 1997.

[106] D. Yu Akimov et al., Nucl. Instr. Meth. A327, pg 152, 1993.

[107] H. A. Bethe, Ann. d. Physik 5, 325, 1930.

[108] S. M. Seltzer, M. J. Berger, Nucl. Instr. Meth. B12, pg 95, 1985.

[109] R. H. Pratt et al, Atomic Data Nucl. Data Tables 20, 175. Errata in 26, pg 477, 1981.

[110] National Institute of Standards and Technology Database. Available at URL; http://physics.nist.gov/PhysRefData/Star/Text/contents.html

[111] G. R. Freeman, in The Liquid State And Its Electrical Properties, Eds Kunhardt et al, NATO ASI Series B: Physics Vol. 193, pg 251-272, 1988.

[112] L. S. Miller et al, Phys. Rev., vol. 166 no. 3, pg 871, 1967.

[113] I. M. Obodovski et al, Physics of Low Temperatures, v5, no. 8 , pg 829-836, 1979 (Russian).

[114] T. Y. Voronova, J. Tech.Phys, v.59, Iss. 7, p 186-189, 1989 (Russian).

[115] E. M. Gushin, JETPh, v. 76, Iss. 5, pg 1685-1689, 1979 (Russian).

[116] D. Cline et al., Astroparticle Phys. 12, pg 373-377, 2002.

[117] Handbook of Chemistry and Physics, Ed. R. C. Weast, 55th Edition, pg B-416, 1975.

[118] V. G. Fastouskiy, A. E. Rovinskiy, Yu. U. Petrovskiy, Inert Gases, Moscow Atomizdat, pg 73, 1972.

[119] H. O. Anger, Rev. Sci. Instrum. vol 29, pg 27-33, 1958.

[120] S. Webb, The Physics of Medical Imaging 1988.

[121] S. Giarrusso et al, Nucl. Instr. Meth. A 354, pg 567-574, 1995.

[122] Available at URL; http://physics.nist.gov/PhysRefData /Xcom/Text/XCOM.html

[123] O. Klein Y. Nishina, Z. Physik, 52, pg 853 1929.

[124] Book of Data 8th Edition. Longman Group Ltd.

[125] I. Liubarsky, Private Communication 01/02/2001.

[126] T. J. Sumner, Private Communication, 2001.

[127] D. Lewin, Radioactivity Test Results, internal report, pg 3, 1995.

[128] D. Akimov et al., Phys. Lett. B, to be published. Available at URL; http://uk.arXiv.org/abs/hep-ex/0106042.